Thesis Report

MSc. Aerospace Engineering

Tom Vergoossen

Design, Integration and Testing of the PocketQube Reaction Wheel

TU Delft

Thesis Report

MSc. Aerospace Engineering

by

Tom Vergoossen

to obtain the degree of Master of Science
at the Delft University of Technology,
to be defended publicly on Friday August 25, 2017 at 09:30 AM.

Student number:	4089626	
Project duration:	October 17, 2016 – August 25, 2017	
Thesis committee:	Prof. dr. E. Gill,	TU Delft
	Dr. J. Guo	TU Delft, Supervisor
	Ir. J. Bouwmeester,	TU Delft
	Prof. W. A. Groen	TU Delft

An electronic version of this thesis is available at `http://repository.tudelft.nl/`.

TU Delft

Preface

This report presents my work on a reaction wheel for TU Delft's PocketQube satellite mission. I am very thankful for my supervisor Dr. Jian Guo's help and guidance. The staff in the Space Engineering department were invaluable in resolving practical matters related to testing and making engineering decisions. In particular I would like to thank Jasper, Stefano, and Mehmet. Prof. Pim Groen was very kind in providing guidance and making equipment and space in his lab available, which was a very enjoyable experience. I am also grateful to an excellent proofreader for her efforts. Furthermore, over the past years I have relied on the graceful support of my parents for which I am deeply grateful. Last, but not least, I would like to thank my friends for listening to me talk about reaction wheels and test set-ups beyond what they could reasonably be interested in. …

Tom Vergoossen
Delft, August 2017

Abstract

A highly miniaturised reaction wheel was developed for Delft University of Technology's PocketQube (PQ) mission as topic of this thesis project. Delfi-PQ, a picosatellite, aims to demonstrate a reliable core bus platform for PocketQubes with a form factor of 5x5x5 [cm] and one or more payload(s). PocketQubes hold the potential to reduce the cost of access to space and disrupt traditional space applications by providing cost effective global coverage. Three-axis stabilisation supports advanced capabilities such as Earth observation, high data rate transfers and propulsive manoeuvres. Precise attitude control requires reaction wheels with accurate speed control and low vibration levels. Power and volume requirements, however, drive a simple and compact design. Presently, no suitably miniaturised reaction wheel exists in the world. Therefore, a reaction wheel is developed specifically for the PocketQube mission. Due to a strict power requirement the research in this thesis focuses on characterising the power consumption of the reaction wheel.

Based on orbital disturbances and the operational context of the Delfi-PQ mission, requirements for the reaction wheel were derived. A suitable electric motor was selected and conclusions from a preliminary design were used to create a detailed design of a single reaction wheel. A simple flywheel is attached to a brushless electric motor and secured in a pressurised housing to protect the bearing lubrication from the vacuum of space. An in-depth model of the motor was created in Simulink and validated through functional testing of the motor. Model results were used to estimate control electronics power consumption. The housing of the reaction wheel was tested for its ability to seal off the motor and flywheel under atmospheric pressure. Then, the motor with flywheel was subjected to vibrations representative of the launch environment and functional testing of the reaction wheel including operational scenarios was performed. Furthermore, a micro-vibration test bench was developed in parallel to characterise the disturbances produced by the wheel. Based on conclusions, recommendations for improving a proposed design for a complete three-wheel assembly were derived.

With a mass of about 8 [g], average power consumption of around 15 [mW] and size of 20x20x12 [mm] the engineering model has been developed successfully. The reaction wheel can provide at least a torque of 2.7×10^{-7} Nm over its full speed range and has a (one way) momentum storage of 1.1×10^{-4} Nms. This is sufficient for attitude stabilisation and ground station tracking on a triple-unit PocketQube in a Low Earth Orbit with an altitude of above 360 [km]. The motor with flywheel uses about 35% more power than the motor alone. This is due to an imbalance of the flywheel which leads to more mechanical friction, although additional effects are present. Disturbances created by the wheel constrain Earth observation scenarios are speeds over 4000 [RPM]. A proposed three-wheel design was created that further pushes the boundaries of miniaturisation with dimensions of 31x31x22 [mm] including control electronics. Future developments should focus on developing control electronics, improving the vacuum seal of the housing and most importantly, the balance of the flywheel.

List of Figures

List of Tables

List of Abbreviations

ACC Accelerometer.

ADCS Attitude Determination and Control System.

BLDC BrushLess Direct Current.

COM Component.

DC Direct Current.

EMF ElectroMotive Force.

EMI ElectroMagnetic Interference.

EPDM Ethylene Propylene Diene Monomer.

EPS Electrical Power System.

ESA European Space Agency.

FAI Field-Aligned Irregularities.

FOS Factor Of Safety.

GSD Ground Sampling Distance.

GSFC Goddard Space Flight Centre.

HK Housekeeping.

HW Hardware.

I2C Inter-Integrated Circuit.

LEO Low Earth Orbit.

MAI Maryland Aerospace Inc..

MEMS MicroElectroMechanical Systems.

MOSFET Metal–Oxide–Semiconductor Field-Effect Transistor.

NASA National Aeronautics and Space Administration.

OBC On-Board Computer.

PCB Printed Circuit Board.

PID Proportional Integral Derivative.

PMSM Permanent Magnet Synchronous Rotor.

PQ PocketQube.

PWM Pulse-Width Modulation.

RAX Radio Aurora Explorer.

RMS Root Mean Square.

RW Reaction Wheel.

SSL Space Systems Laboratory.

TB Test Bench.

TU Technical University.

USB Universal Serial Bus.

List of Symbols

B Friction coefficient.

C_{drag} Drag coefficient.

D Diameter.

F Force.

H Momentum.

I Moment of Inertia.

L Length.

L_{ph} Phase inductance.

M Moment.

P Power.

S_U Voltage sensitivity.

T Torque.

V Voltage.

V_e Velocity.

α Thermal coefficient.

μ Standard Gravitional Parameter.

ω Rotation speed.

ρ Density.

θ Pointing angle.

a Acceleration.

c Speed of light in Vacuum.

c_{aero} Center of aerodynamic pressure.

c_{grav} Center of mass.

d Distance.

f_{res} Resonance frequency.

h Orbit altitude.

h Height.

i Angle of incidence.

i Current.

k Spring constant.

k_e Back EMF constant.

k_t Torque constant.

m Mass.

q Reflectance.

r_b Distance from centre of mass.

w Width.

Contents

1 Introduction

In this chapter the background for this thesis topic is discussed considering recent research, followed by a definition of the research scope and design process.

1.1. Background

In the past two decades satellite capabilities have been revolutionised by advancements in "*nano-, micro-, and miniature technologies*" [50, p.2]. On one hand this has led to "*increasingly capable and cost-effective space missions based on sub-500 kg satellites*" [49, p.1]. On the other hand "*largely supported by academic research*" [49, p.1], completely new classes of satellites (nanosatellites (<10 kg) and picosatellites (<1 kg)) have emerged that are now fully capable of performing scientific measurements. For example, the nanosatellite Radio Aurora Explorer (RAX) has studied "*the formation of magnetic Field-Aligned Irregularities (FAI) in the lower polar ionosphere (80-300 km)*" [45].

Nanosatellites, especially, have thrived on miniaturisation of space technologies, while picosatellite class satellites have great potential for future missions. More than 126 educational institutions have launched over 266 satellite missions [47]. Space agencies including the European Space Agency (ESA) and the National Aeronautics and Space Administration (NASA) operate CubeSat (a standardised nanosatellite) programs [50]. CubeSats have disrupted commercial space markets by replacing larger satellites in some applications and they have "*spawned significant commercial activity, including providers of complete satellites, components, and launch services, many of them starting as academic spin-off*" [50, p.1]. Altogether, over 482 CubeSats have been launched to date [47]. Manifold research in miniaturisation of technologies has led to advances in "*microelectronics, low-power communications, high-efficiency solar cells, low-cost precision fabrication, high-energy-density batteries, MicroElectroMechanical Systems (MEMS), high-density memory, field-programmable gate arrays, miniature high-efficiency motors and actuators, advanced materials, integrated optics, microsensors, and microfluidics*" [50, p.4]. Nanosatellites now have advanced capabilities such as precise three-axis attitude control [36], improved data rate communications [42] and on-board propulsion [19]. At present further advancements in miniaturisation are required for picosatellites to share the same functionalities. However, they hold the potential to further reduce the cost of access to space research and technology demonstration. Universities and others will be able to more easily conduct research in space and demonstrate new technologies. Moreover, distributed networks of picosatellites can replace traditional space applications by cost-effectively providing global coverage [31] for applications such as traffic monitoring [39]. Apart from this, inexperienced groups can start developing satellites of their own. For example, "*Emerging and developing countries have an opportunity to realize the tremendous potential* [of space missions] *for workforce and indigenous technology development*" [50, p.9].

The goal of this thesis project is to develop a highly miniaturised power efficient reaction wheel as part of the Delfi satellite programme. Specifically, the PocketQube is a three-unit picosatellite that is scheduled for launch in 2018, developed by Delft University of Technology. Reaction wheels directly support three-axis stabilisation and pointing of picosatellites, a key enabling technology. Pointing the satellite towards science targets, tracking ground stations and stabilisation during thrusting manoeuvres is required to support other capabilities such as

remote sensing, high data rate communication and orbit changes. A highly compact Attitude Determination and Control System (ADCS) currently measures 52x52x52 mm [10]. However, Delfi-PQ consists of cubes of only 50x50x50 mm indicating the present discrepancy between available solutions and requirements. Furthermore, due to reduced space for solar panels on picosatellites power consumption of existing ADCS systems is also prohibitive. For example, the reaction wheels of the three Unit (100x100x340 [mm]) CubeSat Delfi-n3Xt, a satellite launched by TU Delft, used a maximum of 750 [mW] of power [19]. Improvements in power consumption of one to two orders in magnitude are required for the wheels to be feasible on picosatellites.

In this report first the research objective and scope are defined followed by the definition of the design process. In the first design phase the operational context (Chapter 2) and orbital disturbances (Chapter 2) are used to derive system requirements in Chapter 4. In the following phase a preliminary design is created by selecting an electric motor in Chapter 5 and the design and evaluation of a supporting structure in Chapter 6. In the next phase a detailed model of the motor is presented in Chapter 7 and tests of the selected motor are used to verify its performance and validate the model in Chapter 8. The detailed design of the reaction wheel is given in Chapter 9. In the testing phase a test bench for measuring disturbances produced by the wheel is developed in Chapter 10 and the reaction wheel design is verified in Chapter 11, Finally, conclusions and recommendations are given in Chapter 12.

1.2. Research scope

In this section the research aim and objective are presented. The knowledge required to fulfil the objective is obtained by answering the identified research questions. Goals are defined that will be used to evaluate the success of the research in Chapter 12.

Research aim and objective

The **external aim** of this research project is:
To contribute to miniaturisation of space technology in general and the capabilities of picosatellites (<1 kg of mass) in particular by enabling 3-axis stabilisation and active pointing.

There is no ADCS small enough for 3-axis stabilisation of pico-satellites made of units of 5x5x5 [cm]. For active and precise pointing reaction wheels are required. However, presently they are both too large and consume too much power (see Appendix A).

The **research objective** of this thesis is therefore:
To design, integrate and test a PocketQube reaction wheel and characterise its power consumption in detail.

Research questions

Power consumption is expected to be the driving requirement for a PocketQube reaction wheel, hence it is the main focus of the research. The following research questions have been formulated to guide the research:

1. What is the ideal performance of a reaction wheel?
2. What effects lead to non-ideal performance and how can they be modelled?
3. What is the real performance of a miniaturised reaction wheel?
4. What is the power consumption of the reaction wheel in detail?

Project goals

Several goals are derived from the research questions that will be used to evaluate the success of the research project. Next to characterising the power consumption the required steps to verify the design are included. Goals are given in Table 1.1.

Table 1.1: Research goals

Research Question	Goal	Subgoals
1,2	Model the reaction wheel	Model ideal motion Identify all disturbances and inefficiencies Model non-ideal effects
3	Design, integrate and test the RW	Create preliminary design Integrate and test preliminary design Validate models Improve and create detailed design Integrate engineering model Test and verify the design
4	Characterise the power consumption	Design tests to measure power consumption Analyse differences between theoretical and real performance Characterise power consumption due to non-ideal effects

1.3. Design process

The design process that is used to design a prototype of the reaction wheel is visualised in Figure 1.1.

Design inputs are lessons learnt from the design of the reaction wheels for Delfi-n3Xt, high-level requirements and the operational context of the wheel, i.e. the PocketQube environment. After deriving the disturbance torques acting on the PocketQube the requirements at reaction wheel level are established. At this stage the process splits into a modelling and a hardware development branch. A preliminary design of the reaction wheel is created and conclusions from its verification are used to derive requirements at component level. Meanwhile, models of the reaction wheel are created and validated with functional tests of the motor, which are also used to verify some component level requirements. A detailed design of the reaction wheel is then created, the hardware manufactured and all tests are performed. Finally, conclusions with respect to the research questions, goals and objectives are made, and recommendations for future work are given.

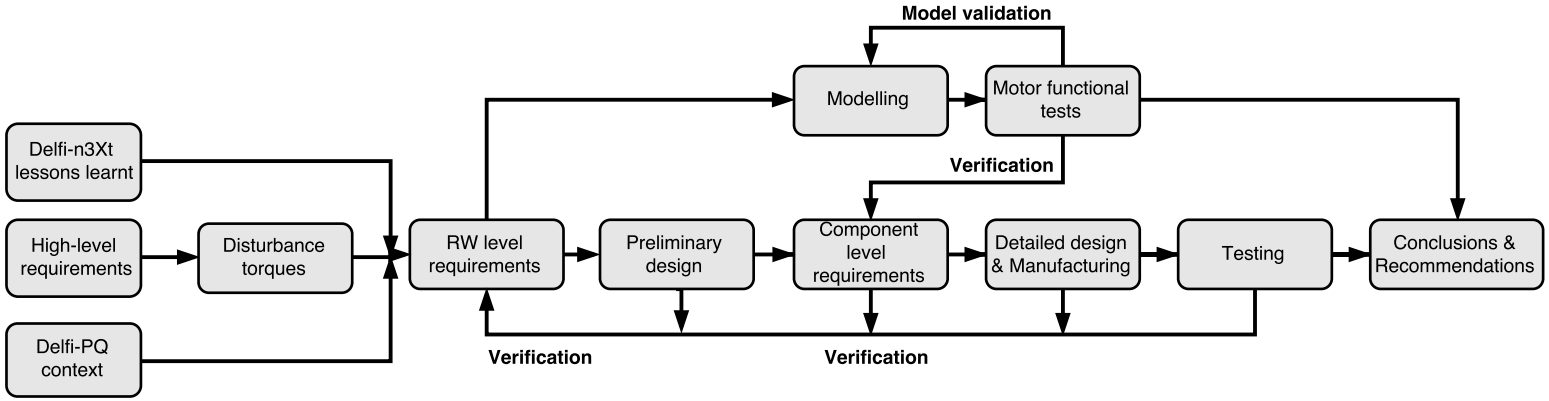

Figure 1.1: Design process

I

Requirements derivation

2

Operational Context

The reaction wheel is developed as part of the Delfi program at TU Delft, which previously successfully developed and launched two CubeSats: Delfi-C3 and Delfi-n3Xt. The general objectives of the Delfi-PQ mission are treated in Section 2.1, after which the environment of the reaction wheel and its purpose is considered in more detail in Section 2.2 and Section 2.3

2.1. Delfi-PQ mission

The Delfi-PQ mission aims to demonstrate a reliable core bus platform for PocketQubes with a form factor of 5x5x5 [cm]. The three-Qube platform will fly one or more payloads, which may include an advanced subsystem such as an Attitude Determination and Control Subsystem. Delfi-PQ is developed with a bottom-up engineering philosophy and components that are ready can be integrated into the first satellite, or in one of the planned successive launches. The first mission is scheduled for a mid-2018 launch.

2.2. PocketQube environment

The context in which the reaction wheel operates and the interfaces it has with other subsystems are a starting point for the design.

Figure 2.1 shows three levels, a reaction wheel assembly consisting of three reaction wheels, an Attitude Determination and Control level and the overall PocketQube level. The reaction wheel will be part of three reaction wheels that are integrated in the overall ADCS, which in turn is integrated into the PocketQube. Basically, the PocketQube consists of a stack of Printed Circuit Boards (PCB) measuring 5 by 5 [cm], which form the basis for each subsystem. The reaction wheels share their PCB with magnetorquers, an ADCS processor and attitude sensors. This represents the physical environment of the reaction wheel.

The reaction wheel has interfaces with each subsystem. In Figure 2.1 the most important ones are shown. Arrows represent an interface, and the associated text explains in general terms its main aspects. Some detail is left out for clarity's sake. For example, Electromagnetic Interference (EMI) of the reaction wheel with the communication subsystem is not included, because EMI is already considered in other interfaces. It is evident that interfaces exist beyond mere structural or electrical connections that are important for the proper functioning of the entire satellite.

The interfaces relevant for the design of the reaction wheel are considered in detail. For example, the disturbances produced by the reaction wheel are of major importance, while the interface between the control electronics and the main processor of the satellite is not so relevant. The important interfaces are shown in Table 2.1, which serve as input for the requirements derivation process in Chapter 4. The important interfaces are treated in more detail throughout this report. For example the disturbances are treated in detail in Chapter 10.

Table 2.1: Important interfaces

Interface	Important Aspects
Wheel to Wheel	Structural connection Disturbances EMI
Wheel - Control electronics	Motor Control Rotor position
RW Assembly - ADCS	Structural connection Disturbances
ADCS - PocketQube	Structural connection Disturbances Power
Control electronics - ADCS	Housekeeping data Commands

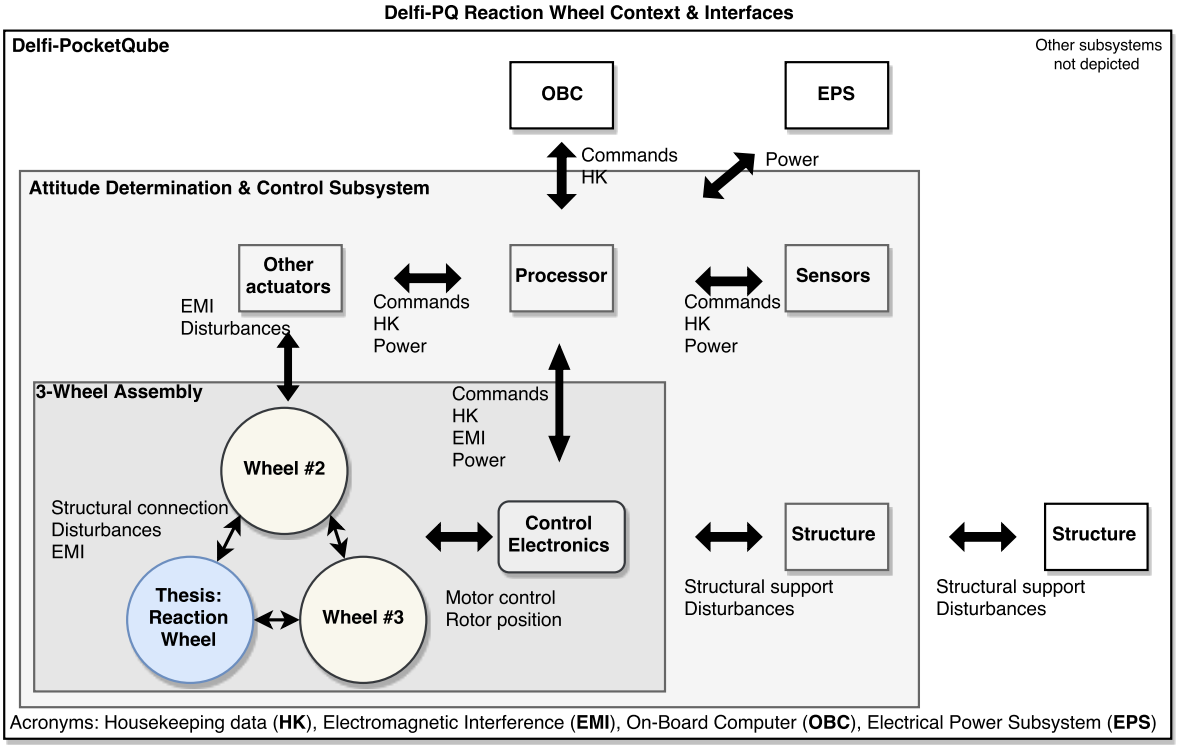

Figure 2.1: Context and Interfaces

2.3. Reaction wheel in-orbit operations

The reaction wheel's purpose is to generate torque and store angular momentum to control the orientation of the satellite in space. The wheel must counteract external (and internal) disturbances to maintain a particular orientation and perform manoeuvres over its orbital period.

Disturbances include aerodynamic drag, interaction of the satellite with Earth's magnetic and gravitational field and solar radiation pressure. Other effects such as Earth's oblateness and third body perturbations, e.g. the gravitational attraction of the Moon, are negligible.

Attitude manoeuvres include changing of the satellite's orientation, e.g. from sun-pointing to Earth pointing, and initiating a specific rotational motion, e.g. actively pointing towards a ground station during a flyby. These are mission specific. For the design of the reaction wheel Earth pointing and ground station tracking are

considered. Manoeuvres are used to evaluate torque and momentum storage requirements derived in Chapter 3.

Internal disturbances may include fuel sloshing, deployment of solar panels and disturbances created by the wheel itself. For the PocketQube only the latter is of relevance. It is crucial to test whether these disturbances limit the pointing of the satellite.

On a per orbit basis, the reaction wheel will continuously increase its rotation speed as it counters disturbances. When the satellite is over Earth's poles the momentum can be 'dumped', i.e. the rotation speed can be reduced, as the satellite's magnetorquers stabilise the satellite. Momentum dumping strategies vary and depend on mission specific orbits. The wheel is developed to fit a once or twice per orbit dumping scenario, i.e. at least every second polar pass momentum shall be dumped.

3

In-orbit disturbances

In this chapter the external disturbances acting on the satellite are analysed. They typically drive the design of the reaction wheel. In the calculations an Earth-pointing mode of Delfi-PQ is assumed, which means that the aerodynamic and gravity gradient torques are secular and the solar and geomagnetic torques are cyclic. Other effects such as Earth's oblateness, third body perturbations and radiation pressure from reflected and/or re-emitted sunlight are assumed to be negligible. The effect of aerodynamic drag is discussed in Section 3.1. Disturbances resulting from the interaction between the satellite and Earth's magnetic and gravitational field are analysed in Section 3.2 and Section 3.3, respectively. Solar radiation pressure is considered in Section 3.4. In conclusion a torque and momentum storage requirement for the reaction wheel are derived in Section 3.5 and Section 3.6, respectively.

3.1. Aerodynamic drag

In Low-Earth Orbit (LEO) gas molecules impact the satellite resulting in a drag force acting through the centre of pressure of the satellite. An offset with the centre of gravity of the satellite results in a disturbing torque about the centre of gravity of the satellite. This torque can be approximated for different geometries using Equation (3.1) [28].

$$\begin{aligned} T_{aero} &= F_{lift} \times (c_{aerp} - c_{grav}) \\ T_{aero} &= \frac{1}{2} \times \rho \times C_{drag} \times A \times V_e^2 \times (c_{aerp} - c_{grav}) \end{aligned} \tag{3.1}$$

Air density, ρ, is taken during solar maximum conditions [9]. The drag coefficient of the satellite C_{drag} is assumed to be 2 [28]. The largest surface area of the satellite is: $0.16 \times 0.5 = 0.08[\mathrm{m}^2]$. Ve is the satellite's orbital velocity with respect to the atmosphere and is calculated for a circular orbit using: $V = \sqrt{\frac{\mu}{(R_E+h}}$, where μ is a standard gravitational parameter of the Earth, R_E is the Earth's radius and h the altitude of the satellite above ground. It is assumed that this is the speed of the satellite with respect to the atmosphere. The distance between the centre of aerodynamic pressure c_{aerp} and the centre of gravity of the satellite c_{grav} is assumed to be given by the offset of the centre of gravity from the geometric centre of the satellite [28]. A scaled down value of the CubeSat standard limit on this value is used ($0.0025[m]$).

This simplified equation only considers normal pressure forces. A better approximation is obtained using particle/surface interaction models that can be derived from free-molecular flow theory [34, p.5]. This also accounts for friction effects as molecules slip on the surface of the satellite [18]. Free-molecular flow conditions hold when the molecular mean free path is larger than the spacecraft dimensions [34, p.4]. Molecules that have impacted the satellite travel far before they interact with other gas particles and the air flow is thus undisturbed by the satellite's presence. The resulting torque is simply the sum of the individual drag contributions by the different spacecraft elements [34, p.4]. Delfi-PQ has a simple rectangular shape so for the orientation with maximum area no summations are required. However, a more detailed analysis should evaluate the aerodynamic drag as a function of satellite orientation. Furthermore, time-varying effects such as lower densities in eclipse and changes in the relative orientation of the satellite's velocity vector with the gas molecules should

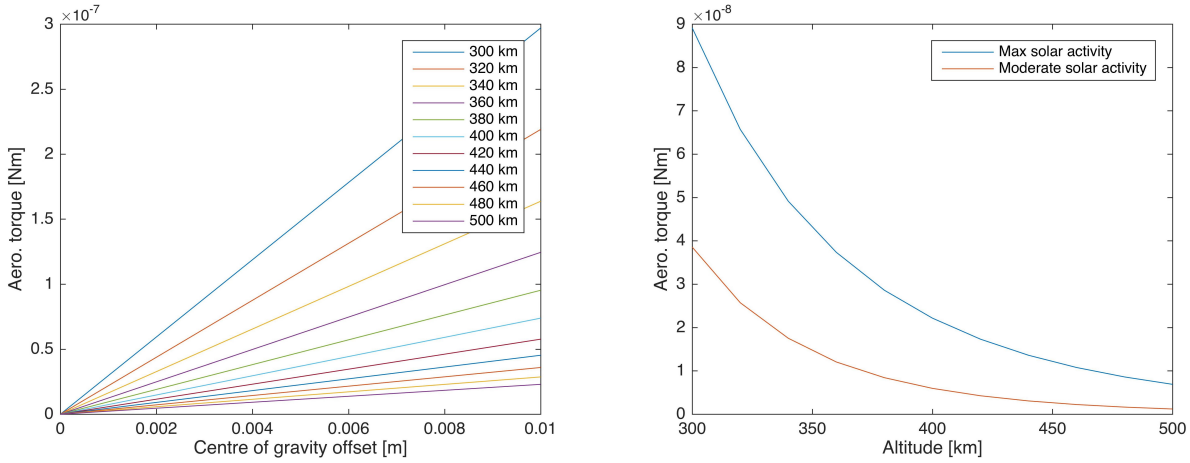

Figure 3.1: Aerodynamic disturbance torque a) as a function of centre of gravity offset and b) as a function of altitude for an offset of 0.003m

be accounted for. However, for a first approximation the formula used above is considered sufficiently accurate [28].

The sensitivity of the torque to parameter changes is illustrated in Figure 3.1. The torque is inversely proportional to altitude and directly proportional to centre of gravity offsets. The value of the torque for an offset of 0.003 [m] at an altitude of 360 [km] for maximum solar activity is taken as design torque.

3.2. Geomagnetic torque

A residual dipole of the satellite will interact with Earth's magnetic field resulting in a force perpendicular to both the local magnetic field lines and the orientation of the satellite's dipole. The resulting torque on the satellite can be calculated as [28]:

$$T_{gm} = D \times B = D \times \frac{2M}{(R_E + h)^3} \tag{3.2}$$

Where B is the Earth's magnetic field strength at satellite altitude, M is the Earth's magnetic moment and D is the satellite's residual dipole. This equation assumes the satellite can be described as a simple dipole and gives an approximation of the maximum value of Earth's magnetic field as a function of altitude and holds for the maximum value occurring above Earth's poles. The satellite's residual dipole D is difficult to predict. The 1 unit CubeSat Compass-1 used an estimate of 0.01 [Am^2] [18], while for Delfi-n3Xt a three unit CubeSat, a residual dipole of 0.001 [Am^2] was assumed. The latter is used for Delfi-PQ as well because the residual dipole can be measured and modified during testing. The geomagnetic torque as a function of the residual dipole for different altitudes is shown in Figure 3.2. Like the gravity gradient torque it is relatively insensitive to altitude, but it is proportional to the residual dipole. The design torque is 1.95×10^{-7} [Nm].

3.3. Gravity gradient torque

Due to the satellite's non spherical mass distribution a torque acts around the centre of gravity of the satellite that attempts to align the satellite's largest moment of inertia axis with the nadir axis. This torque can be calculated as [28]:

$$T_{grav} = \frac{3\mu}{2(R_E + h)^3} |I_z - I_y| \sin 2\Theta \tag{3.3}$$

Where μ is Earth's standard gravitational parameter, R is the satellite's distance from the centre of the Earth and I_z and I_y are the satellite's moment of inertia around the nadir axis and along track direction respectively. Θ is equal to the pointing error of the satellite and is maximum at 45 degrees. This equation neglects third body gravity fields, assumes a spherical Earth and a rigid satellite that is small when compared with its distance from Earth [18].

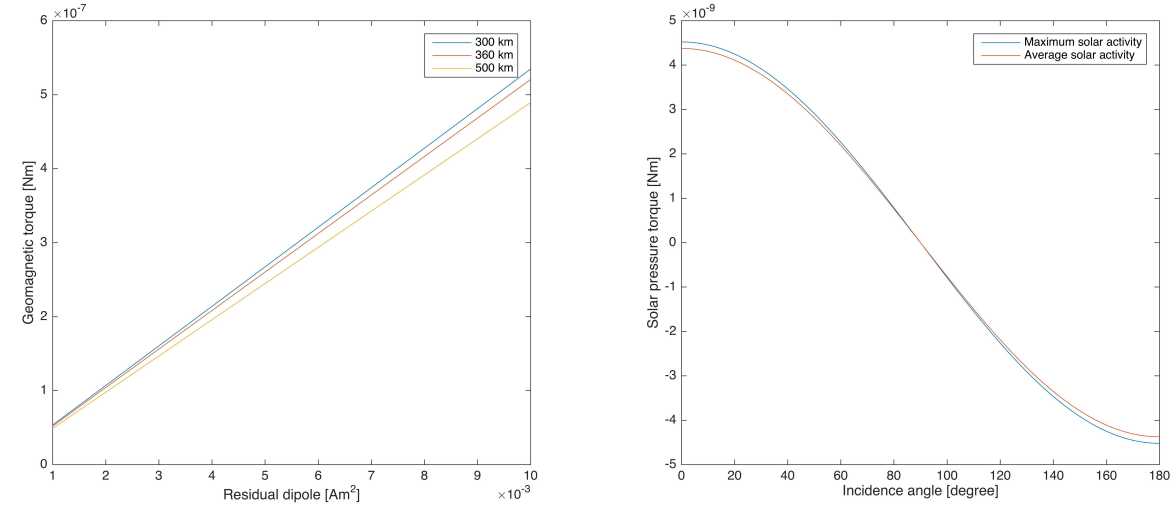

Figure 3.2: a) Geomagnetic torque b) Solar radiation torque

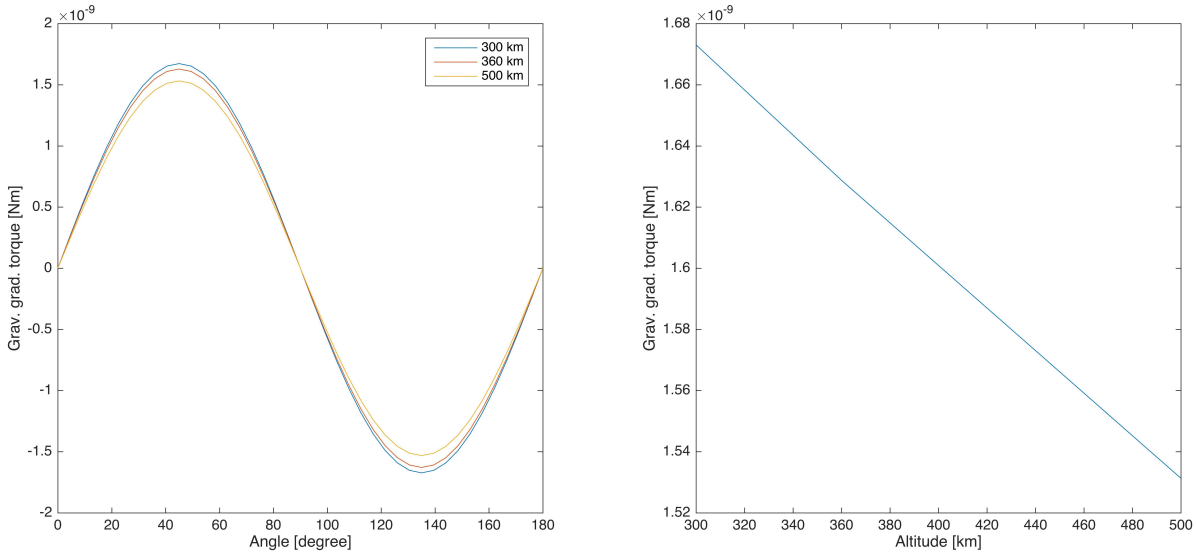

Figure 3.3: Gravity gradient torque as a function of a) satellite orientation b) altitude for largest deviation

A plot of the gravity gradient torque for different altitudes and orientations is shown in Figure 3.3. The design torque is taken at 360 [km] altitude at the largest deviation of 45 degrees as 1.6×10^{-9} [Nm]. Because the satellite altitude is relatively small compared to Earth's radius the torque is not very sensitive to changes in altitude, but changes in orientation of the satellite have a large effect. For a spherical Earth, the gravity gradient torque will remain constant over one orbit for an Earth pointing mode provided that the pointing error is constant in magnitude and direction.

3.4. Solar radiation pressure

Photons emitted by the Sun strike the satellite and exchange momentum. The resulting pressure force acts through the centre of pressure of the satellite. An offset with the satellite's centre of gravity results in a torque on the satellite. This torque can be calculated as [28]:

$$T_{sp} = \frac{c_s}{c} A_s (1+q) \cos i (c_{solp} - c_{grav}) \tag{3.4}$$

Here c is the speed of light, i is the incidence angle of sunlight. It varies from 0 to 90 degrees, but the maximum value at 0 degrees is considered. The solar constant c_s in an Earth orbit is maximum at 1412.9 $[\frac{W}{m^2}]$ [16]. The reflectance of the satellite's face illuminated by the sun, q, is assumed to be 0.6 [28], a value which is largely

determined by the solar cells. The force arm is again assumed to be equal to the offset of the satellite's centre of gravity.

The solar radiation torque as a function of incidence angle is shown in Figure 3.2 b). It is independent of altitude because the solar constant is a function of distance from the Sun. In eclipse the torque will be zero. The design torque is taken at its maximum of 4.5×10^{-10}.

3.5. Minimum required torque

All disturbance torques together can be seen in Figure 3.4. The torques do not act in the same direction, so instead of summing the individual torques, the maximum disturbance torque including a margin of 50% is taken as minimum design torque. As Delfi-PQ should be able to operate in low earth orbits the geomagnetic torque is the largest, but in very low orbits (below 320 [km]) the aerodynamic torque becomes important as well. At 360 [km] the geomagnetic torque including a margin is $1.95 \times 10^{-7} \times 1.5 = 2.93 \times 10^{-7}$ [Nm]. This design torque covers disturbances at all altitudes above 320 [km]. Furthermore, as explained in Chapter 5, the motor is able to deliver more torque over most of its speed range.

The torque requirement is evaluated considering whether it can support ground station tracking. Required slew rates for tracking a ground station for various inclinations (as seen from the ground station) are shown in Figure 3.5. It can be seen that it takes between 17 to about 30 seconds to initiate the maximum slew rate (during direct flyover) with a torque of 2.93×10^{-7}. Considering an orbital period of between 90.4 and 94.6 minutes, this time period is considered acceptable.

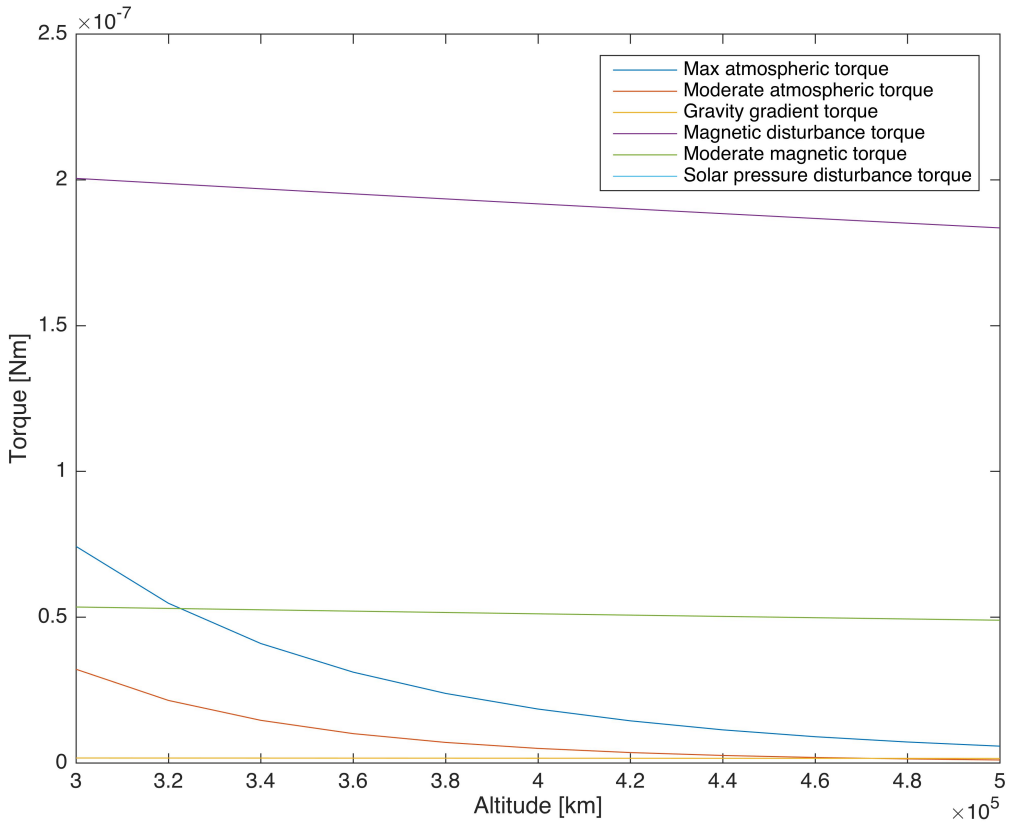

Figure 3.4: Disturbance torques

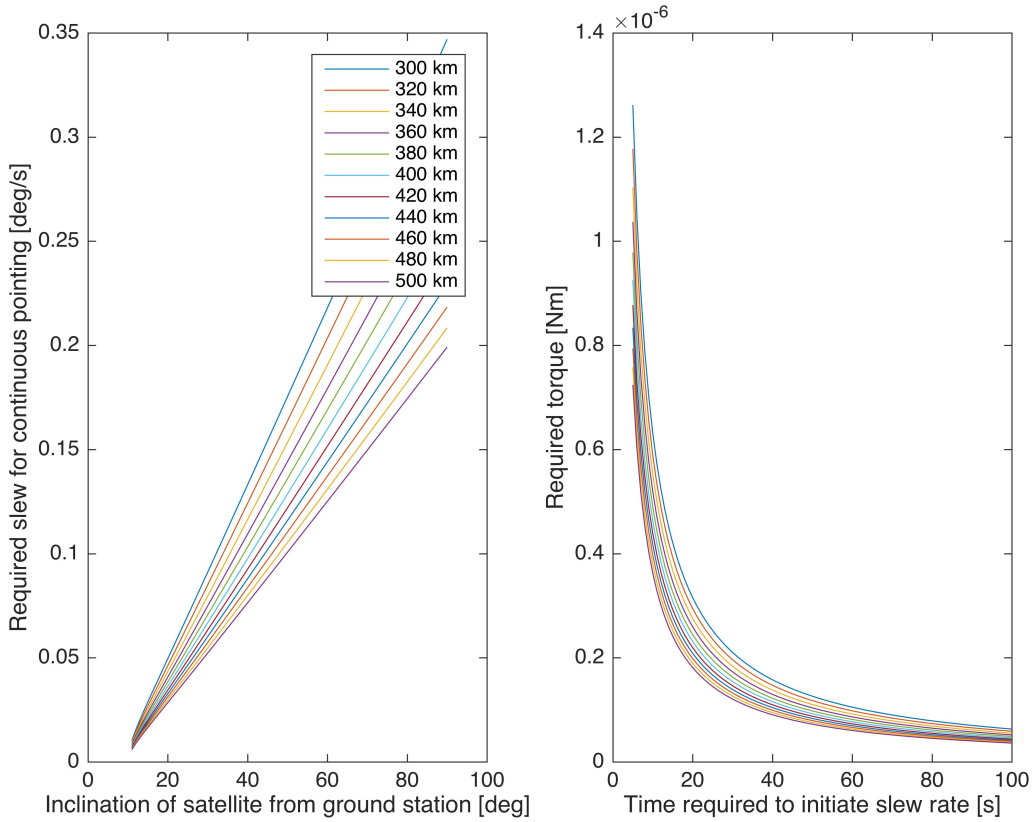

Figure 3.5: a) Required slew rates for ground station tracking b) Time required to initiate max slew rate

3.6. Minimum required momentum storage

The required momentum storage in the wheel is derived by integrating the worst case disturbance torque over the time it builds up up during one orbit [30]. The gravity gradient and aerodynamic torques are constant. The magnetic torque is cyclic with a period of half an orbit as the magnetic field direction flips at the poles, i.e it builds up over one quarter orbit. The solar radiation torque can be assumed to be maximum after a quarter orbit [30].

By considering some torque scenarios in Table 3.1 the importance of the satellite's residual dipole becomes apparent. Taking the estimate based on the Compass-1 nanosatellite a momentum storage requirement of 2.7×10^{-4} [Nms] should be taken. However, the residual dipole assumed for the Delfi-n3Xt satellite leads to a requirement of 0.72×10^{-4} [Nms]. Similarly, if the satellite is launched during a solar maximum a much larger momentum storage would be required than during moderate solar activity, as a result of the increased atmospheric density.

The final momentum storage requirement is set based on two considerations. First, the residual dipole of the satellite can be changed after the satellite is integrated. The value used for the Delfi-n3Xt design is used as a limit value. Now the aerodynamic drag is the biggest contributor. Secondly, the satellite is not launched during a solar maximum [16] and an average of the momentum storage required during a solar maximum and average solar activity is a reasonable approximation. This yields a momentum storage requirement of 1.1×10^{-4} [Nms].

Clearly, this value is sensitive to the specific orientation of disturbance torques and to errors due to simplification in the manner in which they are calculated. To account for this, an inherent safety factor of two is implemented by designing the wheel so that it can store the required momentum in both rotation directions. This is considered in selecting a suitable electric motor in Chapter 5.

The requirement can be evaluated by comparison with the value for Delfi-n3Xt's momentum storage requirement, which at 1.56×10^{-3} [Nm] is about 9 times larger. Considering that Delfi-PQ weighs about 8 times less this is reasonable, although it depends on how exactly the requirement was established.

Table 3.1: Disturbance torques and momentum

Disturbance	**Case**	**Torque at 360 [km] [10^{-6} Nm]**	**Time period [1 orbit]**	**Momentum [10^{-6} Nms]**
Aerodynamic drag	Solar maximum	0.031	1	171.28
	Average solar activity	0.01	1	55.23
Geomagnetic torque	Scaled estimate of Compass-1	0.195	1/4	268.6
	Delfi-n3Xt residual dipole	0.052	1/4	71.6
Solar radiation pressure	Solar maximum	0.000151	1/4	0.21
	Average solar activity	0.000145	1/4	0.2
Gravity gradient torque	45 degree deviation from Earth pointing	0.00163	1	8.8
	5 degree deviation from Earth pointing	0.00028	1	1.56

3.7. Chapter summary

In this chapter external disturbances acting on the spacecraft were analysed to derive torque and momentum storage requirements for the reaction wheel. Aerodynamic drag, geomagnetic torque, gravity-gradient torque and solar radiation pressure were considered and the sensitivity of design parameters was analysed. Especially problematic is the geomagnetic torque as it relies heavily on the assumption for a residual dipole of the satellite. It was judged that, since the residual dipole can be manipulated after integration of the satellite, the value assumed during design of the Delfi-n3Xt satellite scaled down to PocketQube dimensions is a reasonable estimate. The torque requirement was set at 1.5 times the maximum expected disturbance torque. The momentum storage requirement was set after detailed consideration of the different disturbances, and how they act over one orbit. Nonetheless, simulations of how the torques evolve over one orbit are required to establish a definitive value. To account for sensitivities of the requirement to input parameters the wheel will be designed such that it can store the required momentum in both directions of rotation. In the next chapter the torque and momentum requirements are used to derive the complete set of requirements at the RW level.

4

System requirements

Requirements are derived to ensure the reaction wheel is designed to fit the need of the PocketQube mission. First, the functions that the wheel should be able to perform are discussed in Section 4.1. In combination with some PocketQube mission specific requirements all requirements are derived from them. Characteristics of the wheel are derived in Section 4.2, and constraints on it are discussed in Section 4.3. Requirements at RW level are then presented in Section 4.4, whereas component level requirements are given at the beginning of their respective sections. Finally, verification and validation of the requirements is discussed in Section 4.5.

4.1. Capabilities

The high level functions of the reaction wheel, as shown in Figure 4.1, are to produce torque and store angular momentum. At a lower level important requirements such as controlling the rotation speed with a certain accuracy are found. By quantifying to what extent the RW should fulfil these functions the performance requirements of the wheel are derived. Torque and momentum storage requirements were already derived in Chapter 3. In this section the detailed functions identified in Figure 2.1 are quantified.

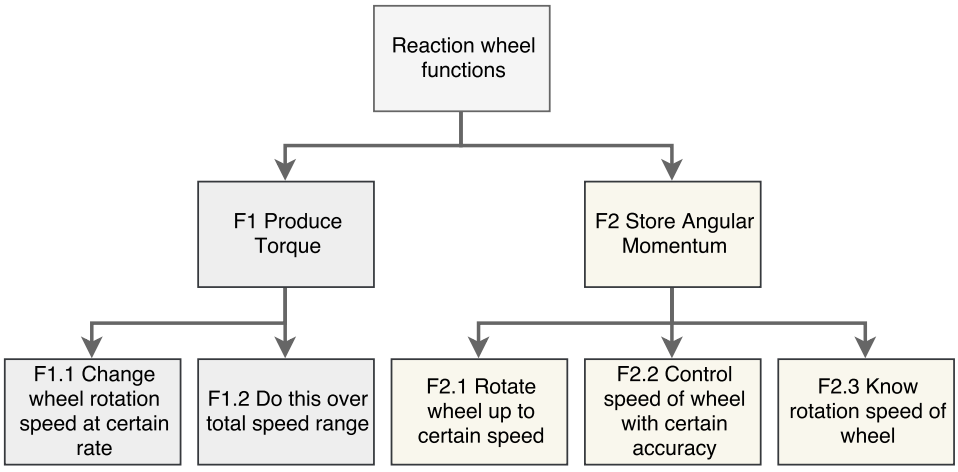

Figure 4.1: Reaction wheel functional breakdown structure

Functions F1.1 and F1.2 are not quantified further, as the torque requirement is sufficient to select a suitable motor. The maximum speed requirement F2.1 depends on the selected motor and flywheel size. This is calculated in Section 5.3. Function F2.3, is a direct selection criterion for an electric motor type in Section 5.5. Function F2.2 is quantified by considering a typical stability and pointing requirements for an Earth observation satellite.

Firstly, the best Ground Sampling Distance (GSD) achievable on a PocketQube platform is estimated as 8 [m], based on twice the diffraction limit for a telescope with an aperture diameter of 4 [cm]. The satellite should be

pointed to within 20% of the GSD for the time it takes to fly over the same area. Simply relating the change in pointing angle and the specified time period to a maximum acceleration, in combination with the satellite's moment of inertia yields a motor torque error limit of 0.0041 [Nm].

Secondly, over half an orbit the satellite should point to within 10% of its Field of View (FoV). This translates to a maximum deviation in angular velocity, and a momentum error limit of about 0.134×10^{-7}. Combined with the momentum of inertia of the motor plus flywheel derived in Chapter 6 this yields a speed error limit of about 300 [RPM]. Furthermore, over one orbit the wheel speed will increase as disturbances are countered. It is crucial to know the rotation speed of the wheel so that saturation can be prevented. It is assumed that knowing the rotation speed to within 10 [RPM] is sufficient.

4.2. Characteristics

After considering the interfaces and functions, the required characteristics of the reaction wheel are derived in this section. Technical characteristics typically include interfaces and internal aspects such as physical limitations and the internal configuration.

Interfaces identified in Section 2.2 must be translated to specific requirements, where possible. A very important interface is the disturbances produced by the reaction wheel, which impact other reaction wheels, other actuators, sensors, and the entire PocketQube. Apart from stability criteria derived in the previous section there is no limit on disturbances, unless they interfere negatively with another component. For example, in the Delfi-n3Xt reaction wheel assembly design a negative effect of disturbances on the performance of other wheels was observed [22]. As such it is important to characterise these disturbances, which is the subject of Chapter 10. Another similar interface is EMI produced by the motor in the reaction wheel. However, as is discussed in Chapter 9 the motor is surrounded by a housing, which shields against such interference. The subject of commands and power is more directly related to the development of the control electronics, which lies outside the scope of this thesis. However, the reaction wheel should operate on the bus voltage of 3.3 [V].

Physical requirements include mass, volume, structural properties and what types of material are used. Mass and volume requirements are derived from the overall PocketQube technical budgets. Based on a preliminary volume budget the reaction wheel should measure no more than 14x14x8mm. However, with these dimensions the flywheels were sized and manufactured, before it was realised that vacuum rated grease in electric motors leads to much higher friction and therefore power consumption of the motor (this is discussed in Chapter 6). With the required addition of a housing for the reaction wheel the dimensions increased. It was decided to allow for a slightly larger prototype of 20x20x12 [mm], with a view to gather the required information to both optimise the flywheel size and the housing dimensions (see Section 9.2). Similarly, the mass of the RW shall be less than 8 [g] for a first prototype, but should be optimised further in subsequent iterations, ideally to be less than 3 [g]. The reaction wheel should interface with the overall three-wheel assembly, which in turn shall interface with the ADCS of the PocketQube. The flywheel shall be made of bronze, for its high density, easy manufacturability and cheap availability (also used on Delfi-n3Xt wheel).

The configuration of the reaction wheel is specified in the requirements, no further quantification is required.

4.3. Constraints

Along with what the reaction wheel does and what it is, it is important to consider under what constraints it must perform its tasks. Physical requirements are in principle also constraints, but in this section a constraint is an external factor that influences the performance of the wheel. A distinction is made between the launch and space environment.

During launch the reaction wheel experiences vibrations transmitted from the launch vehicle via the PocketQube to the wheels. Currently, no launch vehicle has been selected and it is decided to qualify the RW for the largest expected vibrations during launch. The qualification levels and frequencies are shown in Section 11.5.

In space the reaction wheel must contend with vacuum, zero-g, radiation and temperature changes. Radiation

is typically not accounted for in very small satellite programs as radiation hard processors are not available. Regardless, this requirement is is only relevant for the drive electronics. Both vacuum and zero-g are important for the electric motor, because standard grease evaporates in vacuum, and ball bearings float in their races and cages. The effects of changes in temperature on the electric motor are analysed in Section 5.5.

4.4. Reaction wheel requirements

Based on the rationale of the preceding sections the requirements for the reaction wheel are given in this section. At the highest level the functional requirements define the capabilities of the reaction wheel, and the mission requirements define its operational environment. At the systems level, i.e. the complete RW assembly, these requirements are broken down and quantified.

Top level requirements

Functional requirements

SYS-F1. The RW shall be able to generate torque around its rotation axis.
SYS-F1.1 The RW shall be able to accelerate/decelerate to counter disturbances.
SYS-F1.2 The RW shall be able to accelerate/decelerate at the required rate over its operational speed range.
SYS-F2. The RW shall be able to store angular momentum around its rotation axis.
SYS-F2.1 The RW shall be able to counter the total disturbance momentum over one orbit.
SYS-F2.2 The RW shall be able to control its speed.
SYS-F2.3 The RW shall be able to determine its rotation speed.

Mission requirements

SYS-M1. The RW shall survive the PocketQube operational environments.
SYS-M2. The RW shall operate within PocketQube constraints.
SYS-M3. The RW shall have a lifetime of one year.
SYS-M4. The RW shall support Earth-observation and propulsive manoeuvres.

System level

Performance requirements

SYS-PE1. The RW shall be able to store at least 1.1×10^{-4} [Nms] angular momentum about its rotation axis in one direction of rotation.
SYS-PE2. The RW shall be able to generate at least 2.93×10^{-7} [Nm] of torque around its rotation axis over its operational speed range.
SYS-PE3. The RW shall not generate instantaneous disturbance torques larger than 0.0041 [Nm].
SYS-PE4. The RW shall not have a momentum error of larger than 3.182×10^{-5} Nms over half an orbit.
SYS-PE5. The RW shall be able to determine its rotation speed to within 10 [RPM].
SYS-PE6. The RW shall have a nominal power consumption of 15 [mW].
SYS-PE7. The RW shall have a lifetime in space of at least one year.

Physical requirements

RW-PH1. The housing shall provide structural support for the motor and flywheel.
RW-PH2. The housing shall contain an airtight sealed environment with one atmosphere pressure.
RW-PH3. The RW shall weigh less than 8g.
RW-PH4. The RW shall ideally measure less than 14x14x8 [mm], but for a first design it shall measure less than 20x20x12 [mm].
RW-PH5. The RW shall have an eigenfrequency above 60 Hz [8].

Environmental requirements

RW-EN1. The RW shall be able to operate between -15 and 45 degrees Celsius.
RW-EN2. The RW shall be able to operate in vacuum.
RW-EN3. The RW shall be able to withstand the radiation environment in Low Earth Orbit.
RW-EN4. The RW shall be able to survive accelerations during launch with a root mean square value of 7.2 [g] [8].

Interface requirements

RW-IN1. The RW shall operate with the bus voltage of 3.3 [V].

Table 4.1: Requirements verification tests

Test type	Test equipment	RW model type	Requirements to verify
Motor functional test	Control electronics Power supply Oscilloscope Multimeter	Motor Motor with flywheel	P1 - P6, P7 I1
Vibration test	Signal generator Power amplifier Shaker Accelerometer	RW	E4 PH1, PH5
Vacuum test	Vacuum chamber Pressure sensor Data acquisition unit	Housing	E1, E2
Microvibration test	see Chapter 10	RW	P3 I4
Simple tests	Scale Ruler	Components RW	PH3, PH4
Not experimentally verified			E3 I3

RW-IN2. The RW shall have a structural interface with the ADCS system.
RW-IN3. The RW shall not generate electromagnetic disturbances that interfere with other subsystems.

4.5. Requirements Verification and Validation plan

In this section the approach to verify and validate the design is presented. Furthermore, verification of the requirements themselves, i.e. answering the question whether they are the right requirements, is considered.

The tests and methods required to verify the design are shown in Table 4.1. Compliance with functional requirements is implicit in proving compliance with performance requirements. Three requirements are not verified experimentally within the scope of this thesis. Electromagnetic interference is assumed negligible because of the reaction wheel housing's shielding effect, and the radiation environment is not important for the reaction wheel itself. It is, however, relevant for the drive electronics. The lifetime performance of the reaction wheel should be tested after the engineering model has been verified, and so lies outside the scope of this thesis.

Validation of the design is not performed in this thesis. The wheel cannot be tested in a representative environment, as neither dedicated control electronics nor the ADCS of the PocketQube has been developed. However, the requirements can be verified by considering their completeness and content and establishing that they are the correct set of requirements with respect to the need of the PocketQube for 3-axis stabilisation. Completeness is assessed by consulting ESA standards, checklists for requirements, and the requirements for the Delfi-n3Xt reaction wheel [22]. In comparison with ESA standards the requirements are not complete, however it was judged that in a bottom-up engineering approach the agility of a minimal approach outweighs the assurance of a rigorous set of requirements. Instead, the comparison focused on whether any important requirements were missing to develop a prototype. Apart from this, the requirements must be logically coherent internally. For this reason a traceability matrix of all requirements was used to search for missing requirements by following their logical breakdown (Appendix B). It also includes the component level requirements that are presented at the beginning of their relevant sections.

4.6. Chapter summary

In this chapter requirements at RW level were derived by considering the capabilities expected of a reaction wheel, the characteristics it should have and constraints under which it operates. At the highest level functional requirements define exact functions and mission requirements specify the operational environment within the PocketQube satellite. On a systems level performance requirements quantify how well functions should be performed while physical requirements define measurable quantities that drive the RW's structural design and

configuration. Environmental requirements define the external operational environment of the satellite and interface requirements specify how the reaction wheel fits inside the PocketQube. A requirements verification plan was established detailing which tests are required to verify the design. The completeness and internal logic of the set of requirements were assessed through comparison with existing requirements, and a requirements traceability matrix. In the following part of this report a preliminary design is created and evaluated based on the derived requirements.

II

Preliminary design

5

Electric motor selection

The basis of the RW is its electric motor. It controls the speed and acceleration of the reaction wheel and is the major contributor to its power consumption. This chapter presents the analysis and selection of the electric motor that will drive the reaction wheel. First, the requirements for the motor are given in Section 5.1. Different electric motor types are then considered in Section 5.2. Brushless Direct Current (BLDC) motors are then analysed in detail in Section 5.3. Results of a comprehensive search for available motors are given in Section 5.4 and a motor is selected in Section 5.5.

5.1. Motor requirements

Requirements for the motor are derived from the system level requirements (see Appendix B for traceability). Rotor position sensors are required to determine the rotation speed of the motor. As will be discussed in Section 5.2 DC motors do not require these for operations, while BLDC motors do. Whether the requirement can be relaxed in the case of DC motors depends on how well their speed can be determined from the supply voltage duty cycle. The maximum speed of the motor directly drives the mass of the flywheel and it should deliver the required minimum torque over its operational speed range.

COM-M1. The motor shall have a nominal power consumption of 12 [mW].
COM-M2. The motor shall have rotor position sensors.
COM-M3. The motor shall have a mass below 1 [g].
COM-M4. The motor shall have a maximum speed as high as possible.
COM-M5. The motor shall operate between -15 and 45 degrees celsius.
COM-M6. The motor shall have maximum dimensions of 14x14x7.5 [mm].
COM-M7. The motor shall have a linear torque-speed relationship.
COM-M8. The motor shall operate at 3.3 [V].
COM-M9. The motor shall survive launch accelerations of 7.156 [g] (RMS).
COM-M10. The motor shall have a lifetime of at least 1 year.

5.2. Electric motor types

Many different types of electric motors exist. For RW applications a linear torque response, high efficiency and long lifetime are desirable and therefore RWs are typically driven by Permanent Magnet Synchronous Motors (PMSM) or Brushless Direct Current (BLDC) motors [11]. Novel applications such as ultrasonic motors have been proposed [46] to prevent magnetic disturbances on other subsystems and eliminate the need for a housing and lubricant to maintain the reaction wheel. However, for a highly miniaturised reaction wheel efficient and affordable motors must be commercially available.

Both BLDC motors and DC motors are considered as they produce a linear torque response and are readily available. Their main difference is their commutation principle. Brushed motors have a physical connection between the rotating (rotor) and the stationary part (stator) which is used to control the switching of the drive circuit. Brushes make contact and conduct electricity between the parts at certain orientations such that current flow generates the required magnetic field to rotate the rotor. BLDC motors are electronically commutated.

The switching of the drive circuit is controlled by sensing the position of the rotor using Hall sensors, or optical encoders.

Brushless DC motors have a range of advantages over brushed motors at the cost of increased complexity and cost. They allow precise torque control and are small compared to other motors [24]. BLDC motors have a higher lifetime because they have fewer moving parts that can wear out over time. In addition, DC motors can produce more electromagnetic interference due to brush arcing. Because of the aforementioned advantages the brushless motor type is considered primarily. However, due to their widespread use in miniaturised systems (e.g. smart phones), DC motors cannot be neglected without analysis.

5.3. Ideal motor performance

First, the maximum speed at which the minimum required torque can be delivered is calculated for each motor. Subsequently the required flywheel size and total mass of the motor and flywheel combination are determined. Finally, the effect of launch loads is evaluated. The maximum speed of the motor can be derived from its power consumption, i.e. the current and voltage in its windings:

$$P = V \times i \tag{5.1}$$

As the permanent magnets on the rotor rotate, a back electromotive force (EMF) is induced in the motor windings opposing the supply voltage. At every voltage, there exists a rotation speed where the back EMF equals the supply voltage and the motor will only rotate at that speed. The motor is said to be self-regulating. The back EMF constant k_e describes how much voltage is induced at a given speed. In addition to the back EMF there is a voltage drop due to the resistance of the motor phases. The voltage and current are therefore given by:

$$V = k_e \times \omega + i \times R \tag{5.2}$$

$$i = \frac{V - k_e \times \omega}{R} \tag{5.3}$$

The current flowing through the phases determines the torque produced by the motor. At a specific supply voltage a certain no-load speed is reached, where the back EMF equals the supply voltage. The motor draws a certain amount of current to overcome the friction torque at this speed, resulting in zero net torque. To deliver additional torque the motor needs to draw more current. The current therefore has two components: i_0, the no-load current and i_a, the additional current.

$$i = i_0 + i_a \tag{5.4}$$

Next to the back EMF constant, the torque constant describes how much torque is produced per unit of additional current.

$$T = k_t \times (i_a) = k_t \times (i - i_0) \tag{5.5}$$

Substituting for i in eq. (5.3) yields:

$$T = k_t \times \left(\frac{V - k_e \times \omega}{R} - i_0 \right) \tag{5.6}$$

From this equation the maximum speed can be obtained by solving for ω:

$$\omega_{max} = \frac{V - (\frac{T_{min}}{k_t} + i_0) \times R}{k_e} \tag{5.7}$$

R is the resistance of two windings (current flows through two windings at any given point) and T_{min} is the required minimum torque derived in chapter 3. The friction is approximated here using the no-load current

provided in the data sheet. In reality the friction changes with rotor speed. Furthermore, there are power losses due to for example switching effects that are ignored here (see Section 7.5).

Next, the size of the flywheel is determined. The required moment of inertia of the wheel is derived from the required angular momentum storage. The angular momentum of the rotor at maximum speed, including a margin of 25% is:

$$H_{store} = \omega_{max} \times 0.75 \times \frac{\pi}{30} \times I_{motor} \tag{5.8}$$

The total required moment of inertia is:

$$I_{required} = \frac{H_{minimum}}{\omega_{max} \times 0.75 \times \frac{\pi}{30}} \tag{5.9}$$

The moment of inertia of the disk is then:

$$I_{disk} = I_{required} - I_{motor} >= 0 \tag{5.10}$$

Assuming a perfectly shaped disk made of bronze the mass and thickness of the disk and motor combination can be calculated as:

$$m_{disk} = \frac{I_{disk} \times 2}{(\frac{D_{max}}{2})^2} \tag{5.11}$$

$$t_{disk} = \frac{m_{disk}}{\rho \times (\frac{D_{max}}{2})^2 \times \pi} \tag{5.12}$$

$$M_{total} = m_{disk} + m_{motor} \tag{5.13}$$

Finally, the launch loads on the motor shaft as a percentage of the maximum allowed load is calculated as:

$$F_{shaft} = m_{disk} \times a_{launch} \tag{5.14}$$

$$F_{launch} = \frac{a_{launch} \times m_{disk}}{F_{shaft}} \times 100 \tag{5.15}$$

Calculating the launch loads on the motor shaft for the Delfi-n3Xt reaction wheel yields a value of 50%. The acceleration value was taken as the root mean square of the maximum acceleration during launch. This motor was successfully vibration tested so this equation is considered a good first indication of whether the motor can handle the launch loads. However, it only considers vibrations in the direction of the motor shaft and ignores the structural response of the reaction wheel assembly.

5.4. Search results

Effort was made to conduct a comprehensive search of available BLDC motors (see Appendix C). Unfortunately no motor meeting the strict power requirement was found. The brushless motors that best comply with requirements are shown in Figure 5.1, and brushed motors in Figure 5.2.

Figure 5.2 shows that multiple brushed motors comply with the power requirement, however they rotate at lower speeds and therefore require a larger flywheel, leading to larger loads on the motor axle during launch. It should be noted that for 086G1 105 and 086G1 107 shaft load limit values are not available. However, since, they also have the slowest rotation speed they require the largest flywheels and it is probable that they would not survive the launch loads.

Available brushless motors do not meet the power requirement, but do meet the mass and launch load requirements. This is because they can rotate faster due to their brushless design, and so a lighter flywheel can store the minimum angular momentum. Their higher power consumption is simply because their nominal velocities

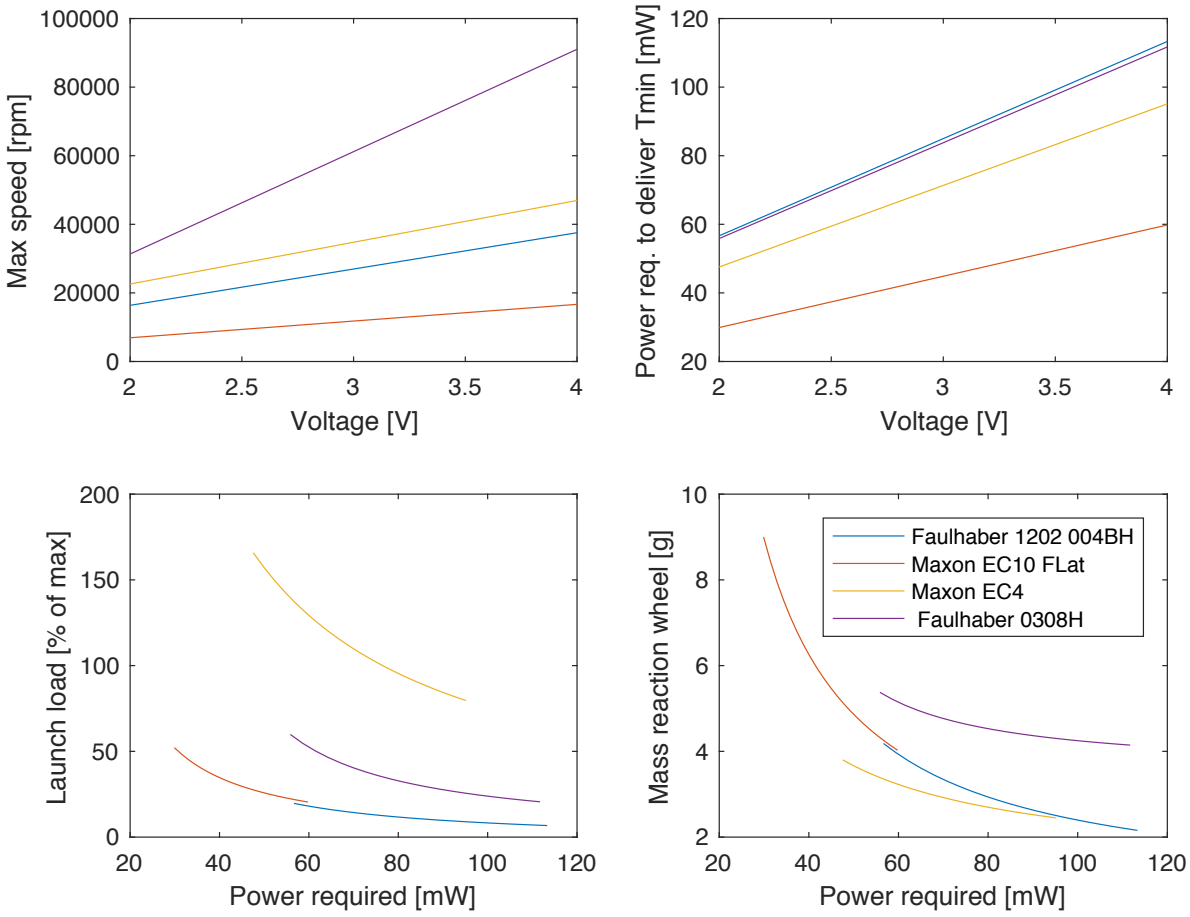

Figure 5.1: Performance of most suitable brushless DC motors

are much higher. In conclusion, a large speed is desirable to achieve low enough mass to survive launch conditions, but this is problematic in terms of power consumption.

It is not fundamentally impossible for a brushless motor to meet the specific requirements. A suitable motor should either have a larger rotor inertia at the cost of delivering less torque to eliminate the need for a flywheel, or it should have a smaller rotor and less friction. In fact, one suitable university-developed brushless motor design was identified [14], however the manufacturing cost alone of this motor was prohibitive.

The power consumption is a killer requirement, but considered alternative options do not offer better performance. Simply using a motor with a larger rotor, thus eliminating the need for a flywheel, is not possible due to power, mass and volume requirements. Using a momentum wheel instead of a reaction wheel to stabilise the PocketQube requires a much heavier flywheel, and so is also not possible considering launch loads. However, it might be possible to stabilise the PocketQube using one or two reaction wheels only.

5.5. Motor selection

Although the power consumption proves problematic, it was decided to continue development with the most suitable motor to measure the power consumption over the whole speed range and validate a model of the motor. This allows to provide a quantitative basis for conclusions about the feasibility of using reaction wheels for picosatellite applications (see chapter 12).

A graphical trade-off is performed to select the best motor option, after which the selected motor is analysed for temperature effects. This is a lesson learnt from the Delfi-n3Xt reaction wheel design [22], where the final design did not comply with all performance requirements over the complete temperature range.

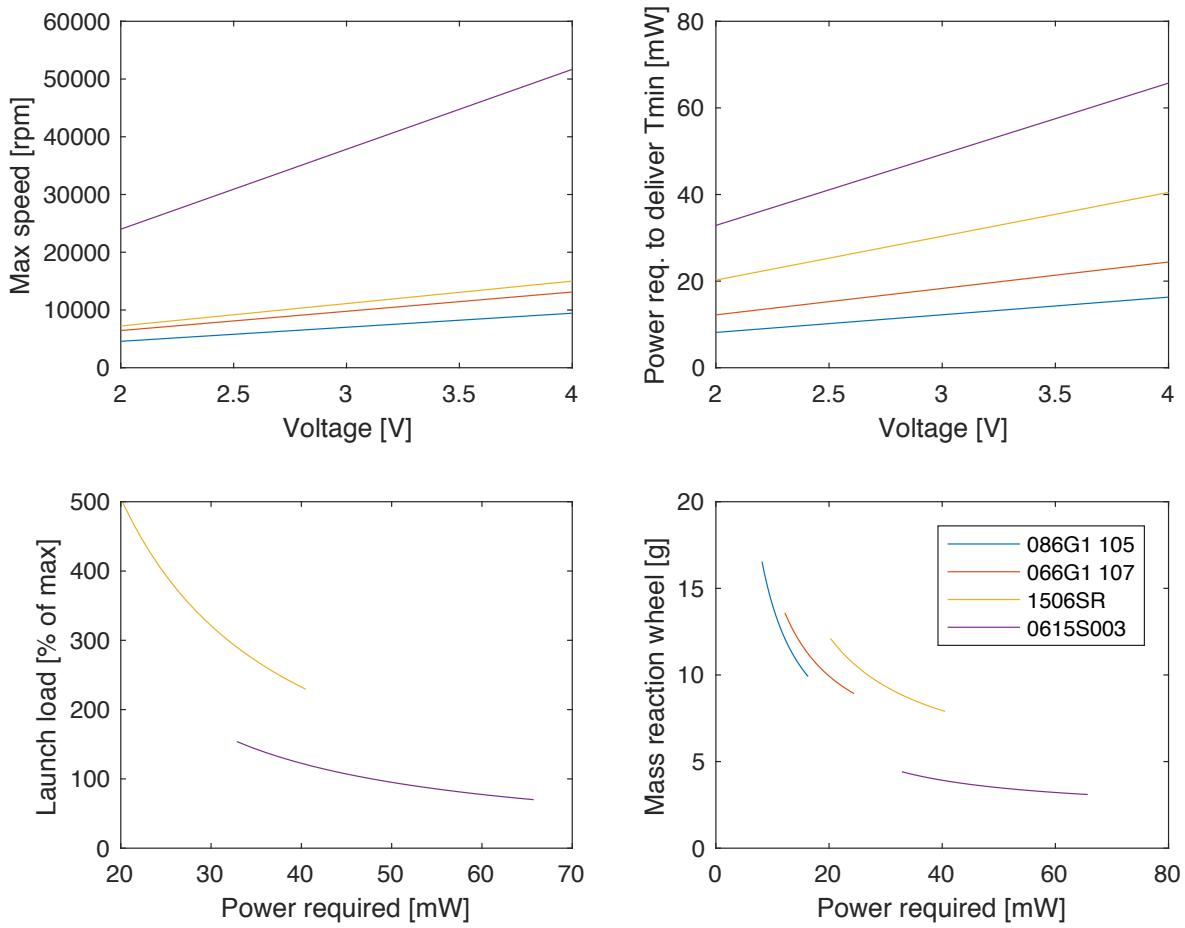

Figure 5.2: Performance of most suitable brushed DC motors

Graphical trade-off

A trade-off is performed to select the best suitable motor based on objective criteria. The trade-off table is shown in Table 5.1. The trade-off criteria are chosen to be independent of each other. A graphical approach is chosen because of the strong asymmetry in compliance due to the power requirement. The power consumption criterion refers to the power required to deliver the minimum required torque at the maximum useful speed. The limit for compliance with the mass criterion is set at 5 [g], which considering the 8 [g] overall mass requirement for the reaction wheel is reasonable. The Maxon EC10 Flat motor is selected because it has by far the lowest power consumption of the motors that comply with all requirements.

Analysis of temperature effects

The performance of the selected motor is analysed further. Including temperature effects in the preliminary design is a lesson learnt from the Delfi-n3Xt reaction wheel design.

Two main temperature dependent parameters can be identified [33]: resistance of the motor windings and the magnetic flux density of the permanent magnets on the rotor. At higher temperatures resistance increases which reduces the current flowing through the windings. This limits the torque generating capability of the motor, effectively reducing the torque constant. Furthermore, reduced magnetic flux density also leads to lower torque generated per unit of current as magnetic force is proportional to magnetic field strength. On the other hand, the decreased flux density leads to less Back EMF induced in the windings, which results in a larger no-load speed. At a certain temperature limit the windings are destroyed as their insulation deteriorates, and

Table 5.1: Graphical trade-off table motor selection

Electric motor	Power consumption [mW]	Rotor position sensors	Mass flywheel and motor [g]	Launch load [% of allowable shaft load]
BLDC motors				
Faulhaber 1202004BH	93.5 red	Yes green	2.5 green	9.2 green
Maxon EC10 Flat	49.3 orange	Yes green	4.9 green	26.2 green
Maxon EC4	78.5 red	Yes green	2.7 green	97.4 red
Faulhaber 0308H	92.2 red	Yes green	4.3 green	26.7 green
DC motors				
Precision Microdrives 086G1105	13.5 green	No red	11.3 red	N/A red
Precision Microdrives 086G1107	20.1 red	No red	9.9 red	N/A red
Faulhaber 1506 SR	33.4 red	No red	8.8 red	284.8 red
Faulhaber 0615S003	54.2 red	No red	4.4 green	86.8 orange

Legend	
green	compliant
red	not compliant
orange	best of type not compliant

no magnetic field can be generated. Similarly, at the magnet material's Curie temperature they permanently demagnetise. The Maxon EC10-FL motor has a maximum operating temperature of 100 degrees Celsius.

Both effects are typically modelled as linear deviations from a reference value, where it is more convenient to work with a deviation from the torque constant, than with the flux density, in eq. (5.16) and eq. (5.17). Here α_{copper} and α_{k_T} are the temperature coefficients of copper and the magnetisation loss constant, respectively. Both are available from manufacturer data [37]. The temperature dependent performance of the selected Maxon EC10 Flat motor is shown in Figure 5.3. Noticeably the power consumption appears temperature independent. This is because the minimum torque requirement is so small that efficiency losses are small compared to the power required to run the reaction wheel at no-load. Because of the reduced torque constant the maximum useful speed decreases, which leads to a larger flywheel. This analysis ignores the possibility of temperature changes affecting the no-load speed. Complete temperature cycling tests are recommended for future work (see Chapter 12).

$$R_T = R_{25} \times (1 + \alpha_{copper} \times (T - 25)) \tag{5.16}$$

$$k_T = k_{25} \times (1 + \alpha_{k_T} \times (T - 25)) \tag{5.17}$$

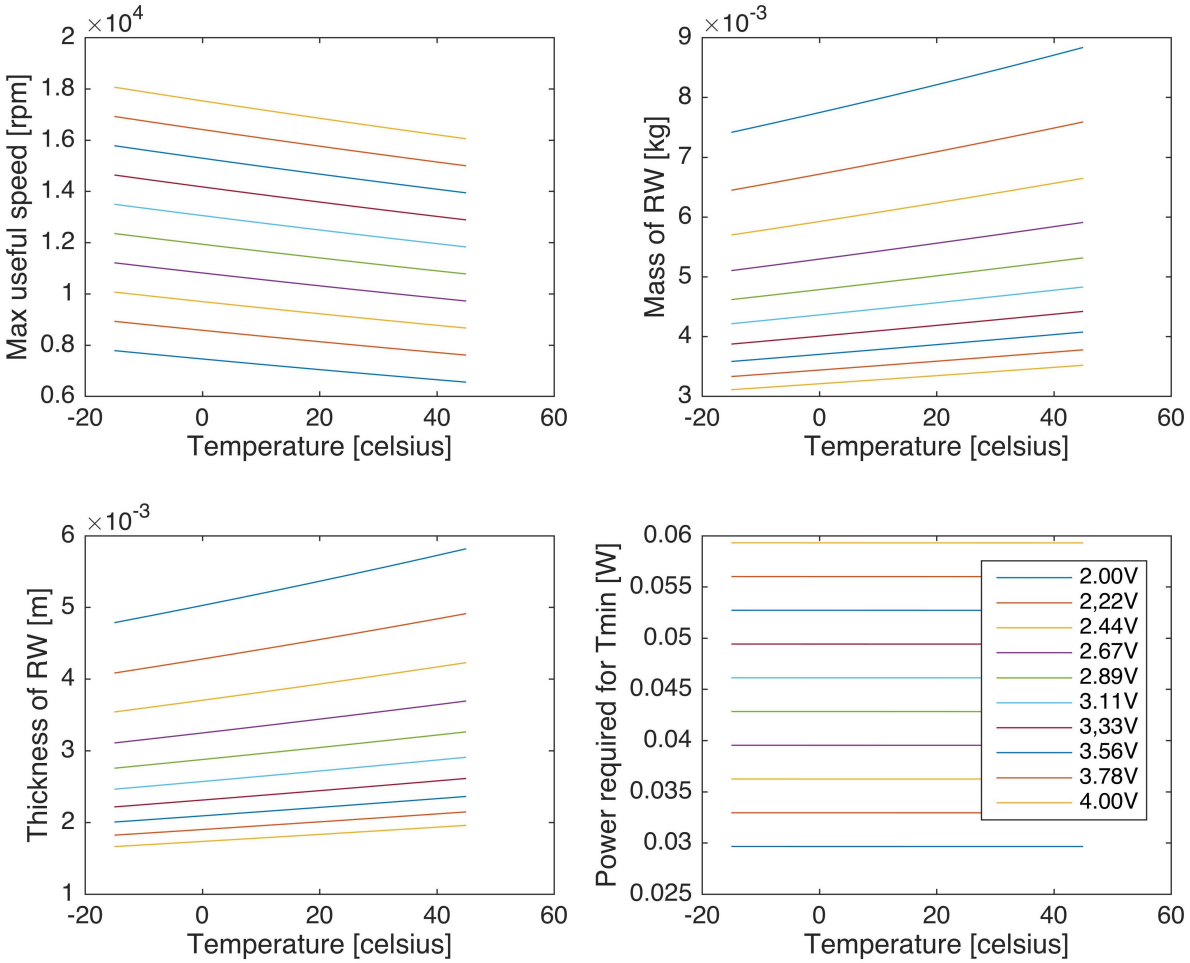

Figure 5.3: Performance of EC10 Flat motor

At the bus voltage of 3.3V and 25 degrees the thickness of the disk should be 2.5 [mm] for a max diameter of 14 [mm]. For colder operations the wheel will have a larger useful speed as can be seen in the figure and will

thus have a larger momentum storage capacity. For temperatures above 25 degrees the opposite will occur. The maximum deviation in maximum useful speed between 25 and 45 degrees is 6%. However, keeping in line with the lessons learnt from the Delfi-n3Xt reaction wheel design a 25% margin on the maximum useful speed is included.

5.6. Chapter summary

The ideal performance of BLDC and DC motor types was analysed in this section to select a suitable electric motor that complies with the component level requirements given at the beginning of the chapter. Results of an extensive search of available motor options were presented and the most suitable motor was selected using a graphical trade-off method: Maxon EC10 Flat. However, this motor does not comply with the power requirement, but it is the best available option. Further analysis of temperature effects showed that the motor complies with performance requirements within the temperature environment on-board the PocketQube. A preliminary design of the hardware of the RW that will accommodate the motor is created in the next chapter.

6

Preliminary Hardware Design

A preliminary design for the reaction wheel is presented in this chapter. Because of the highly miniaturised nature a simple design is chosen to facilitate manufacturing, handling and integration. Once a proof-of-concept has been established, more advanced designs can be considered. For example, high-temperature superconductor bearings have been used in small satellite reaction wheels to reduce power consumption by eliminating bearing friction [35]. However, power savings are offset by the energy required to cool reaction wheels. Permanent magnet bearings [54] do not require cooling, but must be actively controlled and presently have mass overheads due to their complexity. Another novel concept is a variable inertia reaction wheel that provides in-flight flexibility [12], but increased complexity also results in increased mass of the system. These novel concepts must first be used successfully in space before they can be miniaturised for use on nano- and picosatellites.

6.1. Flywheel

Based on the physical requirements established at RW level the requirements of the flywheel are derived:

COM-FL1. The flywheel shall have a maximum diameter of 14 [mm].
COM-FL2. The flywheel shall have a thickness such that it has a moment of inertia of 0.8 [gcm^2] .
COM-FL3. The flywheel shall be mounted on the rotor axle through pressfitting.
COM-FL4. The flywheel shall be manufactured out of bronze (ρ = 8950 [$\frac{kg}{m^3}$]) with a precision of better than 0.1 [mm].

The flywheel was sized in parallel with the selection of the motor in Section 5.3: it has a thickness of 2.5 [mm] for a diameter of 14 [mm]. It should have the simplest possible shape to reduce wheel imperfections and imbalances, which is a lesson learnt from the Delfi-n3Xt reaction wheel design [22]. Furthermore, it will be made of bronze as this material has a very high specific density of 8950 [$\frac{kg}{m^3}$], can be manufactured easily and is not expensive. Bronze is, however, slightly conductive and so the time-varying magnetic fields inside the brushless motor will induce some eddy currents, but this effect is typically small for a highly miniaturised motor. It is acknowledged that no complete survey of materials was performed, which could be the subject of future work, perhaps as part of a literature study (see Chapter 12). The flywheel can be pressfit onto the motor axle, and so should have a precisely centred hole on its rotation axis. The specifications of the motor and flywheel are given in Table 6.1.

Table 6.1: Motor and flywheel specifications

Motor type	**Maxon EC10 Flat**
Nominal voltage [V]	4
Nominal torque [mNm]	0.25
Max useful speed [RPM]	13257
Nominal power consumption [mW]	59.2
Rotor inertia [$g \times cm^2$]	0.08
Motor mass [g]	0.82
Dimensions [mm]	10x10x6.5
Flywheel inertia [$g \times cm^2$]	0.8
Flywheel dimensions [mm]	14x14x2.8
Flywheel mass [g]	2.88
Flywheel material	Bronze

6.2. Support structure

The motor must be clamped to a structure, that in turn can be integrated with the ADCS. At present, no structural designs of the ADCS exist, and for the preliminary design the focus lies on how to clamp the motor securely.

Figure 6.1 shows a design model of a clamp which can be tightened simply with a nut and bolt. It weighs 0.56 [g] if made out of aluminium and measures 14 [mm] in the widest part and 5 [mm] in height.

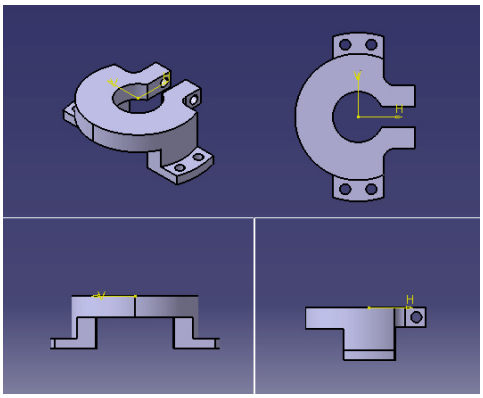

Figure 6.1: Preliminary motor clamp design

6.3. Preliminary verification of design

The preliminary reaction wheel design consists of a flywheel press-fitted to a motor, which in turn is clamped inside a supporting structure. This can be mounted on the ADCS PCB. Compliance of the design with respect to requirements is discussed and important conclusions for the detailed design are drawn in this section.
The selected motor complies with most performance requirements based on the analysis of the ideal motor performance in Section 5.3. However, based on the data-sheet no-load current it does not comply with the power requirement. Speed control accuracy was not yet assessed at this stage. The procured motor controller, despite manufacturer's claims, proved incompatible with the motor. For the detailed design the manufacturer provided a different, functioning, controller. In terms of mass and volume the design is compliant as can be seen in Table 6.1. Compliance of the design with environmental requirements was shown through analysis of temperature effects and the launch loads. A vacuum rated lubricant was initially planned for operation of the motor in Space.

After the first motor was procured it was realised that the bottom half of the motor (see Figure 6.2b) is in fact the rotor and rotates with the motor axle. This means the clamp cannot work as it would restrict the motion of the motor. Furthermore, the manufacturer revealed that using vacuum proof bearing grease increases the

power consumption of the motor by a factor of two. This led to two important conclusions.

First, the flywheel can be glued on the rotor, instead of pressfit on the axle, which makes it easier to align it with the axis of rotation. The motor can simply be clamped upside down as the motor axle would not touch the clamp. A simple clamp was 3D-printed in plastic and used to secure the motor during functional testing. It was evident that the clamp has to be very tight to prevent vibrations. Alternatively, the motor can be glued to the support. Both options are considered further. Requirement COM-FL3 is therefore updated to: "The flywheel shall have a shape such that it can be glued on the rotor". The updated design of the flywheel is shown in Figure 6.2a.

Second, the increased power consumption associated with vacuum proof lubricant is unacceptable. The motor must be enclosed by a pressurised housing to prevent evaporation of the bearing lubricant. The clamp can be integrated with the housing to keep the design simple. This led to requirement RW-PH2: "The housing shall contain an airtight sealed environment with 1 atmosphere pressure".

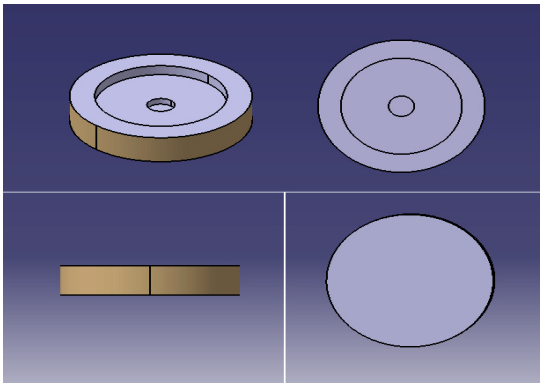

(a) Final flywheel design

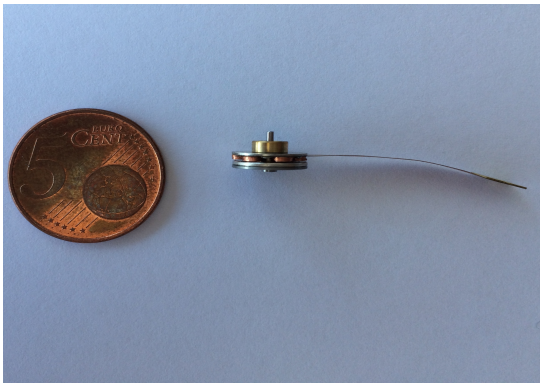

(b) Maxon EC10FL motor

III

Detailed design

7

Motor Electrical Model

Next to the hardware design models of the RW are created to support design and analyse its performance and power consumption in detail. Results are also used for verification purposes. In this chapter, first a performance model of the motor is derived and verified. The BLDC drive circuit and control method are analysed in Section 7.1 and Section 7.2. Subsequently, a simulation model of the drive electronics and motor is derived in Section 7.3 and results are used to verify the model by comparison with data sheet values of the Maxon EC10 Flat motor in Section 7.4. A setup for a sensitivity analysis of the model is discussed in Section 7.6. The second modelling goal is to calculate the power losses of the reaction wheel. This is discussed in Section 7.5.

7.1. Motor drive circuit

As already discussed in Chapter 5 BLDC motors are operated by electrical commutation. A torque is applied on the rotating part of the motor (rotor) through an electromagnetic force between permanent magnets on the rotor and magnetic fields created in the non-rotating part of the motor (stator). Current flowing through coils of wire generates the magnetic fields. Typically BLDC motors have three windings or phases. The position of the rotor determines in which coils and in which direction current should flow. Hall sensors are used to sense the position of the rotor. As the permanent magnets on the rotor move with respect to the coils an electromotive force is induced. This back EMF opposes the supply voltage and reduces the current and so the torque on the rotor. For a given maximum rotation speed the torque becomes zero. The back EMF therefore limits the speed of the motor.

BLDC motors use trapezoidal current waveforms to produce constant torque. For a given predetermined rotation, called the commutation interval, the current flows through two out of the three phases in a specific direction. This is typically described as "*the ampere-conductor distribution of the stator ideally remains constant and fixed in space*" [20][p.273]. As the magnet rotates the phase flux-linkage varies linearly and a constant back EMF is produced. For a constant current a constant torque is produced. The ampere-conductor distribution is switched (commutated) to the next position at the end of the commutation interval.

The operating principle is illustrated by the drive circuit and motoring waveforms in fig. 7.1. The motor windings are typically connected in a so-called wye (or star) connection and the windings are represented by an inductance L_{ph}, Resistance R_{ph} and back EMFs e_1,e_2 and e_3. For each rotor position between 0 and 360 degrees there exists a position of the switching transistors Q1 to Q6 that results in the corresponding currents i_1,i_2,i_3. If the current is flowing through phase one and two in the interval between 30 to 90 degrees, a constant back EMF e_1 and e_2 and Torque T_1 and T_2 are produced. The current in the third phase is zero, but the back EMF induced by the rotation of the rotor is changing linearly. The resulting overall waveform shape is referred to as trapezoidal. Once the rotor has rotated to 90 degrees the transistors are switched and the process repeats [20].

7.2. Control method

BLDC motors are controlled by regulating the current or voltage supplied to the motor windings. Either the signal can be switched on and off rapidly, or its amplitude can be controlled. The former, Pulse-Width Modu-

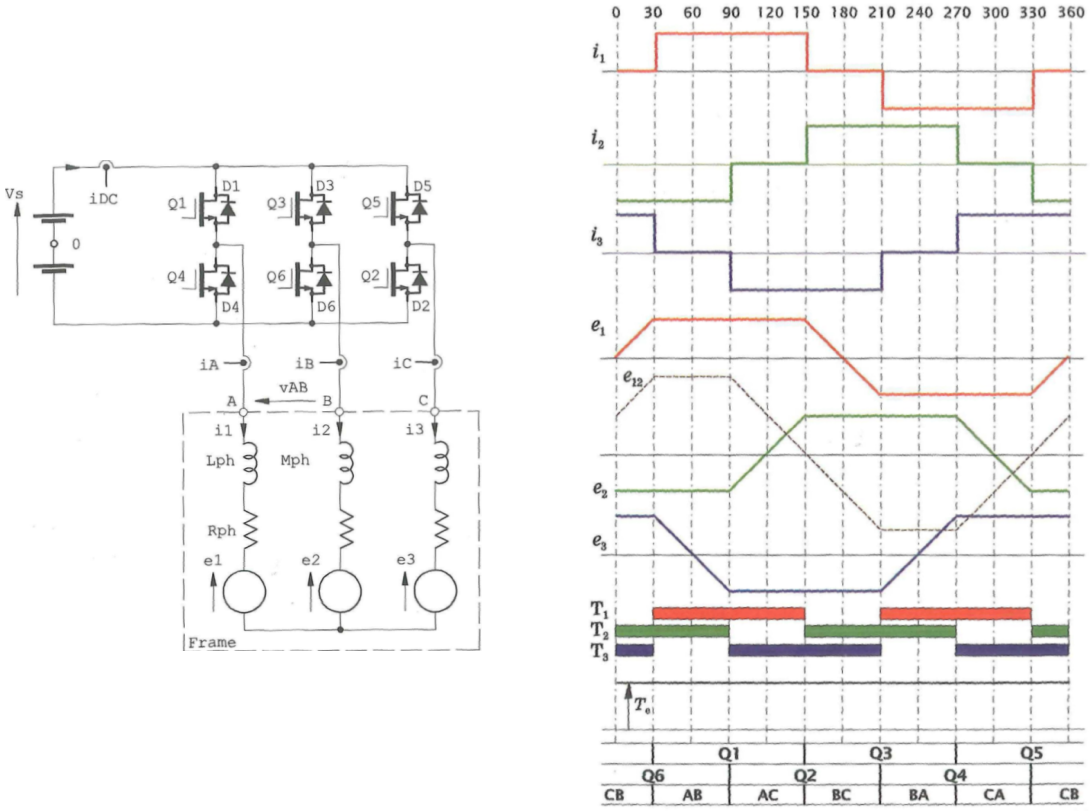

Figure 7.1: a) Drive circuit b) Motor waveforms [20]

lation (PWM), is typically used because of its simple structure [24].

A PWM signal, as seen in fig. 7.3 a), is either 0 or 1. It has a period t_s determined by the switching frequency and the fraction $\frac{t_{on}}{t_s}$ is referred to as its duty cycle. The winding current or voltage can be modulated by switching transistors with a PWM signal. At sufficiently high switching frequencies (typically a few kHz) the average voltage applied is given by $V_{avg} = V_s \times d$, where V_s is the supply voltage. The circuit during chopping of Q1 is shown in fig. 7.2. When a set-point current i_{sp} is required the current flowing through the phases one and two behaves as shown in fig. 7.3 b).

Control strategies differ in whether voltage or current is regulated, and which or both of the interval specific two transistors are chopped. The simplest option for current regulation where the upper transistors are chopped for the 120 degree interval that they are active is considered from now on. This can always be extended in the model if required.

At the end of a commutation interval the transistors are switched and current flows through a different phase combination. However, this does not happen instantaneously as is illustrated in fig. 7.3 c). There is a period when there is current flowing in all three phases as i_C is freewheeling and i_A is building while i_B is constant. Transient analysis of the circuit for each switching pattern can be used to find analytical solutions of the current waveforms. However, while this is beneficial in designing the circuit, it is not considered here. Instead, a circuit built in MATLAB Simulink is used to simulate the switching behaviour in section 7.3. The current waveforms can be used to determine the power consumption of the motor.

7.3. Simulation model

In this section a MATLAB Simulink model of the BLDC motor is presented. The purpose of the model is to model the theoretical power consumption and performance of the motor and control electronics.

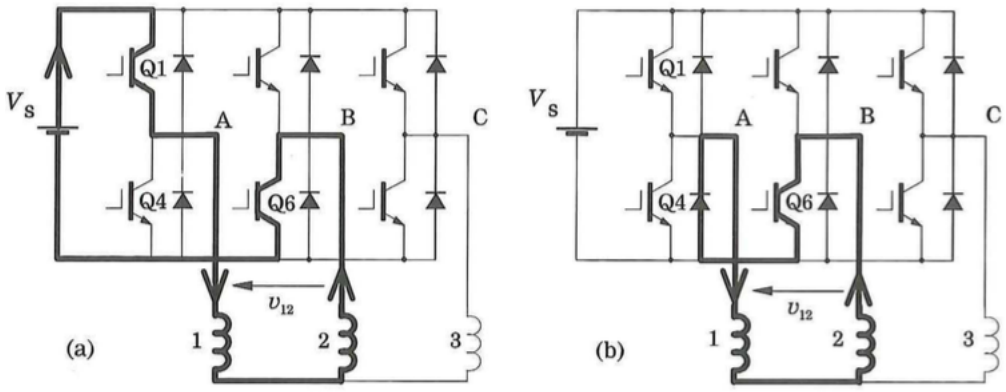

Figure 7.2: Circuit for chopping of Q1 in interval 30-90 degrees (see fig. 7.1)

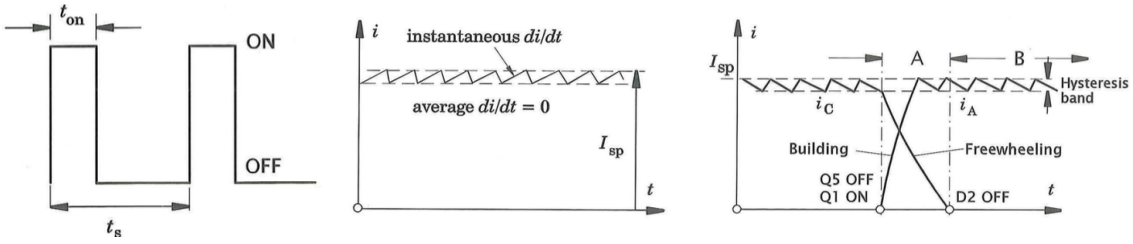

Figure 7.3: a) Pulse-width modulated signal b) Line current c) Commutation of line current [20]

Model overview

The model is created in MATLAB Simulink. It consists of a PWM controller, a drive circuit model and a state-space system of the motor. A block diagram of the model showing links is given in fig. 7.4. This is a simplified overview as some links and aspects are neglected for sake of clarity. The complete model, including all links is depicted in fig. 7.5. Based on the difference between the actual speed and the reference speed the control block determines the required duty cycle, which is passed to the drive circuit. Based on the rotor position the required switching position is determined and the current flowing through the drive circuit is sensed. The electrical torque is calculated by multiplying the current with the back EMF derived from the rotor position and velocity. The back EMF is also an input for the controlled voltage sources in the drive circuit. Additionally, a current limiter is implemented over the drive circuit to prevent extreme current draws during acceleration. The torque is input for the state-space model which calculates the new rotor position and velocity.

PWM control

The speed of the motor is controlled using a proportional–integral controller that, based on the difference between the reference and actual speed, determines the duty cycle for the motor. The Simulink model is shown in fig. 7.6.

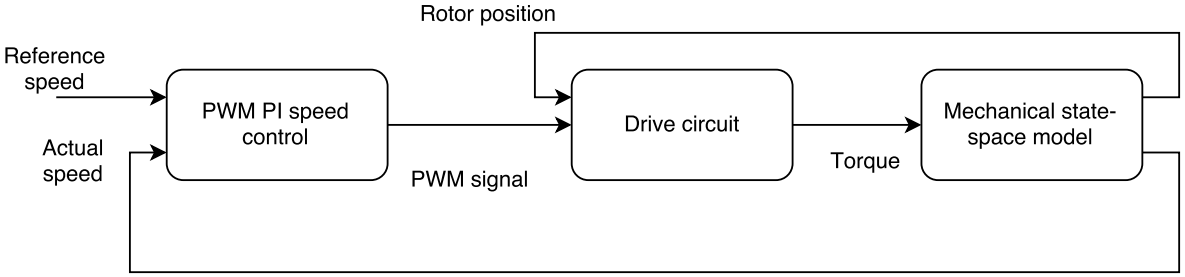

Figure 7.4: Block diagram of BLDC Simulink model

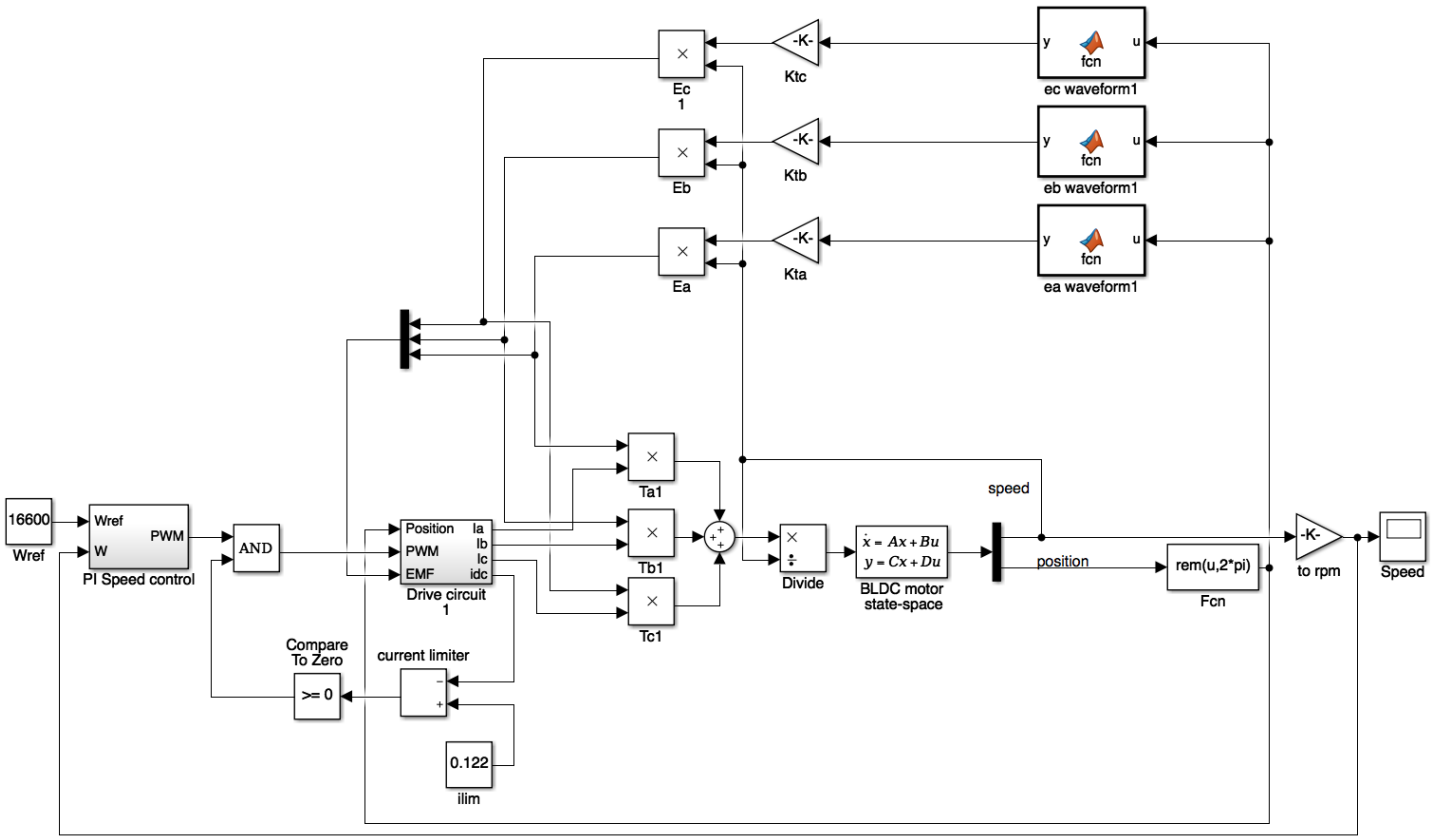

Figure 7.5: Complete MATLAB Simulink model of BLDC motor

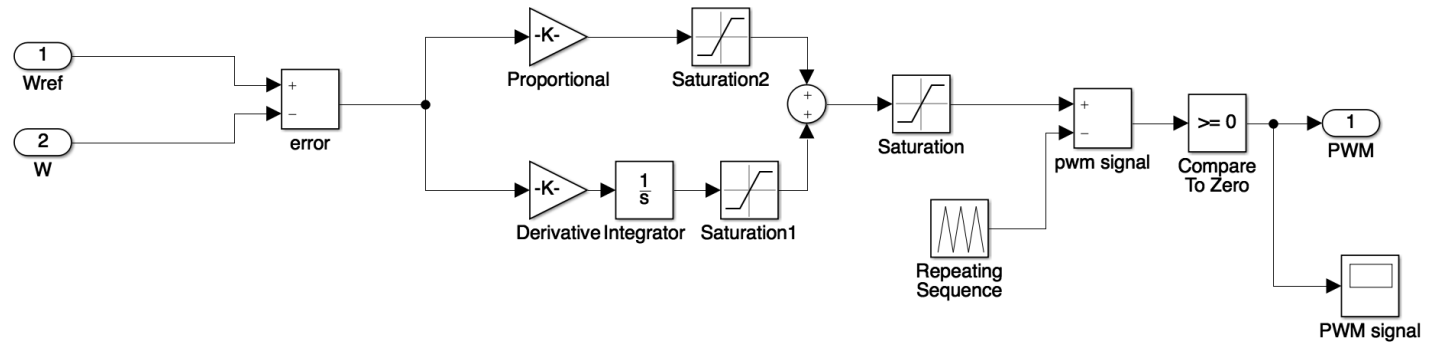

Figure 7.6: PI PWM control

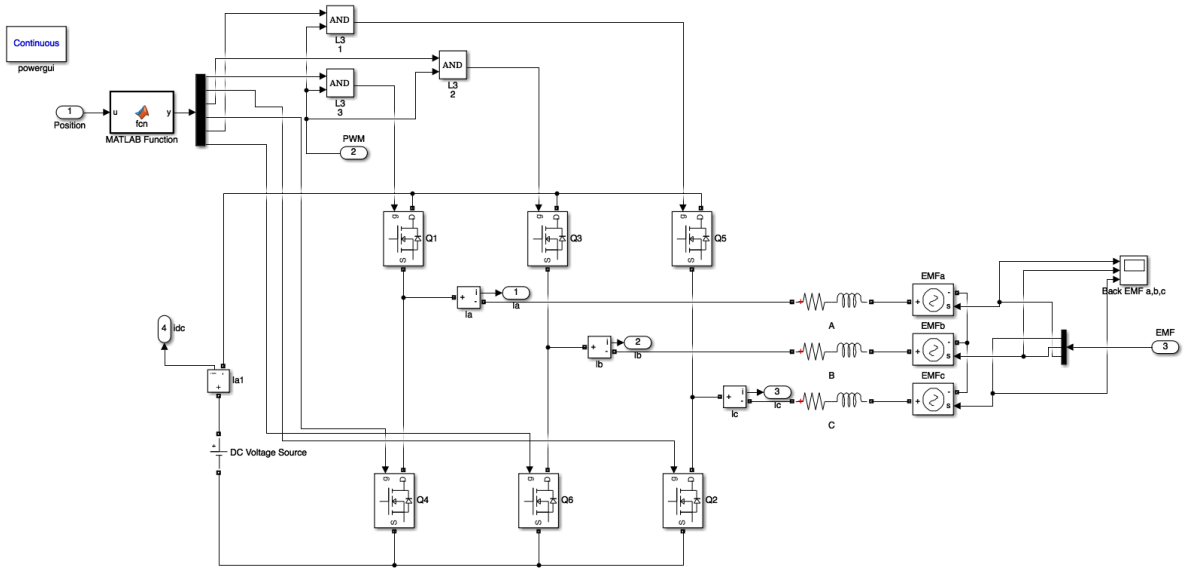

Figure 7.7: Drive circuit model

Drive circuit

The drive circuit in fig. 7.1 is modelled as fig. 7.7. The switches are MOSFET transistors. Based on the rotor position the required switch setting is determined from a MATLAB function. The EMF in the phases is calculated from the speed of the rotor as given by the state space system in section 7.3. The phase currents are sensed and used to calculate the torque input to the state space system.

Mechanical model

The equation of motion for a BLDC motor is given in Equation (7.1) [27]. P is the number of pole pairs in the rotor, B is a friction coefficient, J the rotor inertia, T_e is the electrical torque and T_l is the load torque, which is zero. From this equation a state-space system can be derived as in eq. (7.2) and eq. (7.3). This state space system can be extended to include disturbance torques and more accurate friction models. For now the friction coefficient is determined from the equation of motion for stationary operation at no-load speed and the no-load current, see eq. (7.4).

$$T_e - T_l = J \times \frac{d\omega}{dt} + B \times w \tag{7.1}$$

$$\begin{pmatrix} \omega' \\ \theta' \end{pmatrix} = \begin{bmatrix} -B/J & 0 \\ P/2 & 0 \end{bmatrix} \begin{pmatrix} \omega \\ \theta \end{pmatrix} + \begin{pmatrix} 1/J \\ 0 \end{pmatrix} (T_e - T_l) \tag{7.2}$$

$$\begin{pmatrix} \omega \\ \theta \end{pmatrix} = \begin{bmatrix} 1 & 0 \\ 0 & 1 \end{bmatrix} \begin{pmatrix} \omega \\ \theta \end{pmatrix} \tag{7.3}$$

$$\begin{aligned} T_e &= k_T \times i_o = B \times \omega \\ \Rightarrow B &= \frac{k_T \times i_0}{w_0} \end{aligned} \tag{7.4}$$

7.4. Model verification

The model is verified by comparing results with motor data sheet values. These plots are not representative of actual operating scenarios, which is at a different supply voltage and likely with a stricter current limit. However, these plots illustrate the performance of the motor and are comparable to data sheet values.

The rotor position correctly changes linearly between 0 and 2π as seen in fig. 7.8. Plots for velocity, torque and input and output power are shown in fig. 7.9. The velocity increases to 16424 [RPM], just short of the data sheet

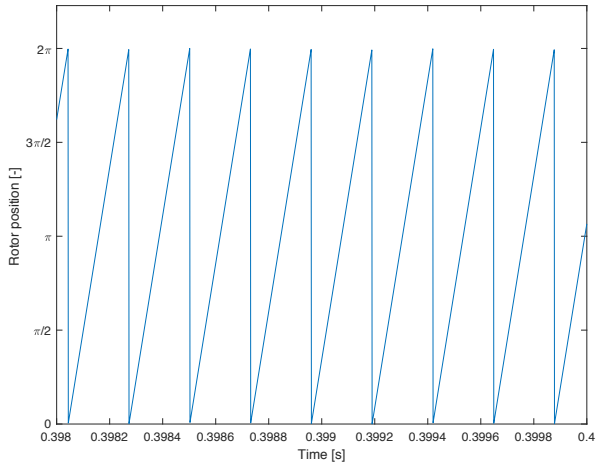

Figure 7.8: Rotor position over time

value of 16600 [RPM]. The maximum torque the motor delivers is about 0.2 [mNm], which is 20% below the nominal torque value of 0.25 [mNm]. The no-load current is correct at 0.0148 [mA] and also the current and back EMF waveforms in fig. 7.10 are as expected. The difference in current waveforms with fig. 7.1 b), is due to switching effects with freewheeling and building currents. The switching effects are also clearly seen in the power and torque plots as the small dips. The maximum efficiency is 39.6 %, which is just below the maximum efficiency of 41% given in the data sheet.

Overall, the model correctly simulates the motor and drive circuit. The difference in torque is difficult to explain without knowledge of the test conditions of the motor. However, to explain the difference the motor has to be tested. The fact that the motor did not reach the no-load speed with the given motor constants indicates inconsistency in the data sheet. Either the torque constant or the no-load current are too large. The physical meaning of this is that either the motor produces less back EMF or there is less friction.

7.5. Power losses

The second goal of the modelling effort is to characterise the power consumption of the reaction wheel and quantify individual sources of inefficiency. Power losses in the motor are calculated from test data and used to tune parameters in the simulation model, which is used to estimate power losses in the drive circuit.

Motor losses

The motor consumes power due to mechanical friction, copper losses and iron losses. Iron losses include eddy current and hysteresis losses. Eddy currents are induced in rotor due to the time-varying magnetic fields created by the electromagnets in the stator. They may cause temperature rise and partial demagnetisation of the magnets [26]. Hysteresis losses are due to a form of inter-molecular friction that occurs inside magnetic materials when subjected to a changing magnetic field [25]. In flat BLDC motors the iron losses are typically included in the mechanical friction as they are strongly speed dependent [37]. A simple friction model is included in the state-space system in the motor Simulink model. The no-load current is measured in motor tests described in Chapter 8. The friction losses are computed from this data using Equation (7.5) and the copper losses are computed using Equation (7.6) for different set speeds. The friction parameter B in the model is then calculated, which is used to update the simulation model.

$$P_{friction} = T_{friction} \times \omega = k_T \times i_0 \times \omega \tag{7.5}$$

$$P_{copper} = i_0^2 \times R \tag{7.6}$$

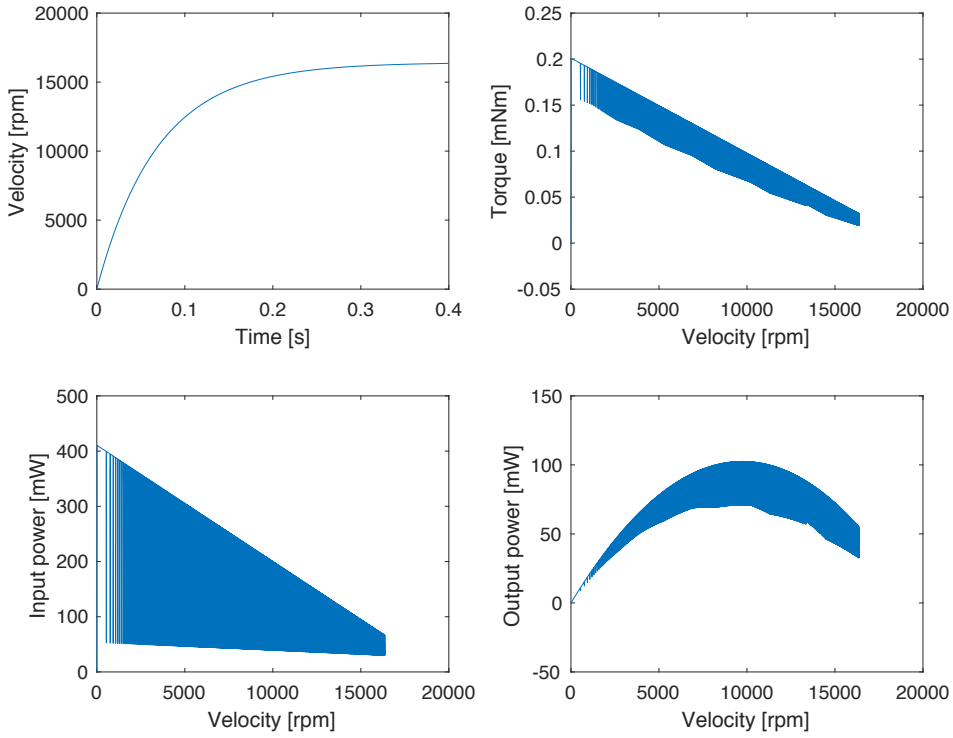

Figure 7.9: Model performance results

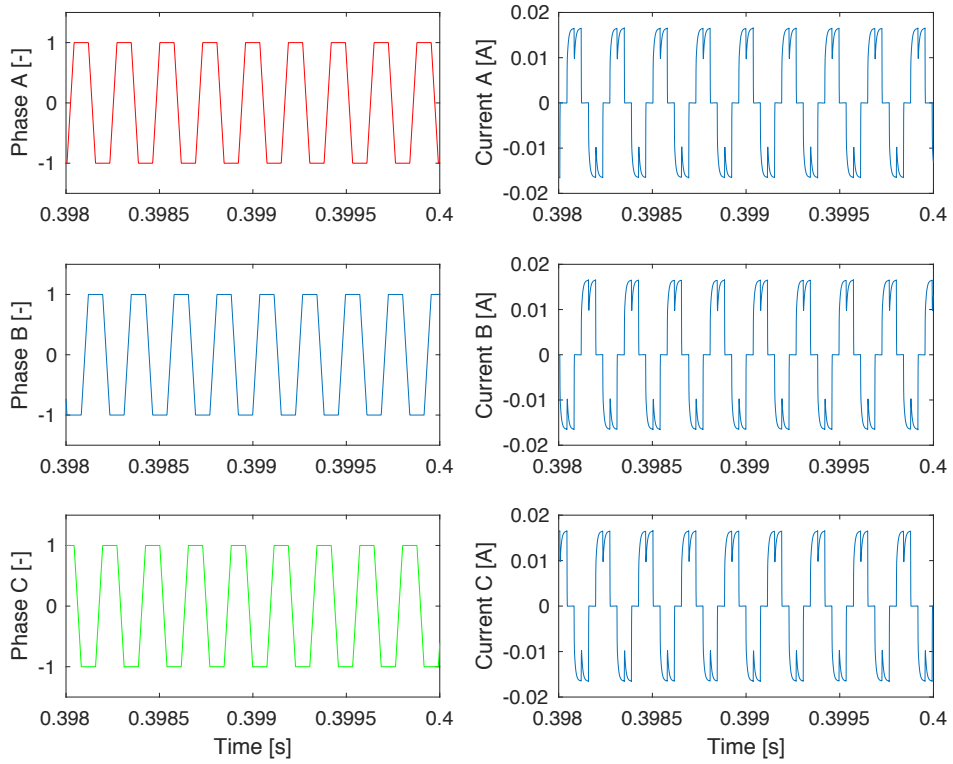

Figure 7.10: Model phase currents and back EMFs

Drive circuit losses

The drive circuit consumes power in the MOSFET switches that guide the current to the right phases, and are switched on and off at the PWM frequency to control the motor speed. Other losses are drive circuit specific. For this analysis it is assumed that the MOSFET gates can be switched by logic-level commands and thus the ADCS processor can drive the switches. Additional circuitry like, for example, a current sensor to generate housekeeping information is not considered either as this is optional.

The MOSFET losses are not straightforward to calculate because they depend on the switching and thermal characteristics of the specific circuit, but some approximations can be made. Basically, there are three operating phases: On, Off and Switching. During the On phase the current flows through the field-effect transistor and in the Off phase the current is dissipating through a flowback diode. Both phases can be modelled as simple conductive losses in Equation (7.7), where the current is obtained in the Simulink model and the resistances and voltage drop are the parameters of the Simulink MOSFET block. A suitable MOSFET has been selected for a preliminary analysis of the drive circuit power consumption: Infineon BSR202N.

$$P_{con} = i_{rms}^2 \times (R_{fet} + R_{diode}) + i_{avg} \times V_{drop} \tag{7.7}$$

The switching losses can be approximated by Equation (7.8) [38] where an average rise and fall time of the current is used. Essentially, this equation computes the switching transition energy over a transition period defined by the rise and fall time of the current for a number of switching periods defined by the PWM frequency. The losses are calculated separately for PWM controlled switches and the other three that are only switched to commutate the motor. Finally, a margin of 100% is implemented to account for circuitry connecting the MOSFETs and diodes to each other, and to the gate driver.

$$P_{swloss} = V_{supply} \times i_{rms} \times t_{rise} \times f_{PWM} \tag{7.8}$$

7.6. Sensitivity analysis

Sensitivity analysis of a model is performed to identify mistakes, know its limitations and better understand the relations between inputs and outputs. The model derived in this chapter is a powerful tool to evaluate future control strategies together with a model of the drive circuit and motor. In this chapter the model served as a tool for understanding power losses in the motor and drive circuit at steady-state situations that have been validated by test data. To draw conclusions based on the dynamic behaviour of the model and evaluate new circuit topologies the model could be extended, at the very least its limitations must be understood. Since such an effort lies outside the scope of this thesis the sensitivity analysis is not performed.

7.7. Chapter summary

Models of the motor commutation as well as the power losses inside the reaction wheel were created in this chapter. An in-depth SIMULINK simulation model of the drive circuit linked with a state-space representation of the motor equation of motion was verified using motor data sheet parameters. Power losses are separated into motor and drive circuit losses. The former includes mechanical friction, copper losses (resistive heating) and iron losses. In the latter the different switching phases of the MOSFET transistors inside the electronics were considered. Together, the models allow to evaluate control strategies and control circuit topologies, as well as characterise the power consumption of the reaction wheel. In the following chapter functional tests of the motor are used to validate the model and update empirical parameters.

8

Motor Testing & Model Validation

The selected motor is tested in this chapter to verify its performance and validate the Simulink model.

8.1. Motor testing

The main points of the testing are discussed here, and a detailed test plan and uncertainty analysis is provided in appendix D.

Test setup

A block diagram of the test setup is shown in fig. 8.1. The clamp for the motor was 3D-printed based on the preliminary design in Section 6.2. The phase voltages were measured using an oscilloscope (PicoScope). The current and speed are measured using the motor control board EPOS 24/2 with the associated software EPOS studio. The current measurement is verified using a multimeter that measures the DC current going into the control board. The speed measurement is verified by the waveform periods observed on the oscilloscope. All non-functional measurements are based on four different motors. Unfortunately, one motor was destroyed by a piece of metal blocking the rotor, so functional test results are averaged across 3 different Maxon EC10FL motors.

All variables in the functional test are described in Appendix D. The motor was tested at 25 degrees ambient temperature. The winding temperature increases with time and reaches a steady state value after 2.2 [s], however the motor temperature rises for 20.5 [s]. Two sets of measurements were performed approximately one minute apart for every functional test to account for this effect. It is important to test over time scales that include all random variations to properly account for them.

Motor test results

The results for the individual parameters and the associated measurement uncertainty are given in Table 8.1. Characteristic plots are shown in Figure 8.2. The measured no-load current is only about 1/3rd of the data sheet no-load current. However, the current measurement was checked with an external multimeter and the obtained current and voltage measurements correspond to the correct torque and speed constant and maximum efficiency of the motor. Apart from this, it was already realised in Section 7.4 that the data sheet parameters are not consistent. Furthermore, the manufacturer confirmed the measurements. It is therefore concluded that the measurements are correct within the presented uncertainty margin. The power consumption is shown in Figure 8.4.

8.2. Model validation

First the model is updated with the torque constant and friction coefficient derived from test data. Most importantly, the model now uses a 10 [V] voltage source that is chopped with the PWM frequency of 100 [kHz] to give approximately 4 [V] at the no-load speed of 16600 [RPM]. Next, by comparing the steady-state and dynamic behaviour of the model to test results the model is validated.

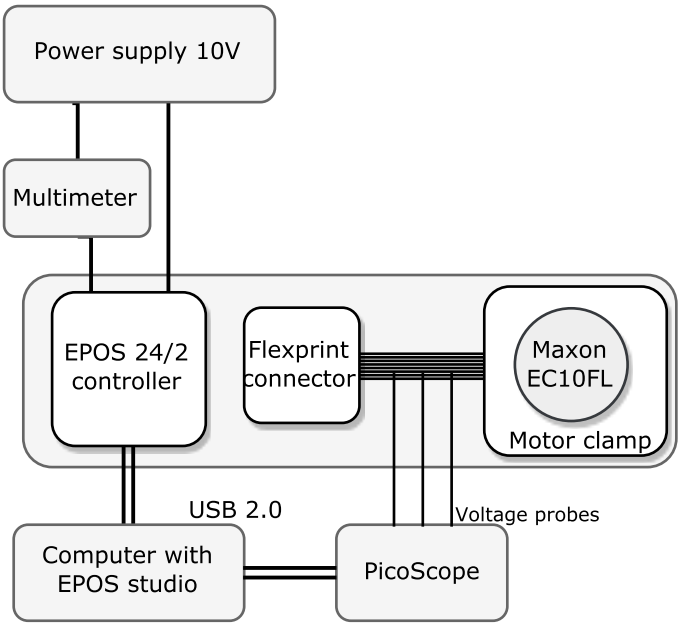

Figure 8.1: Block diagram of motor functional test

Table 8.1: Motor test results

Parameter	**Test Method**	**Data sheet value**	**Measured value**	**Uncertainty**
Weight [g]	Digital scale	0.82	1.211	0.01
Dimensions [mm]	Digital caliper	10x10x6.65	9.89x9.89x6.13	0.02
Resistance [Ohm]	Multimeter	38.8	38.8	0.001
Speed at nominal setting [RPM]	EPOS 24/2 EPOS Studio Voltage waveform	16600	16600	16.6
Speed constant [RPM/V]	Speed and voltage measurement	4870	4586	617.5
Nominal torque [mNm]	Speed curve derivation	0.25	0.216	N/A
Back EMF constant [V/kRPM]	idem	N/A	0.218	0.028
Torque constant [mNm/A]	idem	1.96	2.1	0.28
Friction coefficient [-]	Current measurement	N/A	0.77	0.21
Nominal no-load current [mA]	EPOS 24/2 EPOS Studio Multimeter	14.8	5.157	1.1
Nominal voltage [V]	Oscilloscope	4	3.82	0.21
PWM frequency [kHz]	Oscilloscope	100	100	N/A

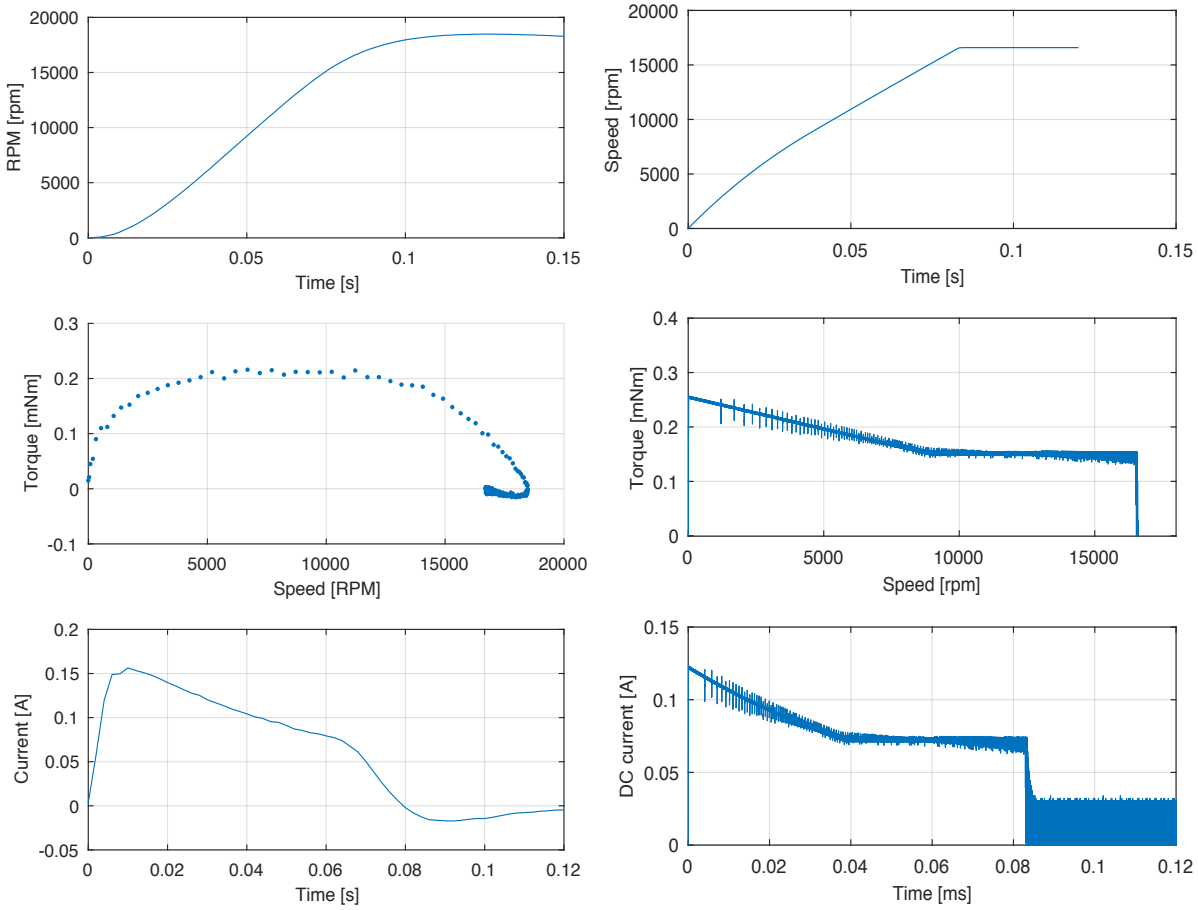

(a) Motor test results

(b) Model simulation results

Figure 8.2: Performance comparison test data and simulation results

To evaluate the steady-state at the no-load speed of 16600 [RPM] the voltage waveforms and no-load current are compared. The waveforms are shown in Figure 8.3. Clearly their period, amplitude and general shape match very well. To explain the differences further analysis is required, but measurement noise is an important factor, which contributes to the presence of non-zero voltages between peaks. Apart from this, the no-load current in the model of 5.8 [mA] falls inside the uncertainty band of the measured value of 5.2 [mA].

The dynamic behaviour is contrasted against test data in Figure 8.2. The time required to accelerate to the no-load speed is 0.82 [s] in both speed vs time curves. However, the test data shows an overshoot and it takes up to 0.2 [s] to reach a steady state speed, whereas this is practically instant in the model. This is also reflected in the torque and current curves. The test result torque curve is obtained by scaling the derivative of the speed curve with the rotor inertia. As a result the torque at low speeds is not accurate. Furthermore, the PWM effects are not visible in the test results because the controller takes the average values of the speed and the DC current. Nonetheless, the peak values and time periods in the plots match reasonably well. However, it must be concluded that the dynamic behaviour is only modelled well as a first approximation. This can be improved once the actual drive electronics are developed for which the model can serve as a design tool.

8.3. Detailed power consumption

The breakdown of the motor power consumption is shown in Figure 8.4. The identification of the diode and MOSFET current is shown in the annotated transistor current waveforms in Figure 8.5 and Figure 8.6. The power consumption is later compared to that of the complete reaction wheel in Chapter 12. The friction loss is by far the largest source of inefficiency. In fact, greater friction requires a larger current to be overcome, which

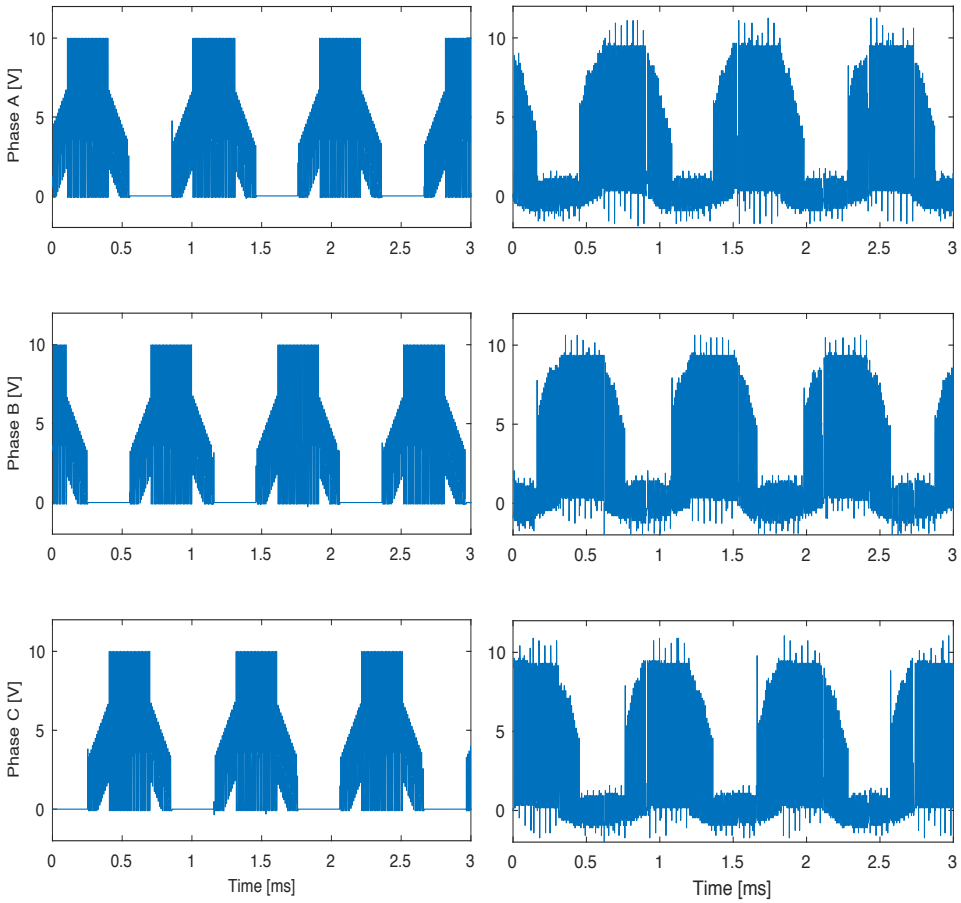

(a) Model voltage waveform (b) Measured voltage waveform

Figure 8.3: Comparison between measured and simulated voltage waveform

also increases copper losses. The drive circuit losses amount to about 15% of the motor losses, where the most energy is lost in the OFF phase of the motor.

8.4. Chapter summary

Functional testing of the motor led to the conclusion that the power consumption of the motor is one third of the data sheet value. Results were checked with an external current measurement, and deliberation with the manufacturer confirmed the test results. Restrictions in the controller and measurement methods constrained the measurement accuracy. A breakdown of the motor power consumption was successfully established in combination with the Simulink model. The model was validated for steady-state conditions, but once the exact motor topology is known this can be extended to dynamic scenarios as well. At present this was not necessary to characterise the power consumption.

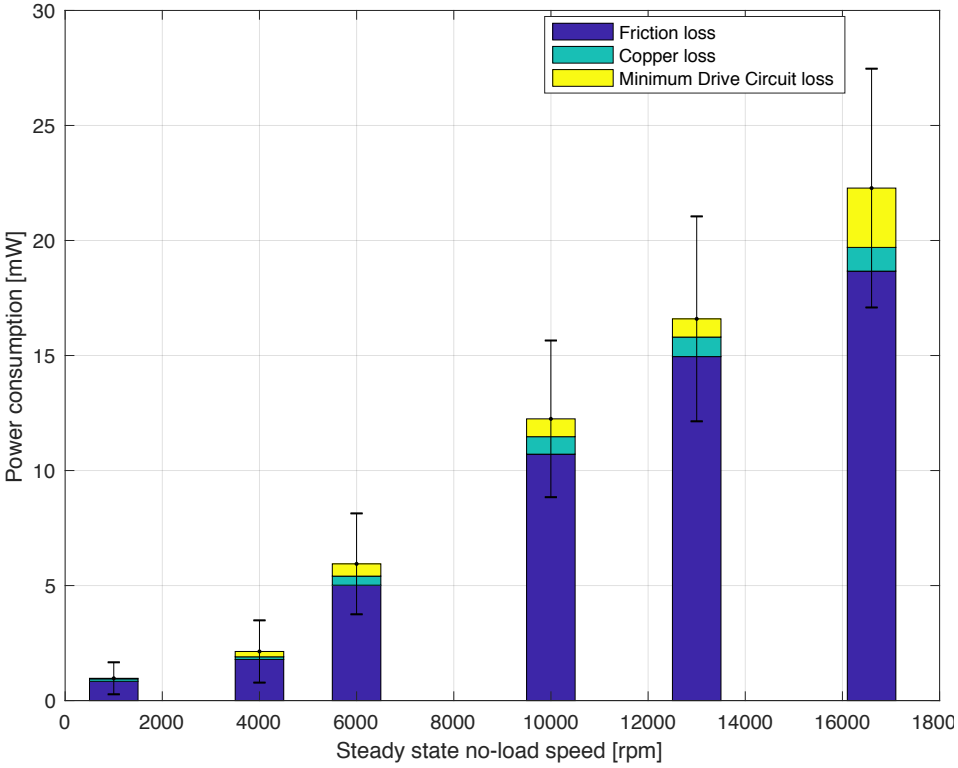

Figure 8.4: Breakdown of motor power consumption

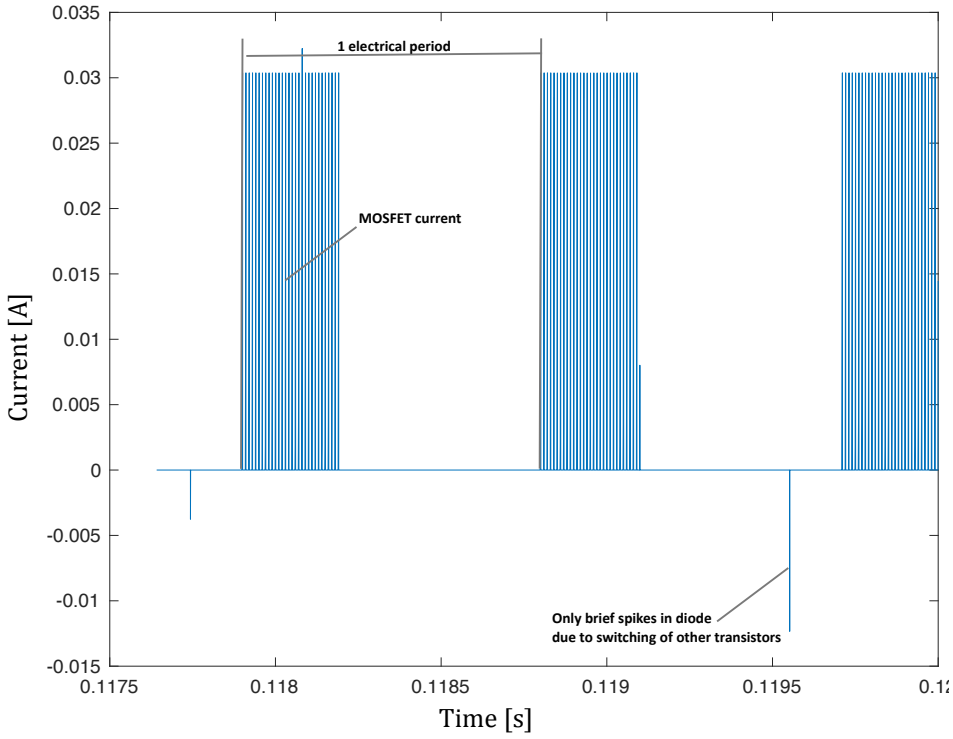

Figure 8.5: Current in Chopping transistor 1

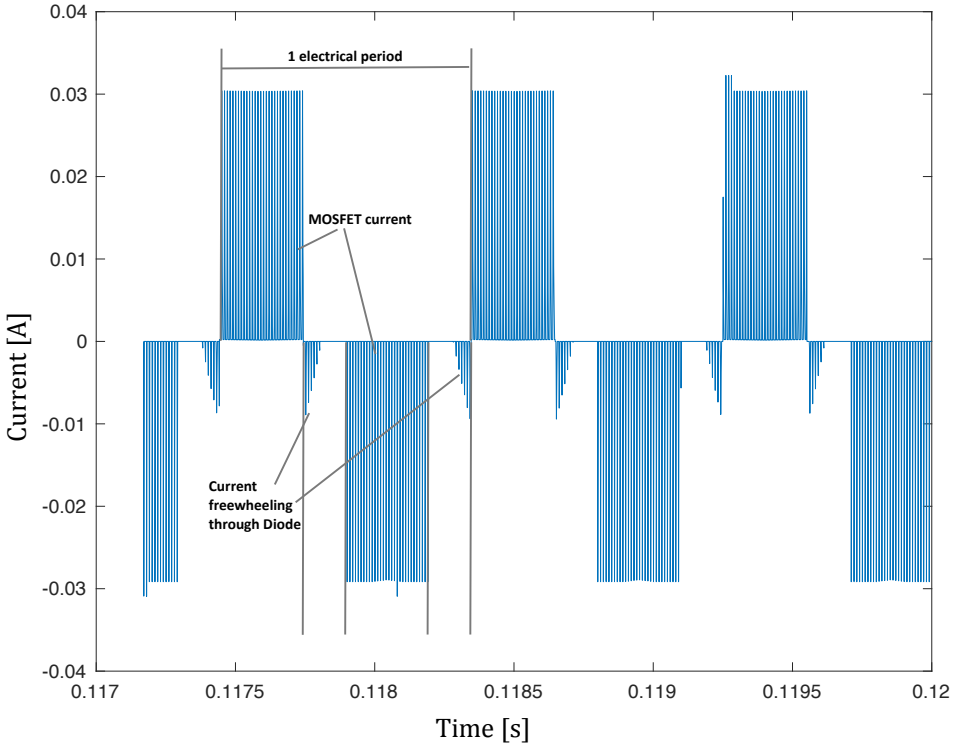

Figure 8.6: Current in bottom transistor 4

9

Detailed Hardware Design

In this chapter the detailed design of the reaction wheel assembly is presented. Starting with the requirements in Section 9.1 a housing for the motor and flywheel is designed in section 9.2. The integration approach is described in Section 9.3. Manufacturing results are discussed in Section 9.4. Requirements for the control electronics are presented in Section 9.5, although their development lies outside the scope of this thesis. Finally, a proposed design for a three-wheel assembly is presented in Section 9.6.

9.1. Housing requirements

Using the results of the preliminary design the requirements for a detailed design were derived from RW level requirements. The housing must provide a pressurised environment to prevent evaporation of the bearing lubricant and should have an eigenfrequency of above 200 [Hz] to guarantee the complete RW has an eigenfrequency above 60 [Hz]. It will be 3d printed out of aluminium for easy and cheap manufacturability, which allows considerable freedom of design.

COM-HO1. The housing shall provide structural support for the motor and flywheel, and interface with the three-wheel assembly structurally.
COM-HO2. The housing shall have an airtight seal and 1 atmosphere internal pressure.
COM-HO3. The housing shall survive random vibrations of 7.2 [g] (RMS) during launch [8].
COM-HO4. The housing shall survive sine vibrations of 3 [g] max. during launch [8].
COM-HO5. The housing shall ideally have a mass of less than 3 [g], but for a first design it shall weigh less than 5 [g].
COM-HO6. The housing shall be made out of aluminium.
COM-HO7. The housing shall have an eigenfrequency of more than 200 [Hz].

9.2. Housing design

The reaction wheel assembly consists of the motor, a flywheel and a sealed housing. Two different housing designs are considered.

Structural design

The housing consists of a bottom part where the motor with flywheel is mounted and a top part that seals off the motor. In design A there is an O-ring at the interface of the two halves and the top half is both glued and bolted to the bottom half. Design B is without an O-ring and room for bolts and is only glued. This results in a smaller and lighter design, but it is unclear whether it can provide a secure seal. Design A and B are shown in Section 9.2. The motor can be glued to the middle of the bottom structure, or clamped inside it. The flat motor cable is fed through the back of the slot at the back of the clamp underneath the motor towards the front of the housing. The top half is glued to the bottom half (see section 9.3).

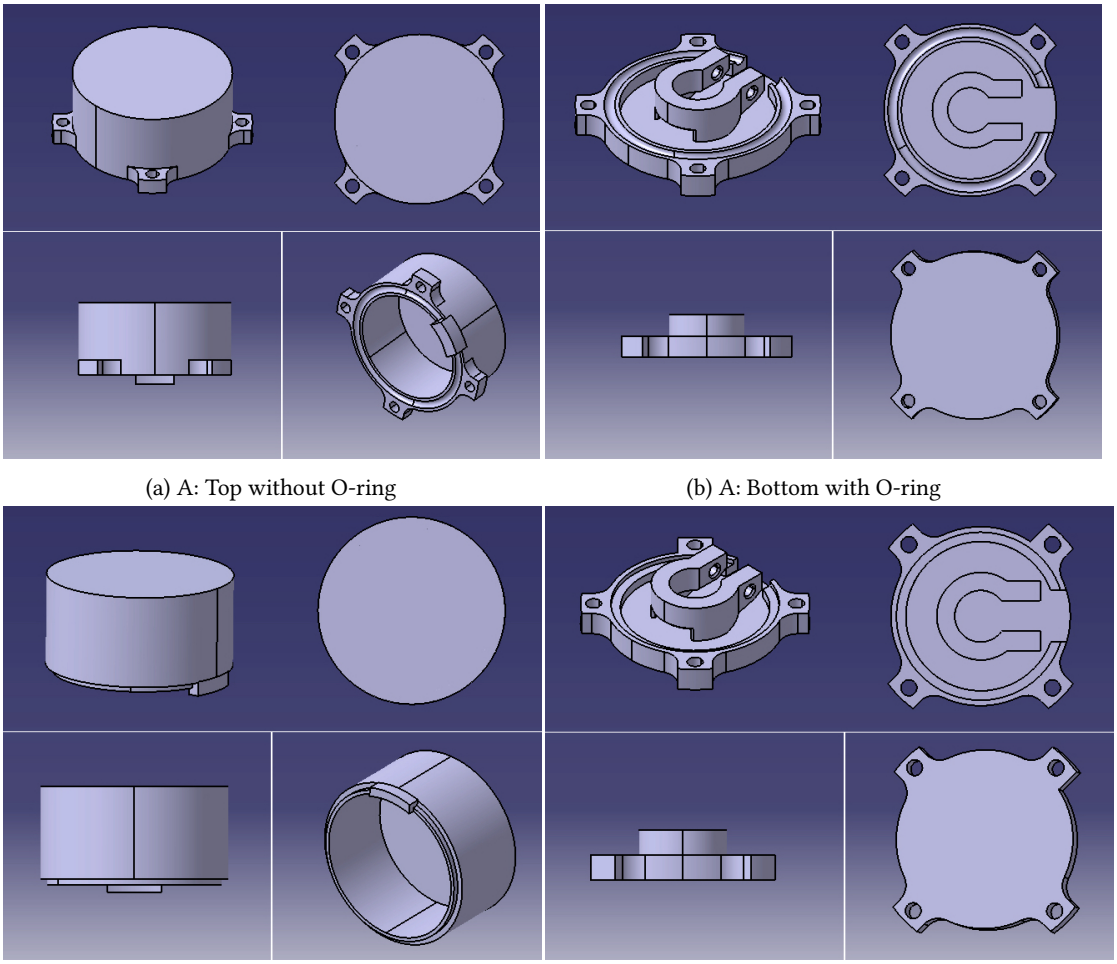

(a) A: Top without O-ring

(b) A: Bottom with O-ring

(c) B: Top without O-ring

(d) B: Bottom without O-ring

Figure 9.1: Reaction wheel housing designs

Structural analysis

The housings are analysed for their compliance with structural requirements. They must survive stresses due to the internal gas pressure and the launch vibrations. Apart from that their eigenfrequency must be below 60 [Hz].

Stress analysis

The stress due to the air pressure inside the housing is well below yield stress for 3D printed Aluminium [21].

$$\sigma = \frac{P \times r}{2 \times t} = \frac{1 \times 10^5 \times 0.008}{2 \times 0.001} = 0.4 \times 10^6 << \sigma_{yield} = 227 \times 10^6 \tag{9.1}$$

Using CATIA's generative structural analysis workbench the launch vibrations and eigenfrequencies are simulated.

Section 9.2 shows the stresses and displacements resulting from simulated launch vibrations for Design B. As it has a lower wall thickness than Design A it will experience larger stresses. The boundary conditions are clamping inside the screw holes and an acceleration of 7.2 [g] is applied on the entire bottom surface for the bottom part, and on the connecting surfaces for the top part. Defining a factor of safety (FOS) as in Equation (9.2), where σ_{VM} is the Von Mises stress a FOS of around 1800 [-] is computed for the maximum stress. It can be concluded that both parts of the housing comply with requirement COM-H3. However, the internal

connections are not straightforward to simulate, and are likely to be the critical points in the design due to stress concentrations on any imperfections. They are tested as part of vibration testing in Section 11.5.

$$F_{safety} = \frac{\sigma_{yield}}{\sigma_{VM}} \tag{9.2}$$

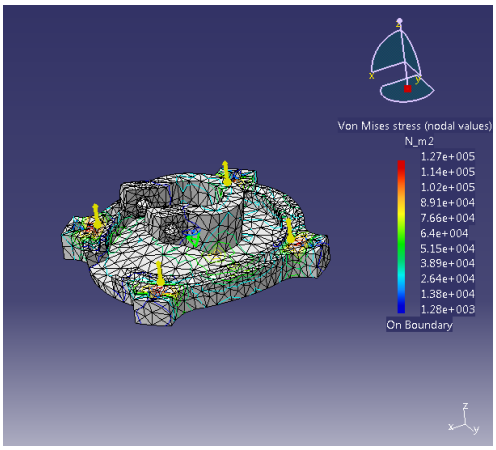

(a) A: Bottom Von Mises stress

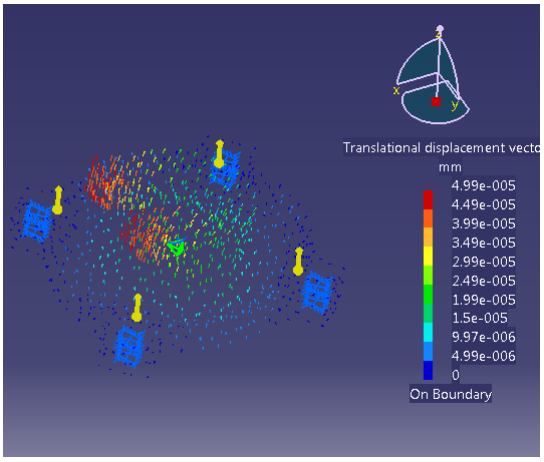

(b) A: Bottom displacements

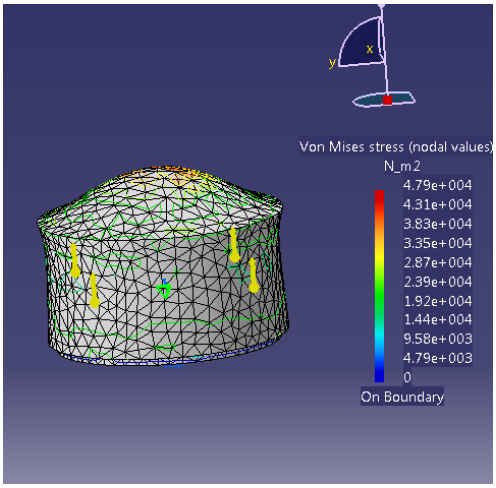

(c) A: Top Von Mises stress

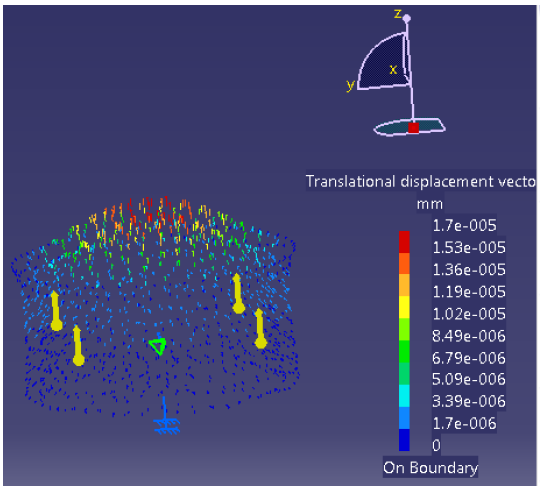

(d) A: Top displacements

Figure 9.2: Reaction wheel housing launch stresses

Eigenfrequency

For the eigenfrequency simulations a mass dummy of the reaction wheel was used, in which all connections between the components are completely rigid. The housing is clamped at the screw holes resulting in a first mode at 6.8 [kHz] for housing A. The effect of using a the simplified model can be evaluated by considering the equation for a simple mass-spring system eq. (9.3) [21]. The actual stiffness of the wheel is lower because of internal structural connections so the eigenfrequency is lower in reality. Housing A was considered as it has a higher mass than Housing B, and so has a lower eigenfrequency. Since the computed value is far above requirement RW-PH5 this simplification is reasonable for a first approximation. The eigenmodes are determined experimentally in Section 11.5.

$$f = 2\pi \times \sqrt{\frac{stiffness}{mass}} \tag{9.3}$$

Table 9.1: Specifications Reaction Wheel Assembly

Reaction wheel assembly	Design A	Design B
Mass housing [g]	5.35	3.356
Mass RWA [g]	9.38	7.33
Dimensions [mm]	20x20x12	18x18x11.5
Minimum torque [mNm]	2.93×10^{-4}	2.93×10^{-4}
One way momentum storage [Nms]	0.113	0.113

9.3. Integration approach

The flywheel is glued on the rotor of the motor, and the motor is glued to the bottom structure. Then, for Design A the O-ring is glued to the bottom structure as well. The top half of the structure is glued to the bottom half sealing the motor and flywheel inside.

Glue selection

For the flight model a space-grade glue is required, but for an engineering model a non-space qualified glue is used. A suitable glue was found in deliberation with manufacturers by communicating the structural and environmental requirements of the housing. An epoxy type two component glue Loctite 3430 provides the required bonding strength and does not evaporate in vacuum.

O-ring selection

An O-ring can provide a vacuum seal when it is compressed inside the structural interface if it is properly placed and clamped. Because the motor cable must go out of the housing a complete O-ring seal is impossible. Nonetheless, the use of an O-ring to seal the rest of the structure is considered. While not strictly in contact with the space environment (as the O-ring is enclosed by the aluminium structure), the O-ring shall have low outgassing in vacuum, low permeability for Oxygen and Nitrogen molecules and a low coefficient of thermal expansion. Suitable materials include Fluoroelastomers and Propylene [41]. Furthermore, the O-ring must be available with the required radius of 8.5 [mm] and thickness of 1 [mm]. The selected O-ring is made of EPDM, a type of Ethylene Propylene rubber.

9.4. Manufacturing

The designs are first 3D-printed with plastic to test their fit and then using Aluminium. 3D printing was chosen as manufacturing method because it allowed for the integration of the clamp with the bottom structure and is a factor of ten cheaper than conventional milling and drilling at small scales. A drawback is that print accuracy is no better than 0.1 [mm] which is significant as the minimum internal thicknesses is 0.5 [mm]. This was evident in the fabricated parts as some filing was required to achieve a good fit. Furthermore, the printed parts show material imperfections, which can lead to stress concentrations. The parts and assembled wheel can be seen in Section 9.4. The specifications of the reaction wheel assembly are given in Table 9.1.

9.5. Control electronics

The control electronics board is not developed as part of this thesis, but its requirements are a result of the work.

COM-C1. The control electronics board should control the motor using Pulse-width modulation.
COM-C2. The control electronics board shall have a power consumption of less than 10 [mW].
COM-C3. The control electronics shall be able to control the motor speed to at least within 300 [RPM].
COM-C4. The board shall have dimensions of less than 14x14x2 [mm].
COM-C5. The board shall have a mass of less than 1 [g].

Pulse-width modulation is suggested as control approach because it is widely used, efficient and is simple to implement [24]. The other requirements follow directly from the system requirements.

(a) All RWA parts

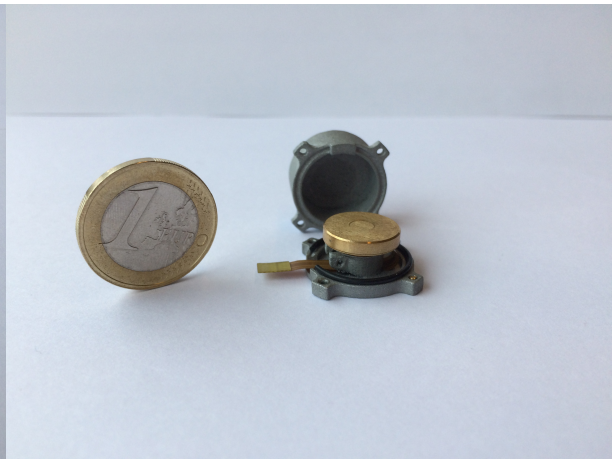

(b) Design A open view

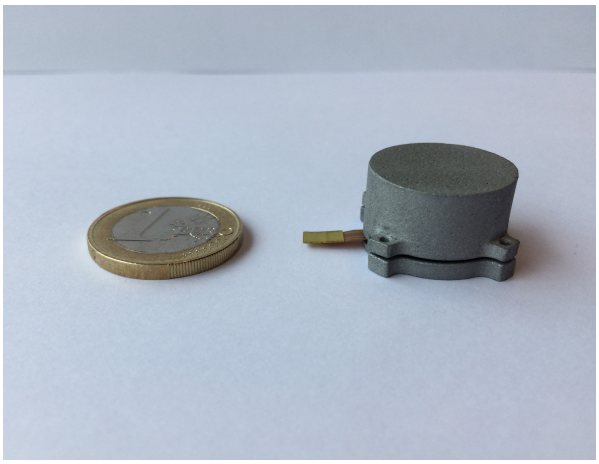

(c) Design A front view

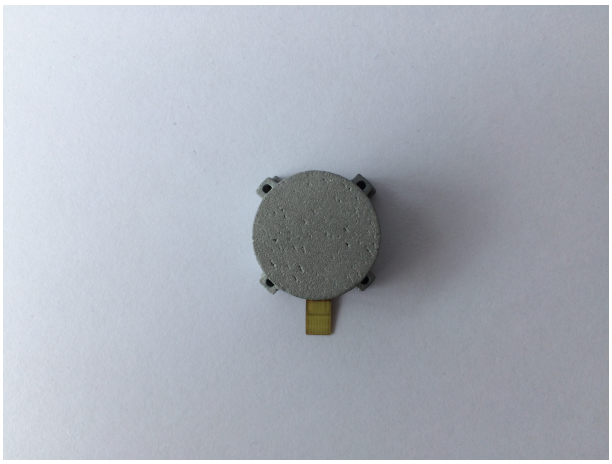

(d) Design A top view

Figure 9.3: Reaction wheel housing designs

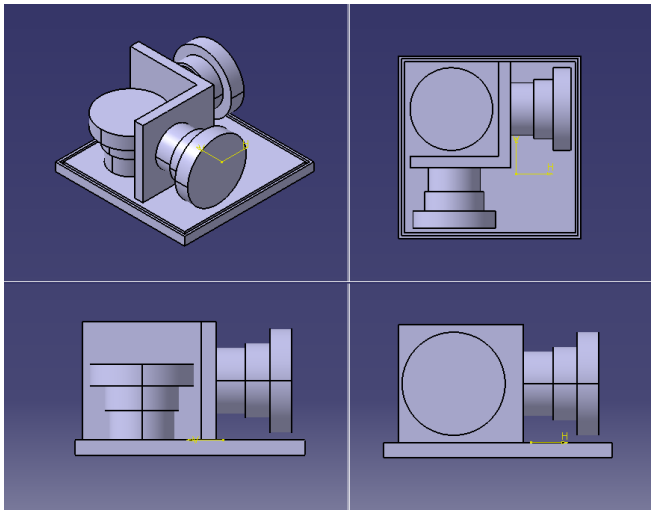

Figure 9.4: Bottom half of three-wheel assembly

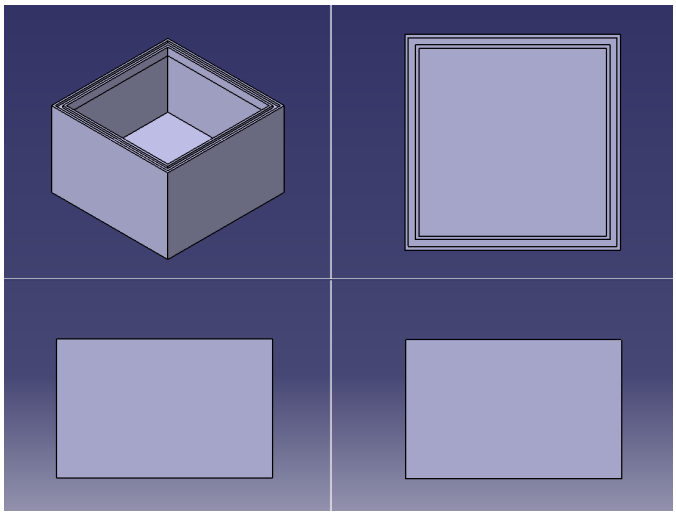

Figure 9.5: Top half of three-wheel assembly

9.6. Three-wheel assembly

A preliminary design for the three-wheel assembly is given in Figure 9.4 and Figure 9.5. The flywheel is attached to the motor as in the one wheel design, but all three wheels are within the same pressurised housing. The exact interface between the motor and the structure is not defined, but overall the structure is simple. It can be manufactured without 3D-printing, as this provided very mixed quality results. The dimensions are 31x31x22 [mm]. The control electronics should be integrated into the top of the structure. There is in the design 3 [mm] thickness included for this. In this way all the motor cables stay inside the housing, and the connections between the control electronics and the ADCS processor should be integrated at the top as well.

9.7. Chapter summary

Based on component level requirements two options for a housing were designed. The motor can be glued, or clamped, inside the bottom half and the flywheel is glued to the motor rotor. Design A includes an O-ring to seal the housing while Design B relies solely on glue to properly seal the two halves of the structure. Structural analysis indicates compliance with requirements with room for further optimisation. The interface of the RW assembly with the ADCS for now simply consists of 4 M1.6 screw holes. The use of 3D printing to manufacture the RW structure will be evaluated. A proposed three-wheel design takes the miniaturisation a step further including 3 wheels as well as their control electronics inside one pressurised housing. In the next part of this

report the one wheel assembly will be tested extensively to provide conclusions for a future detailed design of the three-wheel assembly.

IV

Testing

10

Micro-vibration Test Bench

In this chapter the development of a micro-vibration test bench is described. Its purpose is to measure the vibrations generated by the reaction wheel. Possible disturbance models are discussed in Section 10.1 to determine which parameter should be measured, followed by an estimation of the required measurement sensitivity in Section 10.2. Section 10.3 describes the selection of an appropriate test method. Technical requirements for the test bench and accelerometer are presented in section 10.4. The selection of a suitable sensor, its working principle and a comparison between theoretical and actual performance are presented in Section 10.5. The test bench is designed in section 10.6 and its integration and calibration is discussed in section 10.7.

10.1. Reaction wheel disturbances

Sources of disturbances and state of the art models are considered to support the selection of a suitable test method.

Reaction wheel disturbances caused by rotation of the wheel have have fundamental and harmonic components. Their analysis is complicated by structural vibration modes of the reaction wheel structure (and satellite). Fundamental disturbances are caused by static and dynamic imbalances of the wheel. They include mass imbalance and misalignment of the flywheel, and bending of the motor axle during rotation due to its finite stiffness. This results in a force and moment proportional to wheel speed [51]. Disturbances that occur at sub and higher harmonics of the wheel speed are referred to as harmonic disturbances. They include dynamic lubrication behaviour, control errors like cogging and torque ripple and irregularities in the bearing balls, races and cages [29]. Harmonic disturbances can be further amplified at structural vibration modes of the wheel. It is therefore important to test at frequencies larger than the wheel speed to properly consider these potentially most important disturbances.

State of the art disturbance models combine analytical and empirical models and use test data to determine reaction wheel specific parameters experimentally [29]. In principle, measurements of forces and moments in three axes are sufficient to extract the relevant parameters [29]. It is also possible to measure accelerations to derive these forces and moments [15]. A suitable measurement approach is selected in section 10.3. The measurements can be used in future work as input for a disturbance model.

10.2. Measurement sensitivity

The required measurement sensitivity is approximated by considering vibration levels measured on the ExoplanetSat reaction wheel system.

ExoplanetSat is a satellite mission aiming to detect exoplanets around sun-like stars on a nanosatellite platform. This requires arc second level pointing stability [43]. Vibrations due to the rotation of reaction wheels are an important constraining factor in achieving high pointing accuracies. At the Massachusetts Institute of Technology Space Systems Laboratory (SSL) and the Goddard Space Flight Center (GSFC) vibration tests of the Maryland Aerospace Inc.'s MAI- 200 reaction wheels have been performed [43] to assess the feasibility of the pointing requirement. MAI-200 consists of three orthogonally placed reaction wheels fixed in a housing

Table 10.1: Estimated disturbance forces MAI-200 reaction wheel [43]

	Minimum		Maximum	
	Axial	Radial	Axial	Radial
Max force coefficient [mg × mm]	230	170	2400	1600
Max torque coefficient [mg × mm^2]	4700	31000	260000	310000
Wheel speed [rad/s]	104.72	104.72	418.88	418.88
Max force [mN]	2.52	1.86	421.1	280.7
Max torque [mNm]	0.052	0.34	45.62	54.4

with a total mass of 910 [g] and dimensions of 100x100x79 [mm] [1]. Reaction wheel specific coefficients describing dynamic behaviour at harmonic resonances are extracted from vibration data and used to compute forces and torques, in both axial and radial direction. An estimate of the expected maximum disturbance forces of the Delfi-PQ reaction wheel is derived by scaling forces and torques obtained using equation one and two [43][p.8]. Results are shown in section 10.2. A single MAI-200 reaction wheel weighs about 300 [g], roughly 2 orders of magnitude heavier as the Delfi-PQ reaction wheel. Therefore, at harmonic resonance peaks forces and moments between respectively 0.0186 [mN] and 4.211 [mN] and between 0.00052 [mNm] and 0.544 [mNm] can be expected.

10.3. Test approach

Different vibration sensors and methods used for reaction wheel testing in literature are discussed and the distinction between hard-mounted and coupled measurements is made clear. An approach taking hard-mounted measurements using piezoelectric bimorph sensors is chosen for the micro-vibration test bench.

Acceleration can be measured directly, or it can be computed from measurements of force, velocity or displacement. Vibrations are typically derived from measurements using dynamometric platforms (measuring force or torque using load cells) [40] [43] [17]. These force tables can measure forces down to 1 [mN] [51]. Another approach measures displacement using charge-coupled-device laser sensors [48] which enables measurements with a sensitivity of about 0.5 [mN] up to a maximum frequency of 20 [Hz]. A simpler approach is based on sensing accelerations transmitted to a seismic mass using accelerometers achieving similar sensitivity levels [51]. Unfortunately, accelerometers with sufficiently high sensitivity are not readily and cheaply available. Accelerometers make use of the piezoelectric effect to link charge generated from compression of a piezoelectric component to the acceleration of an internal mass. The same effect can be exploited using piezoelectric bimorph sensors that can achieve very high measurement sensitivities (see Section 10.5).

Apart from the physical quantity and how it is measured, it is important to define what the measurement represents. On a satellite the vibrations of the wheel are transmitted to the satellite's structure in a zero-g environment. The structure in turn vibrates and transmits vibrations back to the wheel. The dynamic behaviour of the wheel is said to be coupled with the behaviour of the structure it is attached to. Only a coupled measurement is truly representative of the operational environment. On Earth, zero-g environments are simulated using methods such as suspending the measurement platform using air-bearings, string suspension, or gimbals and operating the platform in zero-g during parabolic flights [12]. Furthermore, the wheel must be attached to a representative satellite structure to achieve a coupled measurement. Moreover, the sensor itself cannot introduce too much mass to the system or the measurement is not representative of the operational conditions. For example, force tables are not suitable for coupled measurements as they are several orders of magnitude heavier than the reaction wheels themselves. However, hard-mounted measurements can be used to estimate coupled dynamics [7]. In the scope of this thesis only the hard-mounted measurements will be analysed, but the estimation of coupled dynamics is recommended for further analysis. Nonetheless, the measurement approach shall make use of a free-free suspension method to isolate the vibrating mass. This allows deriving the forces and moments at the reaction wheel to seismic mass interface from acceleration measurements [53].

10.4. Test bench requirements

Technical requirements for the test bench are:

TB-HW1 Natural vibration modes of the measurement system shall be larger than 1.5 [kHz] or as close to 0 [kHz]

as possible.

TB-HW2 The test bench shall be made out of high stiffness material (e.g. Aluminium 7075).

TB-HW3 The test bench shall be suitable for different RWAs with a maximum diameter of 5 [cm].

TB-HW4 The vibration sensors shall be rigidly attached to the measurement system, and data cables shall not introduce unwanted load paths.

TB-HW5 The test bench shall have a cost of less than 1500 Euro.

TB-HW6 The test bench shall be operated on a suitably solid table to isolate it from parasitic vibrations.

TB-HW7 The test bench shall consist of a seismic mass that is suspended by two ropes.

The technical requirements for the vibration sensor are as follows.

TB-ACC1 The sensor shall have a measurement sensitivity of at least 10 V/g and ideally 100 V/g.

TB-ACC2 The sensor shall operate at frequencies between 0 and 1.5kHz.

TB-ACC3 The sensor shall be insensitive to external varying magnetic fields created during motor operation.

The maximum useful motor speed corresponds to a forcing frequency of about 220 [Hz]. As discussed in Section 10.1 at higher harmonic frequencies the largest disturbances occur so the measurement range is ideally between 0 and 1.5 [kHz]. However, as is explained in Section 10.5 both the selected sensor and calibration sensor have reduced performance at frequencies above 1 [kHz]. Because of the high measurement sensitivity, parasitic vibrations will likely constrain the lowest measurable accelerations. Both the suspended seismic mass and a very solid base table will filter out background noise.

10.5. Piezoelectric bimorph sensor

In this section the principle of piezoelectricity and bimorph sensors is described and theoretical and measured sensitivities during calibration testing are compared. Finally, an additional high sensitivity accelerometer for calibration of the test bench is selected.

Piezoelectric effect and bimorph sensors

When stress is applied to a piezoelectric material a proportional charge is generated. To exhibit piezoelectric behaviour the material's molecules must lack a centre of symmetry and be non-conducting. On a molecular level, the centres of positive and negative charge within one molecule move with respect to each other resulting in an electric dipole. The opposite of this direct piezoelectric effect is also possible. The indirect effect is when an electric field is applied across a piezoelectric material it deflects geometrically due to an induced electric force moving the ions with respect to each other [23].

In addition to this, some piezoelectric materials show pyroelectric behaviour where a change in temperature of the material generates a charge. On a molecular level it is a change in the position of the atoms with respect to each other that changes the polarisation state of the molecule [23].

A bimorph, also called bender, is made by bonding two thin polarised piezoelectric plates on a metallic supporting layer. If the layers are oppositely polarised the pyroelectric effect is cancelled out. This means temperature does not need to be closely controlled in an experiment. When the sensor is bent one layer is compressed while the other is elongated. The opposite stress and opposite polarisation lead to the same voltage over the sensor layers, hence both layers can be connected in series. This polarisation configuration is called a series bimorph [23]. This sensor will be used in the micro-vibration test bench.

Theoretical measurement sensitivity

The theoretical measurement sensitivity can be computed from piezoelectric sensor theory. Parameters of interest are the sensor's voltage sensitivity and resonance frequency, which can be calculated using Equation (10.1) and Equation (10.2), where L is the free (unclamped) length of the sensor, L_t is its total length and h and w are its thickness and width, respectively.

$$S_{U,bender} = 2 \times 10^{-2} \times \frac{L^2}{h \times L_t \times w} \tag{10.1}$$

$$f_{res} = 400 \frac{h}{L^2} \tag{10.2}$$

Table 10.2: Voltage sensitivity and resonance frequency (h=0.75 [mm], w = 5.87 [mm])

Sensor free length L_t [mm]	Voltage sensitivity S_U [V/g]	Resonance frequency f_res [Hz]
17.8	6.4	943.7
26.8	10.4	418.3
40.9	16.8	179.3

Table 10.2 shows voltage sensitivities and resonance frequencies for different sensor lengths. In addition, it is possible to pre-load the sensors by placing a mass at the free end of the sensors, which greatly improves its sensitivity. However, it is not straightforward to calculate this effect so instead it is determined experimentally.

Sensor calibration

The test setup used to calibrate the sensors is shown in Section 10.5. The output of the bimorphs is compared to that of a calibrated accelerometer with a sensitivity of 8.04 [mV/g]. The Bruel & Kjaer accelerometer has a constant sensitivity up to 12 [khz]. Sine vibrations of varying frequency are applied to measure the voltage sensitivity at different frequencies and to find the resonance frequency of the different bimorphs. The bimorphs are read using a charge-to-voltage converter and amplifier with variable gain, which eliminates cable influences [23]. Electrical noise and parasitic vibrations will determine the lowest measurable vibrations. The wires soldered to the bimorph are connected to a shielded Coax cable which is connected to the amplifier. Shielding drastically reduces the electrical noise. The amplifier also filters out signals above 1 [kHz], which further reduces the noise. Furthermore, some of the noise can be averaged out in the oscilloscope.

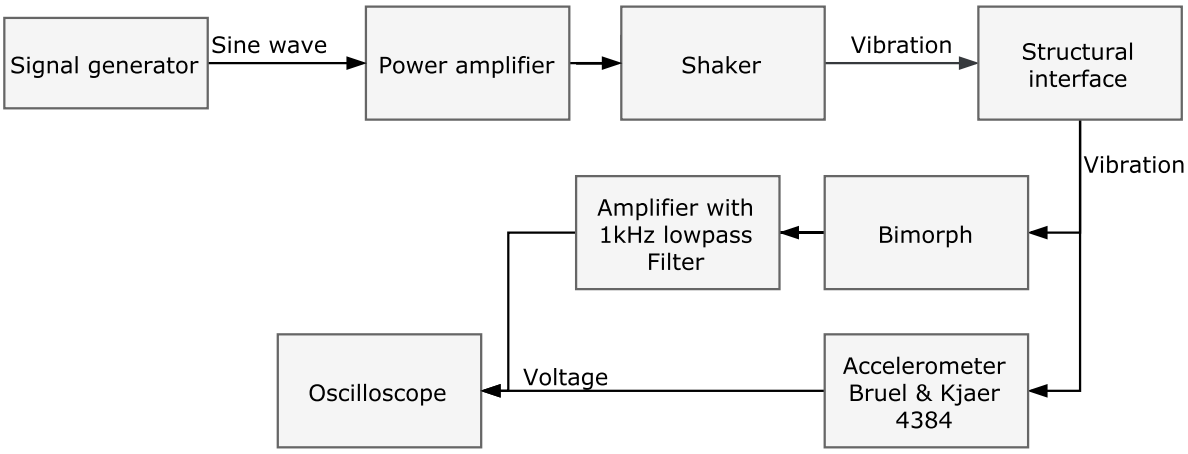

Figure 10.1: Calibration test setup

Experimental measurement sensitivity

The measured sensitivities at different frequencies are shown in Section 10.5.

First of all, the measured sensitivities are well below the theoretical values. In a charge to voltage converter the output voltage scales with the converter capacitance [23]. The amplifier has a variable gain, so that the theoretical value is not necessarily representative. On the other hand, the importance of properly clamping the sensors was also realised. The effective length of the sensor can change and additional energy is dissipated if the sensor moves inside the clamp. This is an important consideration for the test bench.

The sensitivity increases drastically by pre-loading the sensor, but at the cost of an equally sharp decrease in the resonance frequency. The behaviour of the sensors is also frequency dependent already well below resonance. This effect is exacerbated by the added mass, because it decreases the range. In addition, below a certain forcing frequency the sensor also resonates at its resonance frequency. This is strongly dependent on the input signal, however.

Measurement noise corresponds to an acceleration of between 0.0001 - 0.002 [g] depending on the sensor. However, it is unclear to what extent the noise consists of parasitic vibrations, which will be filtered by the suspension of the test mass. Purely electrical noise might be averaged out using long acquisition times.

The sensitivities that can be achieved, albeit in restricted frequency ranges, are sufficient to measure the expected disturbances. However, calibration tests are performed at vibration levels several orders of magnitude above the expected reaction wheel disturbances. This analysis therefore only serves as a rough indication of the frequency range and voltage sensitivity of a particular sensor and added mass.

In conclusion, initial results indicate that for limited frequency ranges the required sensitivity can be achieved. Shorter sensors are required to measure at higher frequencies, but they likely will not have sufficient sensitivity. Further tests using a highly sensitive reference accelerometer on the actual test bench are required. Three main points need to be resolved.

1. What is the background noise of the test setup?
2. Can the sensors provide reliable measurements at frequencies above their resonance frequency?
3. What is the actual signal to be measured?

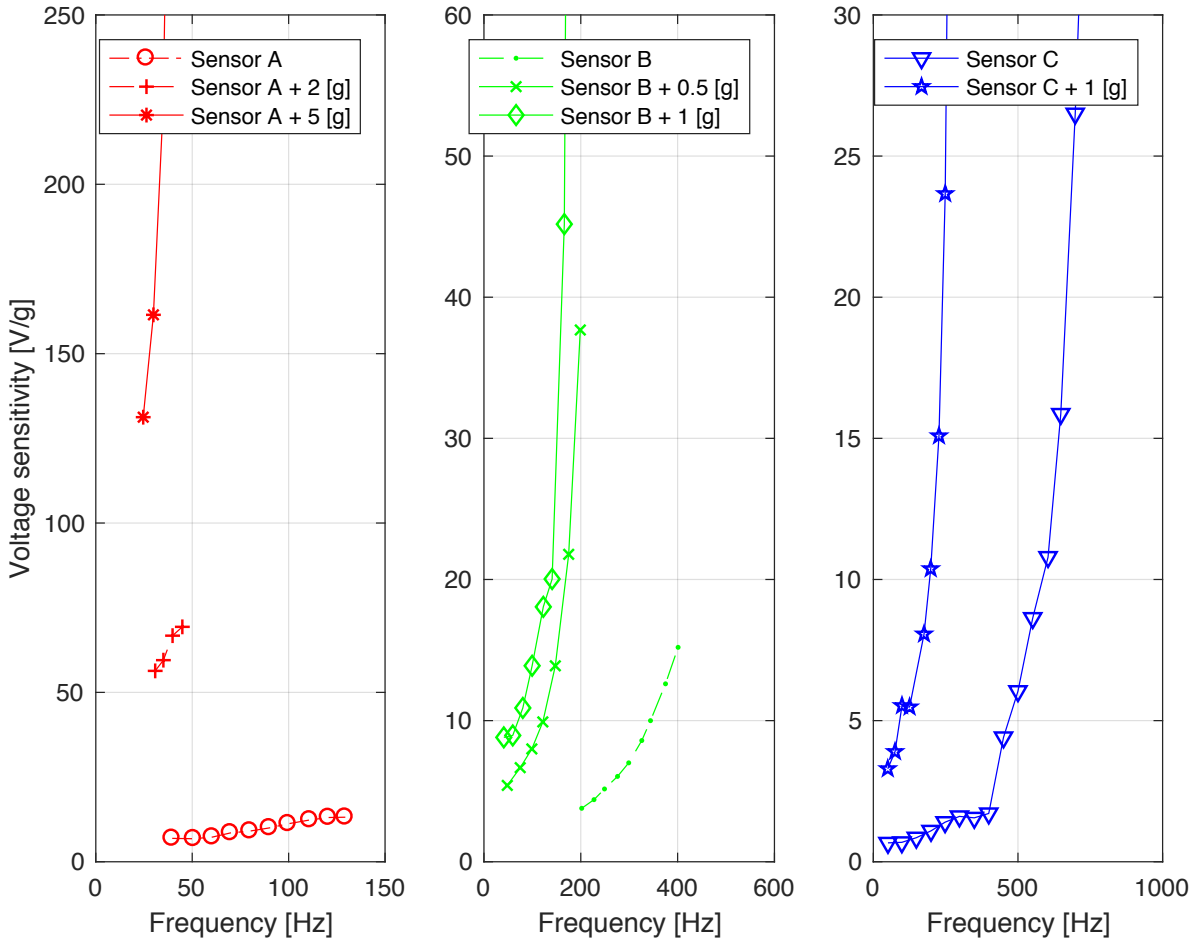

Figure 10.2: Calibration test results

High Sensitivity Calibration sensor

The high sensitivity accelerometer has the same technical requirements as identified for the bimorph sensors, with the added consideration that the sensor should not be too large to be mounted on the test bench. Unfortunately, in the sensitivity range above 1 [V/g] there is very limited choice. The PCB 393B12 accelerometer offers the largest frequency range of up to 1 [kHz], with a mass of 210 [g] and a sensitivity of 10 [V/g].

10.6. Structural design

The test bench consists of a suspended seismic mass on top of which the reaction wheel assembly is placed. The piezoelectric bimorphs are used to measure accelerations in two directions. From this, disturbance forces and moments can be derived, which in turn can be used in future work to validate a mathematical model of the reaction wheel assembly.

Disturbances from acceleration measurements

The test bench is based on the work presented by Zhou et al. [53]. A schematic of the bench is shown in Figure 10.3. Measurements of accelerations at location 1-4 are used to derive the forces and moments at the interface of the wheel and the seismic mass. Accelerometer 1 and 2 measure in the y-axis, and three and four measure the acceleration in the z direction. This measurement can be linked to forces and moments at the measurement location.

$$\vec{\mathbf{a}} = \frac{\mathbf{d}\vec{v}}{\mathbf{dt}} + \frac{\mathbf{d}\vec{\omega}}{\mathbf{dt}} \times \vec{r_b} + \vec{\omega} \times (\vec{\omega} \times \vec{r_b}) \tag{10.3}$$

The radius vector from the centre of mass of the seismic block to the location of the accelerometers is represented by $\vec{r_b}$. The velocity and angular velocity vector of the seismic mass are given by $\vec{v}$ and $\vec{\omega}$, respectively. During testing $\vec{\omega}$ is small and the centripetal acceleration term $\vec{\omega} \times (\vec{\omega} \times \vec{r_b})$ is assumed to be negligible. The remaining terms can be formulated in terms of the forces and moments.

$$\vec{\mathbf{a}} = \frac{\mathbf{d}\vec{v}}{\mathbf{dt}} + \frac{\mathbf{d}\vec{\omega}}{dt} \times \vec{r_b} = \frac{F_m}{m} + \frac{\vec{\tau_m}}{I} \times \vec{r_b} \tag{10.4}$$

The equation is filled in for the locations 1 and 2, and then rewritten in terms of acceleration measurements. Note that the sign convention defined in the paper (Figure 10.3), shows that d_2 is positive while d_1 is negative. Nonetheless, the derivation is continued with this new sign convention.

$$\begin{bmatrix} a_1 \\ a_2 \end{bmatrix} = \begin{bmatrix} \frac{1}{m} & \frac{d_1}{I_{xx}} \\ \frac{1}{m} & -\frac{d_2}{I_{xx}} \end{bmatrix} \begin{bmatrix} F_{m,y} \\ M_{m,x} \end{bmatrix} \tag{10.5}$$

$$\begin{bmatrix} F_{m,y} \\ M_{m,x} \end{bmatrix} = \begin{bmatrix} \frac{1}{m} & \frac{d_1}{I_{xx}} \\ \frac{1}{m} & -\frac{d_2}{I_{xx}} \end{bmatrix}^{-1} \begin{bmatrix} a_1 \\ a_2 \end{bmatrix} = \begin{bmatrix} \frac{m \times d_2}{d_1+d_2} & \frac{m \times d_1}{d_1+d_2} \\ \frac{I_{xx}}{d_1+d_2} & \frac{-I_{xx}}{d_1+d_2} \end{bmatrix} \begin{bmatrix} a_1 \\ a_2 \end{bmatrix} \tag{10.6}$$

The equation can now be modified to express the force and moment at the wheel-mass interface in terms of the accelerations a_1 and a_2. While the force is the same, the moment at the interface is related to the moment at the centre of mass by:

$$M_x = M_{m,x} - F_{m,y} \times d_2 \tag{10.7}$$

The final equation then becomes:

$$\begin{bmatrix} F_y \\ M_x \end{bmatrix} = \begin{bmatrix} \frac{m \times d_2}{d_1+d_2} & \frac{m \times d_1}{d_1+d_2} \\ \frac{I_{xx} - m \times {d_2}^2}{d_1+d_2} & \frac{-I_{xx} - m \times d_1 \times d_2}{d_1+d_2} \end{bmatrix} \begin{bmatrix} a_1 \\ a_2 \end{bmatrix} \tag{10.8}$$

Note that in the reference paper the equation is slightly different. The term $d1 \times d2$ appears as d_1^2. However, in another paper [52] the same authors report $d1 \times d2$. It is concluded that a mistake was made in the first reference. Furthermore, the transformation in Equation (10.7) reported in the paper has the opposite sign in both references. However, as aforementioned, this is not consistent with the sign convention of Equation (10.4). During processing of the test data both options were implemented to verify this reasoning. The equation reported here yielded the exact same relation between the force and moment plots as reported in the reference paper. The equation given in the paper, however, produced completely inconsistent results. Furthermore, first calculating the moment around the centre of mass, and then applying the transformation directly with the calculated forces yielded the same relation between force and moment plots. It is clear that there is an issue with sign convention. Therefore, this approach is considered valid. Results are shown in Section 11.6.

For a symmetrical test bench the forces and moments in y and x direction are equivalent. In other words, two acceleration measurements are sufficient to compute the radial forces and moments.

$$\begin{bmatrix} F_y \\ M_x \end{bmatrix} = \begin{bmatrix} F_x \\ M_y \end{bmatrix} \tag{10.9}$$

With the second pair of accelerometers at location three and four, the axial disturbance force F_z can be derived in the same way by filling in eq. (10.4). Note that d_3 is equal to d_4.

$$\begin{bmatrix} a_3 \\ a_4 \end{bmatrix} = \begin{bmatrix} \frac{1}{m} & \frac{1}{m} \\ \frac{d_3}{I_{xx}} & \frac{-d_4}{I_{xx}} \end{bmatrix} \begin{bmatrix} F_{m,z} \\ M_{m,x} \end{bmatrix} \tag{10.10}$$

$$\begin{bmatrix} F_z \\ M_{2,x} \end{bmatrix} = \begin{bmatrix} \frac{m}{2} & \frac{m}{2} \\ \frac{I_{xx}}{2d_3} & \frac{I_{xx}}{2d_3} \end{bmatrix} \begin{bmatrix} a_3 \\ a_4 \end{bmatrix} \tag{10.11}$$

The axial disturbance moment $M_{m,z}$ is actually negligible "*due to wheel imbalance and bearing imperfections as well as electromechanical sources such as cogging and ripple*" [32][p.4]. The moment $M_{m,x}$ calculated can be checked with the second measurement.

Sizing of the test bench

For sizing of the seismic block there are three main considerations. First, a lighter seismic mass leads to larger accelerations, and so they can be measured more accurately (improved signal to noise ratio). Second, the mass determines the natural frequency of the suspended system. Ideally, the test bench has no eigenfrequencies in the test range from 0-1500 [Hz]. Finally, it should be large enough to fit a three-wheel assembly.

The eigenfrequencies of the test bench are direction-dependent. In the x and y direction (as defined in fig. 10.3) the bench behaves like a pendulum. In the z-direction it behaves as a mass-spring system with 4 parallel springs. Furthermore, the block itself has structural vibration modes. In Zhou et al. [53] an eigenfrequency of below 2.5 [Hz] is reported without specifying how this value is computed, and for which direction it holds.

The motion of the test bench in the x- and y-direction is approximated by that of a pendulum. It is assumed that the two ropes attached to each side of the block can be treated as a single rope. The torque about the centre of mass of the block corresponds to its angular acceleration and its moment of inertia about the centre of mass.

$$\tau = I_{cm} \times a \tag{10.12}$$

At any given time the torque is due to the 'restoring force', i.e. the component of the pendulum's mass, m_{block}, in the y direction times the length, L_{cm}, of the pendulum.

$$|\tau| = mg \times \sin(\theta) \times L_{cm} \tag{10.13}$$

The angle between the z axis and the pendulum string is θ. For small angles, a condition which holds for practical operations of the test bench, the equation of motion is:

$$a \approx -\frac{mgL_{cm}}{I_{cm}}\theta \tag{10.14}$$

This is actually a simple harmonic equation for which a general solution is:

$$\theta = A \times \cos(f \times t - \phi) \tag{10.15}$$

Taking the second derivative yields the general equation of motion:

$$\frac{d^2\theta}{dt^2} = a = -f^2 \times (A \times \cos(f \times t - \phi)) = -f^2 \times \theta \tag{10.16}$$

The natural frequency of the pendulum f is then given by:

$$f = \sqrt{\frac{mgL_{cm}}{I_{cm}}} \tag{10.17}$$

In the z direction the system is approximated by a simple mass-spring system. The 4 ropes are modelled as parallel springs, which allows adding up their contributions. The natural frequency of oscillation is then given by:

$$f_n = \frac{1}{2\pi}\sqrt{\frac{k_{eff}}{m}} \tag{10.18}$$

where k_{eff} is the sum of the individual effective spring constants. It is likely that this data is not known for an off-the-shelf rope. Instead, the spring constant must be determined experimentally or extracted from test data. Nonetheless, for sizing of the bench the equation illustrates that a large weight of the seismic mass is desirable for a low natural frequency system.

The seismic block itself has structural vibration modes that can be computed using CATIA's Generative Structural Analysis workbench. These modes should also be outside the test range of 0-1500 [Hz].

Apart from this, the seismic block shall fit larger reaction wheels and three-wheel assemblies. The block shall therefore have a square top surface of 15x15 [cm] and be symmetrical in the x and y directions (as defined in fig. 10.3). The length of the pendulum, L_{cm}, is assumed to be 0.1 [m] and the seismic mass is made out of Aluminium.

Using a Matlab script the different eigenfrequencies have been calculated for three different masses. The outer dimensions are fixed. Results are presented in table 10.3. For a pendulum the frequency increases with mass, while for a mass-spring system this is not the case. This suggests there is an optimum mass at which the two frequencies are equal. Once the rope spring constant is measured this can be determined. For now, the test bench has a wall thickness of 1.5 [cm] and outer dimensions of 15x15x15 [cm], to keep structural vibration modes above 1500 [Hz] and natural frequencies low.

Table 10.3: Test bench sizing results

Wall thickness [cm]	Mass [kg]	I_{xx} [kgm^2]	I_{yy} [kgm^2]	f_x [Hz]	f_y [Hz]	1st structural vibration mode [Hz]	Mininum expected acceleration [10^{-5} g]
1	2.27	0.015	0.012	7.46	8.62	1225.7	0.9029
1.5	3.28	0.02	0.016	10.03	11.58	1502.8	0.4763
2	4.21	0.024	0.02	13.12	7.02	2122.8	0.3363

Final design

The final design is shown in Figure 10.4. The seismic mass will be suspended from the support rods using a rope.

10.7. Integration and calibration

The test bench was successfully integrated and characterised. Disturbances by the reaction wheel are easily measurable with the reference accelerometer eliminating the need for the piezoelectric bimorph sensors. A block diagram of the complete test setup is shown in Appendix D.3.

Pictures of the test bench after manufacturing and in the actual test setup can be seen in Section 10.7. The seismic mass has threaded holes where both the reference accelerometer and the piezoelectric sensors can be mounted on all sides. Note that the holes for the mounting of the accelerometers on the top were drilled later. The wheel is directly mounted to the top using 4 M1 screws. Because larger aluminium plates were not cheaply and readily available the bottom plate had to be oriented diagonally to fit the seismic mass. Both the accelerometer and the bimorph cables introduce unwanted load paths that are not considered in the analysis, however

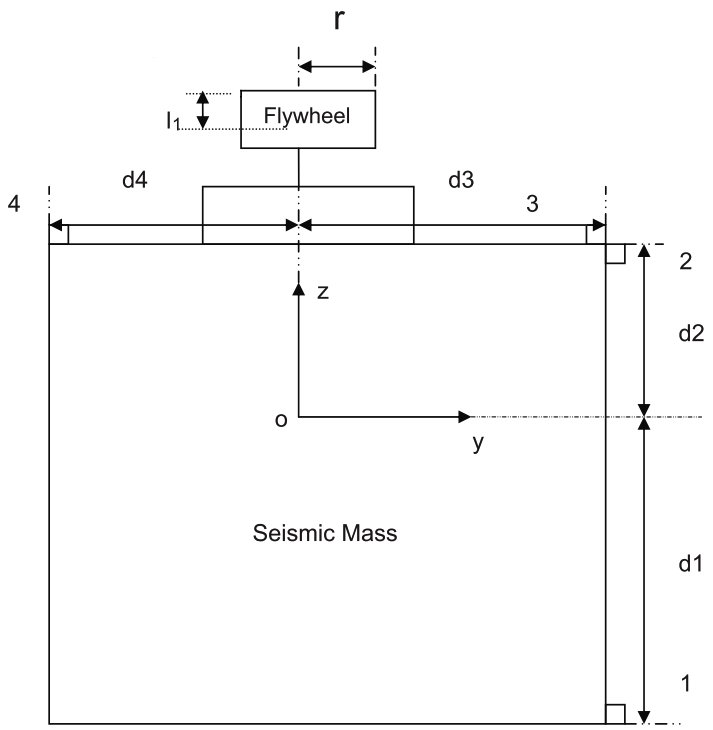

Figure 10.3: Schematic of test bench with accelerometer locations 1-4 [53]

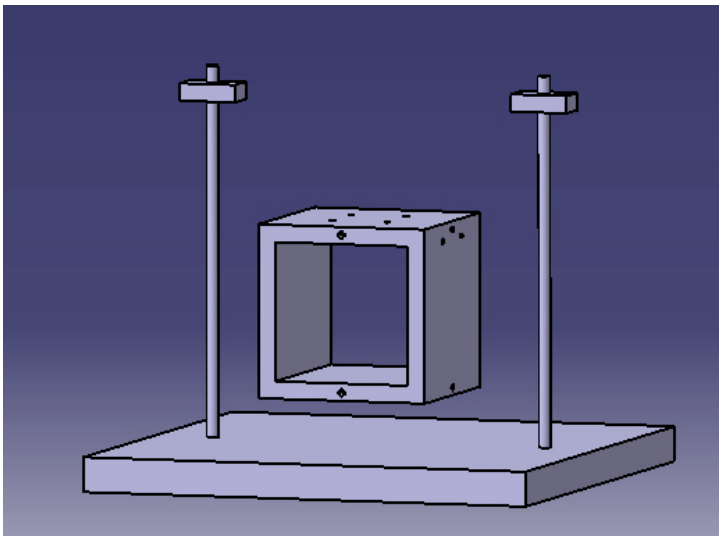

Figure 10.4: CATIA drawing of the test bench

this effect is evaluated in the random uncertainty of the measurements. The entire test bench is placed on a passive vibration isolation table.

The eigenfrequencies of the test bench are derived from swing tests in each direction. The reference accelerometer was used to measure the frequency of free motion after perturbation from rest state. The largest frequency of 10 [Hz] is in the z direction. The effective measuring range is therefore 10-1000 [Hz], constrained by the accelerometer.

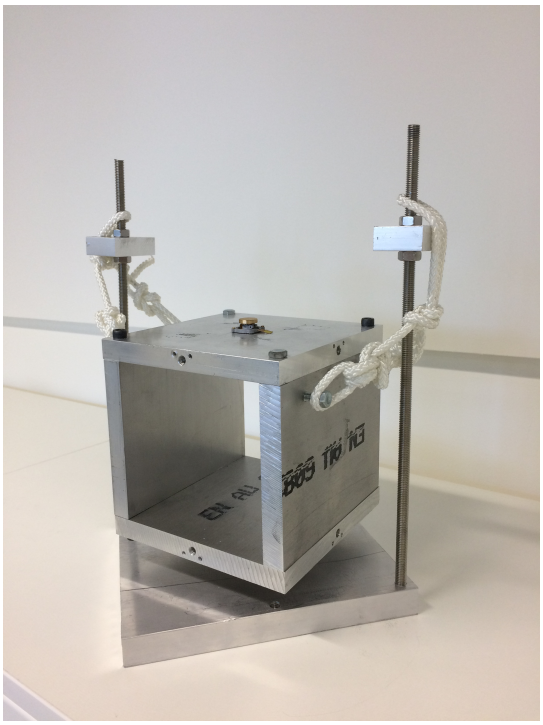

(a) Test bench after integration

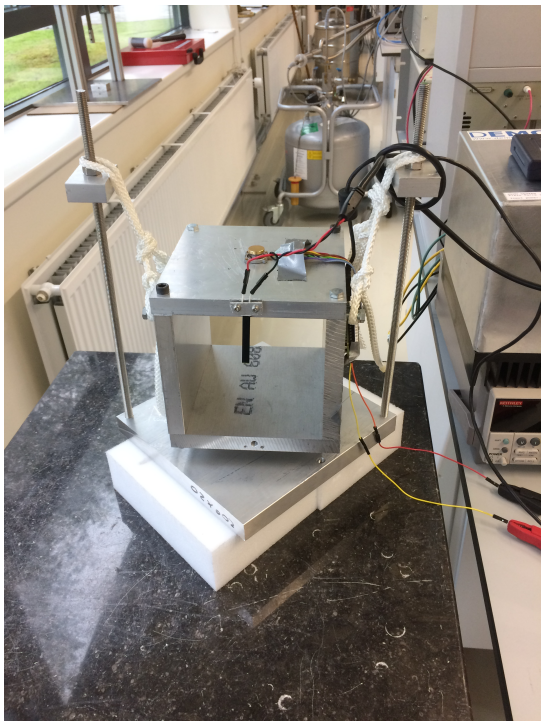

(b) Test bench in actual test setup

The measurement sensitivity of the reference accelerometer is sufficient to characterise the reaction wheel, but future better stabilised wheels might still require higher sensitivity. Therefore, the calibration is still considered briefly. Measured accelerations for each of the three piezo bimorphs and their respective reference accelerometer measurements are shown in Figure 10.6. Overall, the sensors correctly identify the peaks corresponding to the wheel speed within their frequency range but the slope traced by the peaks only matches that of the reference accelerometer within a more limited bandwidth. Near and above resonances false peaks are produced, and the output is non-linear. Below about 50 [Hz] no output can be produced, which was already observed in initial calibration testing. Above about 300 [Hz] all bimorphs miss a few or produce more peaks than the reference data shows, which is due to their fundamental and higher resonance frequencies. Overall, the bimorphs could be used to measure accelerations between 50 and 300 [Hz], if outside their resonance frequency, but above 300 [Hz] they can be used to identify structural resonances of the wheel. For this their output has to be compared; if a peak shows up on all three outputs it is likely to be real. Nevertheless, both the medium length and the short piezo have voltage sensitivities below that of the reference accelerometer, and the longest bimorph has the poorest performance. The sensitivities could be increased, but at the cost of reducing their effective measurement range. Because the disturbances are large enough to be measured, the bimorphs are not considered further. Instead, individual measurements at the accelerometer locations with the reference accelerometer will be combined. The reproducibility of the results must be proven in this approach. This is discussed in Section 11.6.

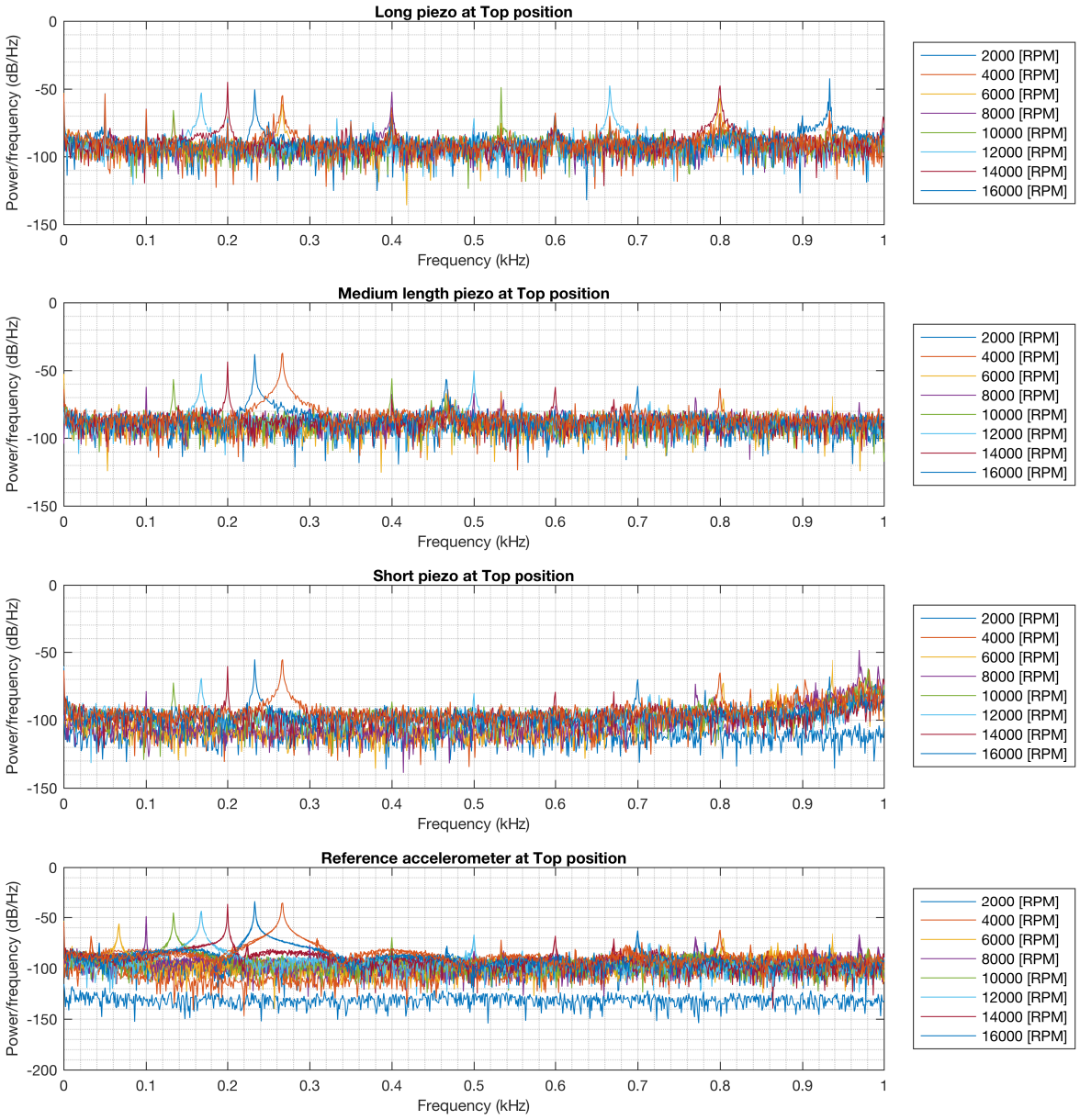

Figure 10.6: Piezoelectric bimorph calibration results

10.8. Verification & Improved design

The test bench mostly complies with the requirements. The measurement range is restricted to 10-1000 [Hz], due to the accelerometer, but this is sufficient to capture higher harmonics at up to 4.5 times the wheel speed. It has a sufficiently high eigenfrequency and fits much larger reaction wheel assemblies. Unwanted load paths and imperfect mounting of the reaction wheel introduce random uncertainties that can be reduced further. The test bench was operated on a passive vibration isolation table and cost less than 1500 Euro including accelerometer.

The test bench's measurement range and practicality can be improved by replacing the two-rope suspension with a single high-stiffness wire, e.g. fishing wire, in its centre, or by its 4 corners. This will allow for a longer pendulum arm, and thus a lower eigenfrequency. The accelerometer disturbs the balance of the test bench through its weight, so a mass dummy can be mounted on the opposite side to counter this. This will keep the test bench level, and it will be symmetrical, as is assumed in the analysis. Apart from this, the load paths mainly due to the accelerometer and the motor cables should be considered as they introduce random variations in the test results.

10.9. Chapter summary

Based on identification of acceleration as measurement variable and its expected magnitude a microvibration test bench was developed to characterise the disturbances created by the reaction wheel. The test bench isolates the disturbances through suspension of a seismic mass , effectively filtering parasitic vibrations. The use of a piezoelectric bimorph sensor to measure very low level vibrations was considered, but the actual vibration levels and far superior performance of the reference accelerometer led to the conclusion to not pursue their use further at this stage. In the future, should the flywheel's balance be improved their use might still be considered for identification of resonance peaks or measurement of accelerations in restricted frequency ranges that lie beyond the sensitivity of the reference accelerometer. The test bench can measure accelerations in the range of 10-1000 [Hz] with a sensitivity of 10.36 [V/g]. However, unwanted load paths due to cables and problems with rigidly securing the reaction wheel led to a high, but acceptable, measurement uncertainty. Specific suggestions for improving the design include changing the suspension of the seismic mass and using two accelerometers instead of one.

11

Verification and Validation

Verification and validation of the prototype reaction wheel involves establishing that it has been developed to specification, and that it can fulfill the needs of the PocketQube. The latter typically includes functional testing in a representative environment, which unfortunately is not possible as the ADCS of the PocketQube is not yet developed. Therefore, the design is only verified in this chapter. Both the tests and the conclusions are presented first at the component level, then at the overall reaction wheel level. All requirements and their verification results are shown in Figure 11.9.

11.1. Motor

Results of the tests performed on the motor were presented in Section 8.1. The requirements including verification result are shown in Figure 11.9. In conclusion, the power consumption is much lower than the datasheet value suggests. On the other hand the motor weighs 50 % more than the datasheet value.

11.2. Flywheel

The flywheel dimensions and mass are measured using a digital caliper and scale. The results are shown in Table 11.1. The flywheel was manufactured to specifications, but the actual material has a lower density than was assumed in the calculations. In future manufacturing the exact density should be agreed on with the manufacturer. The overall effect of this is considered in the functional tests of the motor with the attached flywheel.

Table 11.1: Flywheel parameters

Flywheel Requirement	**Target**	**Actual value**	**Uncertainty**
Diameter [mm]	14	14.01	0.01
Thickness [mm]	2.8	2.81	0.01
Manufacturing precision [mm]	0.1	0.1	0.01
Mass [g]	3.08	2.88	0.02

11.3. Housing

The housing design is verified by measuring its physical properties and assessing how well it provides a vacuum proof seal. Verification of the dynamic structural properties of the housing is done as part of the vibration tests in Section 11.5.

Physical parameters are measured using a digital caliper and scale. Results are given in Table 11.2.

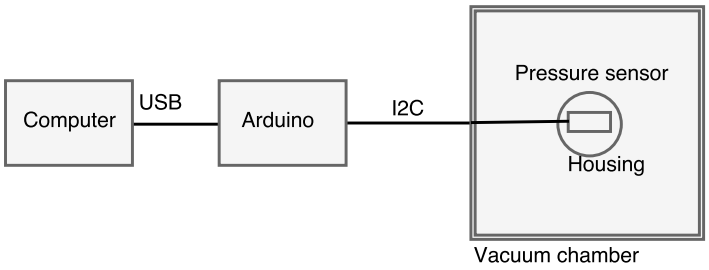

Figure 11.1: Housing pressure test block diagram

The two housing designs are tested in a pressure chamber. The test setup is shown in Figure 11.1. The pressure sensor (MS5607) is read using an Arduino Uno board via the I2C communication protocol using an open source code [44]. The pressure chamber achieves a vacuum of 50 [Pa]. Unfortunately, neither design had a functioning seal. The pressure dropped immediately when the vacuum chamber was turned on. It is likely that the aluminium of the housing itself was leaking due to poor manufacturing quality. Progressively more glue was applied to cover all possible leaks, but no complete seal was achieved, although the rate of leakage decreased. This indicates that either the glue itself or the cables connecting the pressure sensor to the Arduino Uno are leaking.

Table 11.2: Housing structural parameters

	Design A			**Design B**		
Housing Requirement	Target	Actual value	Uncertainty	Target	Actual value	Uncertainty
Mass [g]	6	5.15	0.01	6	3.10	0.01
Diameter [mm]	20	19.99	0.01	18	18.00	0.01
Height [mm]	12	12.36	0.01	11.80	0.01	0.01
Wall thickness [mm]	2	2.1	0.1	1.1	0.1	0.1

11.4. Functional testing

The effect of the flywheel on the performance of the motor is tested using the same test setup as in Section 8.1, which is described in detail in Appendix D.

Characteristic performance plots are shown in Figure 11.2, and the power consumption breakdown in Figure 11.3. The power consumption has increased by about 35% compared to the motor performance plots in Section 8.1. As is clear from the power breakdown the friction losses drive the power consumption. Figure 11.4 shows that the addition of the flywheel reduces the variations in dynamic current consumption. Therefore, the increased power consumption is not due to control problems but must be due to increased friction, which is caused by the flywheel. Furthermore due to the increased friction loss the copper loss has increased, and the drive electronics dissipate more power as well. The no-load current has increased to about 7 [mA], which means that less current is available to generate torque, which can be seen in the torque graph. Apart from this, it is clear that the controller has more difficulty controlling the speed of the wheel in a maximum acceleration scenario.

At steady state the control accuracy is constant at around 80 [RPM], but as a percentage of the absolute speed it increases considerably. The minimum required torque of 2.93×10^{-4} [mNm] can be delivered at well above the required maximum useful speed. This is expected as the no-load current of the motor was below the data sheet value. The verification results for the performance requirements are presented in Figure 11.9.

Two operational scenarios are considered. A zero-speed crossing is run with an deceleration/acceleration of three rpm/s, which corresponds to the average rate over one orbit (max useful speed of 13500 [RPM] divided by the orbital period). This is done for the motor and for the motor with flywheel separately. Second, fast changes in velocity at a rate of 200 [rpm/s] are performed. In both scenarios the current and velocity are measured. Voltage measurements, especially at low velocities, are not possible as explained in Appendix D.1. Therefore

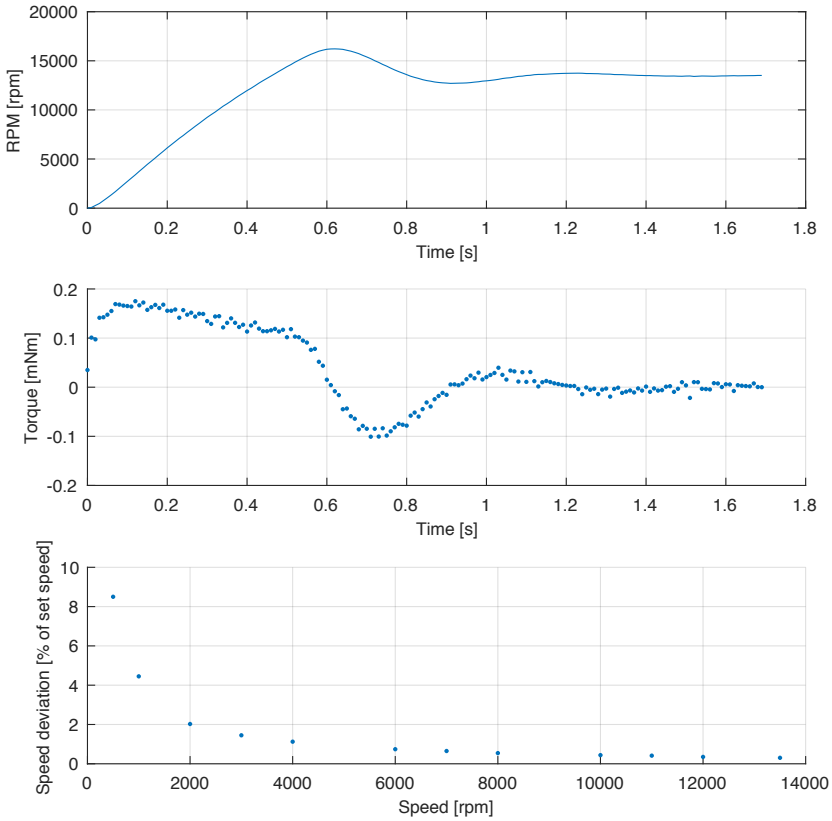

Figure 11.2: RW functional test

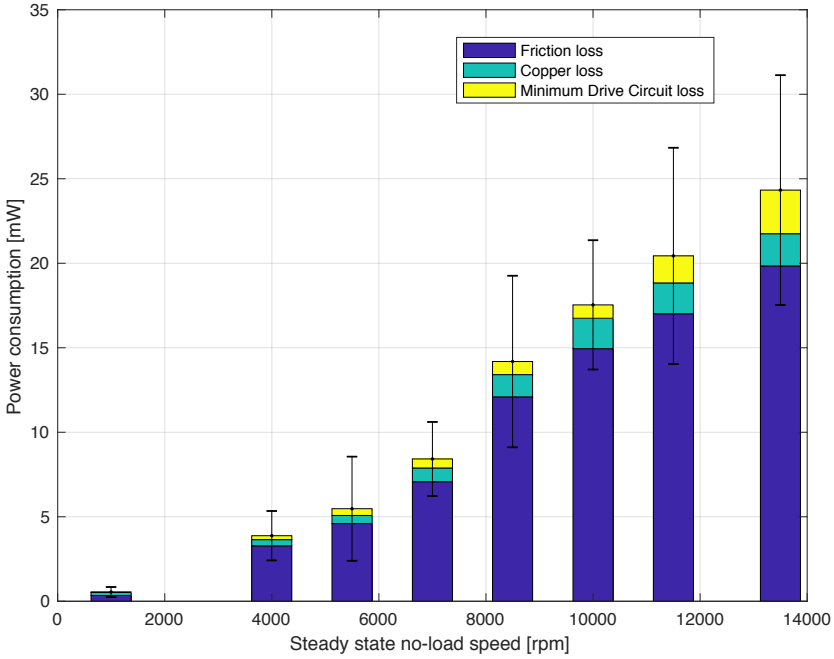

Figure 11.3: Breakdown of RW power consumption

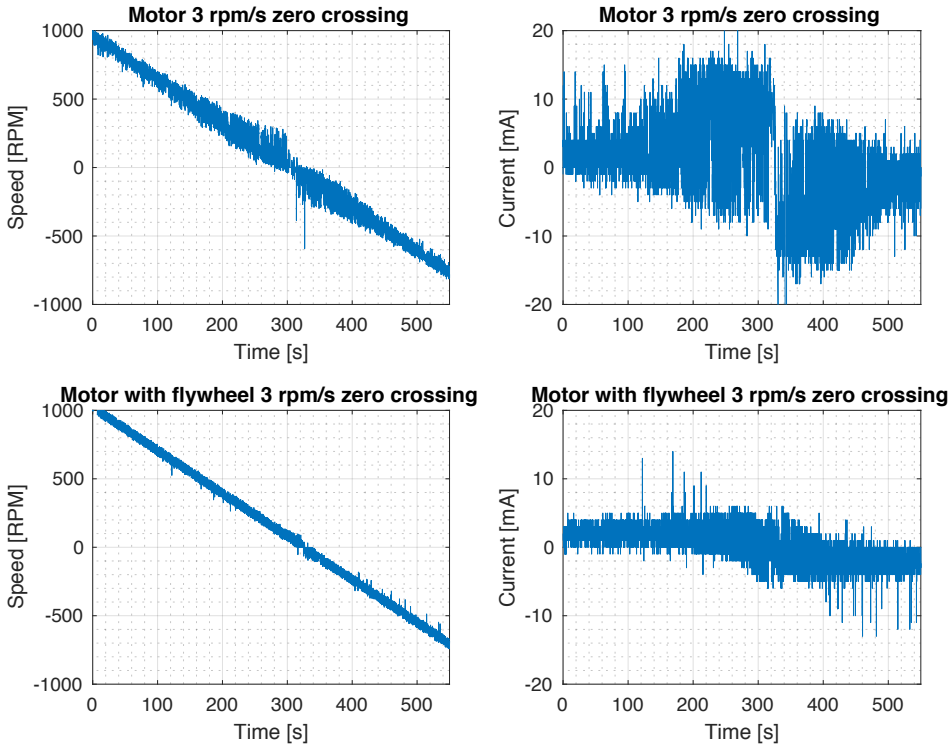

Figure 11.4: Zero speed crossing at three rpm/s

measuring the dynamic power consumption is not possible. Results can be seen in Figure 11.4 and Figure 11.5.

Interestingly, the dynamic current consumption is reduced by the addition of the flywheel, because the increased inertia reduces the speed overshoot. The error decreases by about a factor of two in the speed range -100 to +100 [rpm] for the motor with flywheel. Outside this range the speed error is on average 80 [rpm]. These results are not directly representative of the RW performance in the PocketQube because the behaviour depends strongly on the control parameters and control method. However, they can serve as a benchmark to evaluate the performance of the dedicated control electronics that will be developed in the future.

The fast change scenario does not show an improved zero-crossing control accuracy, as the second zoomed in plot shows. The current consumption also shows large peaks around the zero-crossing. There is little overshoot when a steady state at larger values is reached, although some current peaks are related to this. This is controller specific behaviour and so is not investigated in more detail.

11.5. Vibration testing

The reaction wheel assembly is tested to verify it can survive the accelerations during launch in axial and radial direction. The complete test is described in Appendix D.

Test overview

The test setup is shown in Figure D.4. The shaker is driven by a power amplifier, which in turn is supplied either with a sine signal from a signal generator or with a random signal generated in Matlab. The reaction wheel and an accelerometer are mounted on the shaker via an interface structure. Vibration data is processed in Matlab. The wheel is qualified for representative launch loads of small satellite launch opportunities. The test procedures and qualification levels are summarised in Table D.1. Only NanoRacks random qualification loads have not yet been tested. Sine sweeps before, during and after the sine and random vibrations are performed to identify changes in resonance peaks that could indicate mechanical damages.

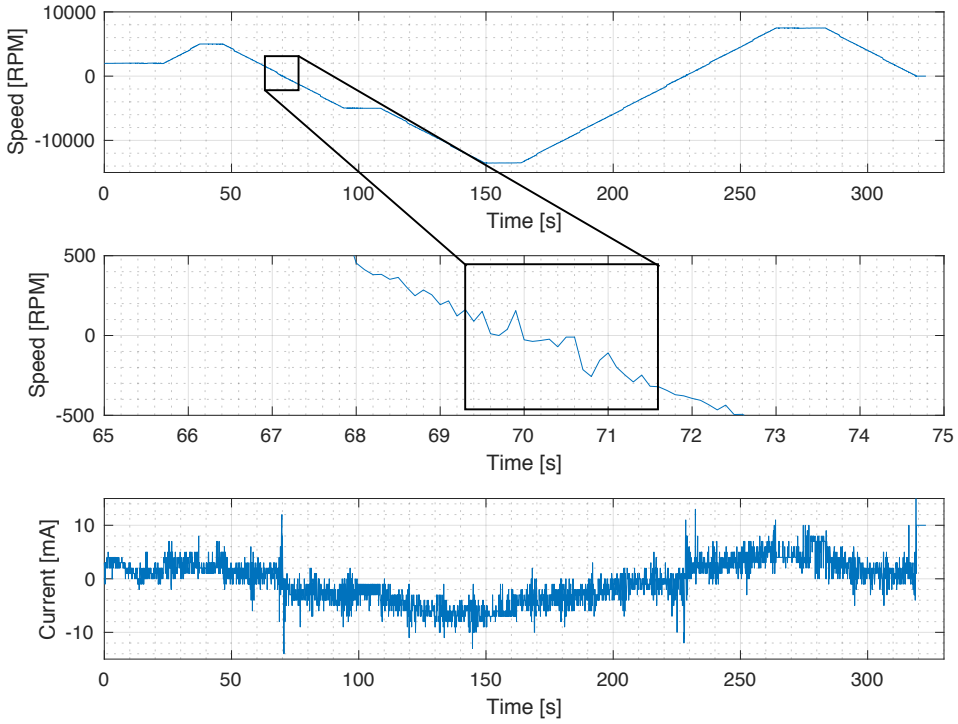

Figure 11.5: Fast speed changes at 200 rpm/s

Test Results

The reaction wheel showed no measurable performance degradation after the vibration tests, but some additional noise after the radial direction tests indicates minor damages.

The results for the 7.2 [g] axial and radial random vibration test are shown in Figure 11.6 and Figure 11.7, respectively. The bottom two plots are the shaker response with the reaction wheel attached to the structural interface. The 6 measurements are overlaid to show that the differences over time are small. The average load over the 120 [s] duration is 7.186 [g] in the axial, and 7.329 [g] in the radial direction. The required sine loads could not be achieved under 40 [Hz] because of mechanical limitations of the shaker.

Functional tests showed no performance degradation in terms of power consumption and motor parameters. However, after the radial vibration tests the wheel makes more noise indicating minor mechanical damages that could have an effect on the lifetime of the wheel. It is presently unclear whether there is any damage to the bearings, or if the wheel imbalance increased due to either a shift of the flywheel or deformation of the rotor axis. To assess whether there is any impact on the lifetime long-term functional testing is required. Future steps may include inspection of the bearings after vibration tests, and more steps in the tests to identify the mechanical limits.

The eigenfrequencies of the reaction wheel can be identified from the axial vibration tests by comparing the response of only the shaker to the response with the reaction wheel attached. This was not possible using the radial test data because of the added mass of the additional interface required to mount the RW sideways, which reduced the relative contribution of the wheel to the structural response of the moving platform. Specifically, when comparing the bottom two rows in Figure 8.2a a shift in resonance peaks can be observed. This is due to the added mass of the reaction wheel. This effect was not observed in the radial direction tests. It is recommended for future vibration testing to manufacture a lighter interface.

The first eigenmode of the wheel is identified at 3.5 [kHz], although the peak at around 1 [kHz] has a larger magnitude. Whether this is due to the time-varying changes in the input signal or because the wheel has an eigenmode at that frequency is not clear from this plot. However, no additional peak was observed in the radial test data at 1 [kHz] either. Eigenfrequencies of the wheel should be above 200 [Hz]. During the sine sweep

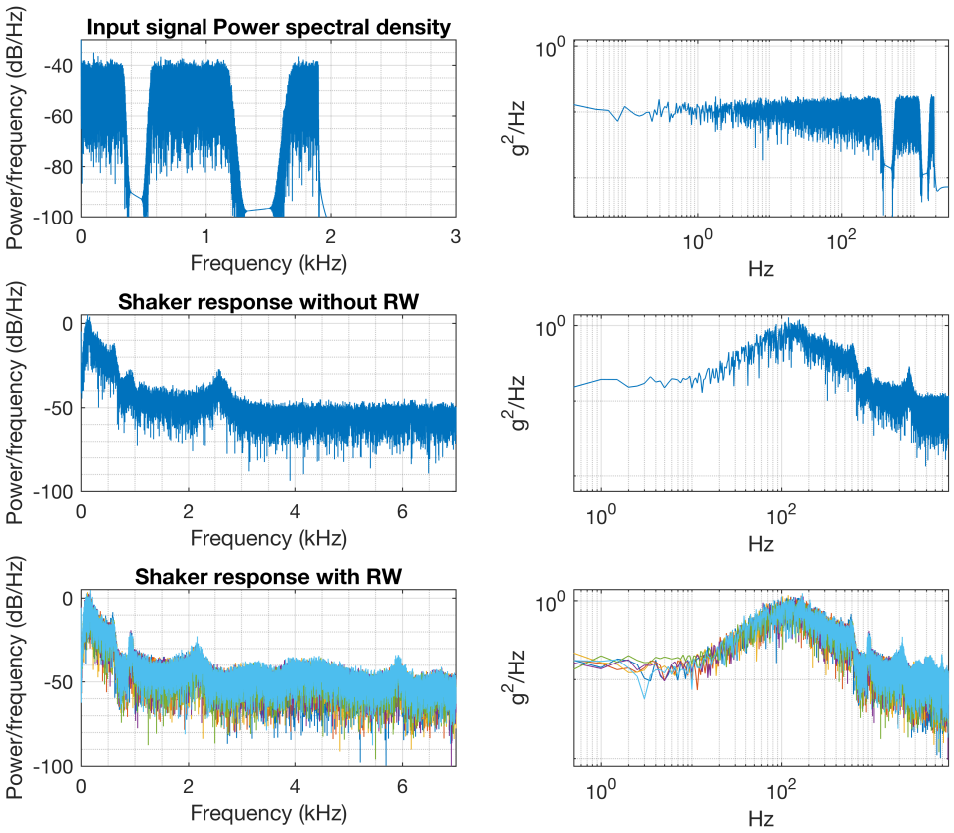

Figure 11.6: Axial vibration test results PSD plots

from 0-800 [Hz] no additional resonances were identified and the test data show no additional resonance peaks below 3.5 [kHz].

11.6. Micro-vibration testing

The test setup for micro-vibration tests is identical to the one used during calibration testing of the piezoelectric bimorphs, which is shown in Figure D.6. Further details about the test setup such as the uncertainty analysis are presented in Appendix D.3. Tests were performed for an undamaged wheel. Due to time constraints only measurements at locations 1 and 2 were possible. This means that the force in y-direction is not experimentally measured, however it is smaller so for verification purposes not relevant.

The results are shown in Figure 11.8. The force and moment in x and y direction are equivalent. The moment and force graphs have the same shape, and the moment is about a factor of 10 smaller than the force. This is the same relation presented in the paper the test bench design is based on [53]. Their magnitude is about 20 times smaller than reported in the paper. Unfortunately, the mass of the reference wheel is not reported, but it looks to be about 1 to 2 orders of magnitude larger, which fits the magnitude difference.

The general shape of the curves is as expected; a rotating mass imbalance produces a torque that increases with ω^2. Around 10000 and 12000 [RPM] there is a local peak which indicates some structural resonance. At the same time, the random uncertainty of the measurement increased. The wheel was verified to not have structural eigenmodes in this frequency range, so this effect is likely due to the mounting of the wheel on the seismic mass. The wheel is screwed directly into the seismic mass with 4 M1 screws. However, the drill holes could not be tapped with such a small diameter screwthread, so some of the screws are not fixed well. Again, due to time constraints only one round of testing was possible.

The theoretical disturbance force and moment calculated for the Delfi-n3Xt reaction wheels [22] is about the same magnitude as the experimental resutls. Delfi-n3Xt wheels had a flywheel about twice as heavy and maxi-

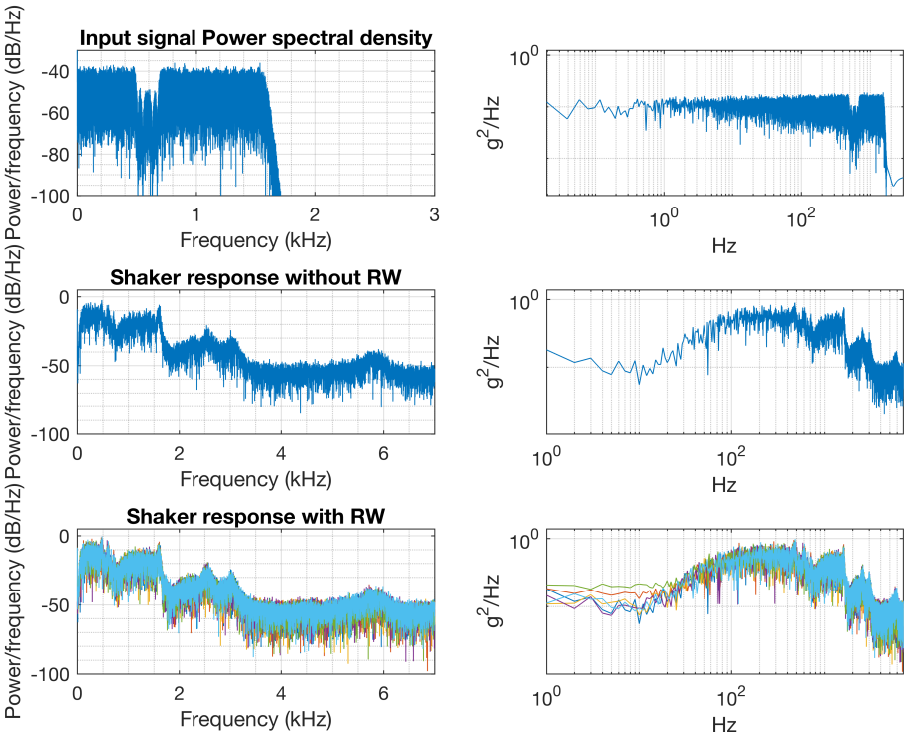

Figure 11.7: Radial vibration test results PSD plots

mum rotation speed up to twice as fast. These results were not experimentally validated, but they indicate that the imbalance of the Delfi-PQ wheels is larger.

With respect to requirement RW-IN4 that specifies a maximum disturbance moment of 0.0041 [Nms] the reaction wheel is not compliant above about 4000 [RPM]. This means that Earth observation scenarios are limited by the flywheel disturbances rather than the speed control accuracy. However, this imbalance can be improved by manufacturing a flywheel that better fits the rotor dimensions. Because of production uncertainties in the motor dimensions there is a gap between the flywheel and the mass of 0.11 [mm], which during integration partly fills with glue and leads to an imbalance of the wheel.

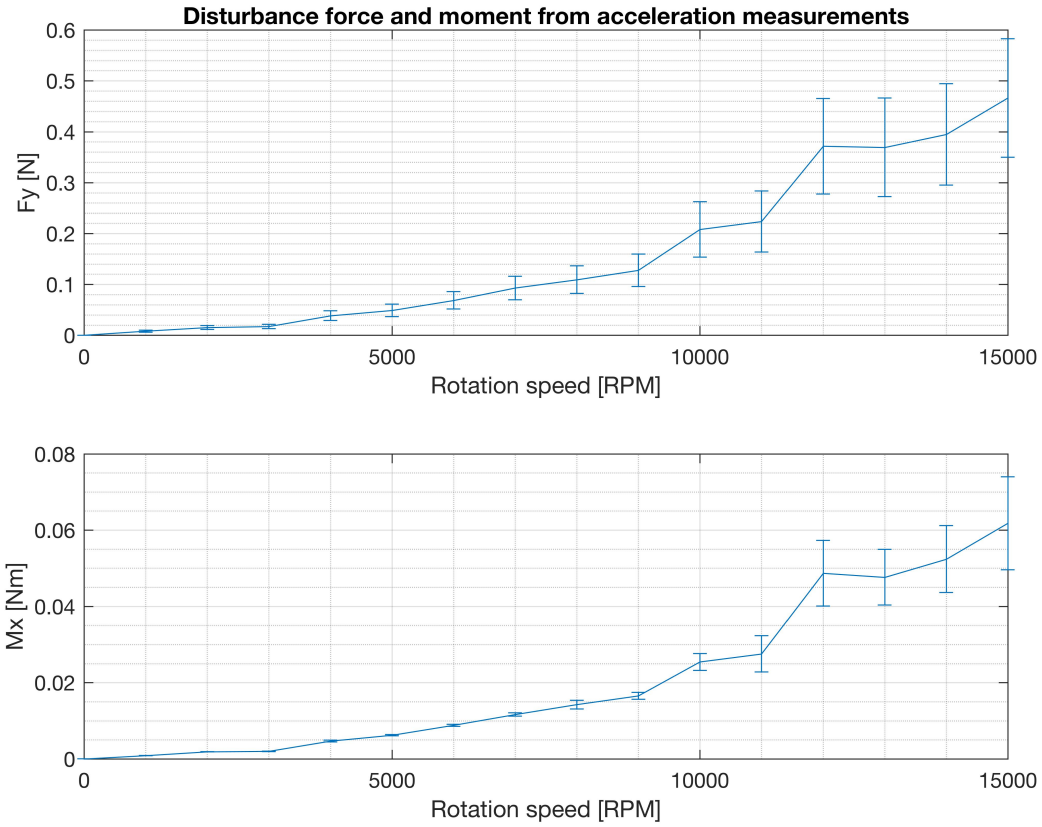

Figure 11.8: Results microvibration test

Requirement verification matrix					
Reaction wheel level requirements					
Functional requirements	**Verification status**	**Target value**	**Actual value**	**Verification method**	**Explanation**
SYS-F1. The RW shall be able to generate torque around its rotation axis. SYS-F1.1 The RW shall be able to accelerate/decelerate to counter disturbances. SYS-F1.2 The RW shall be able to accelerate/decelerate at the required rate over its operational speed range. SYS-F2. The RW shall be able to store angular momentum around its rotation axis. SYS-F2.1 The RW shall be able to counter the total disturbance momentum over one orbit. SYS-F2.2 The RW shall be able to control its speed. SYS-F2.3 The RW shall be able to determine its rotation speed.					
Performance requirements	**Verification status**	**Target value**	**Actual value**	**Verification method**	**Explanation**
SYS-P1. The RW shall be able to store at least 1*10^-4 Nms angular momentum about its rotation axis in one direction of rotation.	Verified	1*10^-4 [Nms]	1.08*10^-4 [Nms]	Test	max torque motor can deliver with 10mA current limit
SYS-P2. The RW shall be able to generate at least 2.93*10^-3 Nm of torque around its rotation axis over its operational speed range.	Verified	Tmin at 13500	Tmin at 14700 rpm	Test and Analysis	
SYS-P3. The RW shall not generate instantaneous disturbance torques larger than 0.0041 [Nm].	Verified	4.1 [mNm]	0.021 [Nm]	Analysis	
SYS-P4. The RW shall not have a momentum error of larger than 0.134*10^-7 [Nms] Nms over half an orbit.	Verified	3.08*10^-5 [Nms]	7.81*10^-7 [Nms]	Test	
SYS-P5. The RW shall be able to determine its rotation speed to within 10 [rpm].	Not verified	10 [rpm]		Test	
SYS-P6. The RW shall be able to control its rotation speed to within at least 300 [rpm] of the desired value.	Verified	300 [rpm]	90 [rpm]	Test	
SYS-P7. The RW shall have a nominal power consumption of 15 [mW].	Not achieved	15 [mW]	24.9 [mW]	Test and Analysis	Power required to deliver Tmin at max speed
SYS-P8. The RW shall have a lifetime in space for at least one year.	Not verified				
Physical requirements					
RW-PH1. The housing shall provide structural support for the motor and flywheel.	Verified	3g sine and 7.2g random vibrations	3g sine and 7.2g random vibrations	Test	
RW-PH2. The housing shall contain an airtight sealed environment with 1 atmosphere pressure.	Not achieved	-		Test	
RW-PH3. The RW shall weigh less than 8g.	Verified w.a.m.	8 [g]	TBD	Test	depends on succes of housing pressure tests
RW-PH4. The RW shall ideally measure less than 14x14x8 [mm], but for a first design it shall measure less than 20x20x12 [mm].	Verified w.a.m.	14x14x8 [mm]	20x20x12.37 for Design A; 18x18x12 for Design B		
RW-PH5. The RW shall have an eigenfrequency above 60 [Hz]	Verified	60 [Hz]	TBD	Test	
Environmental requirements					
RW-E1. The RW shall be able to operate between -15 and 45 degrees [celsius]	Verified	-15 to 45	max useful speed at 45 degrees sufficient to store Hreq	Analysis	
RW-E2. The RW shall be able to operate in vacuum.	Not achieved			Test	
RW-E3. The RW shall be able to withstand the radiation environment in Low Earth Orbit.	Not verified				

RW-E4. The RW shall be able to survive accelerations during launch with a root mean square value of 7.2 [g]	Verified	3 [g] sine, 7.2[g] random	qualified up to 3 [g] sine and 7.2 [g] random vibrations	Test	
Interface requirements					
RW-I1. The RW shall operate with the bus voltage of 3.3 [V].	Verified	-	-	Test	
RW-I2. The RW shall have a structural interface with the ADCS system.	Verified	-	-	Inspection	
RW-I3. The RW shall not generate electromagnetic disturbances that interfere with other subsystems.	Not verified		-		
RW-I4. The RW shall not generate disturbance torques larger than 0.0041 [Nm]	Not achieved		Only below 4000 [RPM]	Test	
Component level requirements					
Motor requirements	**Verification status**	**Target value**	**Actual value**	**Verification method**	**Explanation**
COM-M1. The motor shall have a nominal power consumption of 12 [mW].	Not achieved	12 [mW]	17.02 [mW]	Test	
COM-M2. The motor shall have rotor position sensors.	Verified			Test	
COM-M3. The motor shall have a mass below 1 [g].	Not achieved	1 [g]	1.21 [g]	Test	
COM-M4. The motor shall have a maximum speed as high as possible.	-				
COM-M5. The motor shall operate between -15 and 45 degrees celsius	Verified	-15 to 45	-40 to 85	Analysis	
COM-M6. The motor shall have maximum dimensions of 14x14x7.5 [mm].	Verified		9.89x9.89x6.13 [mm]		
COM-M7. The motor shall have a linear torque-velocity curve.	Verified				
COM-M8. The motor shall operate at 3.3 [V].	Verified			Test	
COM-M9. The motor shall survive launch accelerations of 7.156 [g] (RMS)	Verified		qualified up to 7.186 [g] random vibrations		
COM-M10. The motor shall have a lifetime of at least 1 year	Not verified				
Flywheel requirements					
COM-FL1. The flywheel shall have a maximum diameter of 14 [mm].	Verified		14.01 [mm]		
COM-FL2. The flywheel shall have a thickness such that it has a moment of inertia of 0.877 [gcm^2]	Verified w.a.m.		0.851 [gcm^2]	Analysis	
COM-FL3. The flywheel shall be glued to the rotor of the motor.	Verified			Inspection	
COM-FL4. The flywheel shall be manufactured out of bronze (rho= 8950 kg/m^3] with a precision of better than 0.1 [mm].	Verified w.a.m.		8400		
Housing requirements					
COM-H1. The housing shall provide structural support for the motor and flywheel, and interface with the 3-wheel assembly structurally.	Verified				
COM-H2. The housing shall seal off the motor under 1 atmosphere pressure.	Not achieved				
COM-H3. The housing shall survive random vibrations of 7.156 [g] (RMS) during launch.	Not verified		Not for complete assembly		
COM-H4. The housing shall survive sine vibrations of 2 [g] max. during launch.	Not verified		Not for complete assembly		
COM-H5 The housing shall ideally have a mass of less than 3 [g], but for a first design it shall weigh less than 6 [g].	Achieved		Design A 5.15 [g]; Design B 3.10 [g]		

Figure 11.9: Requirements verification matrix

V

Results

12

Conclusions and Recommendations

In this chapter conclusions to the research and recommendations for future work are discussed. Reflections on requirements, research questions and research goals are presented first, followed by the final specifications for the reaction wheel prototype. Then, the research objective and external aim of the thesis are evaluated and conclusions about the feasibility of using reaction wheels on a PocketQube are discussed. Finally, recommendations for improving the design are made.

12.1. Requirements compliance

The design complies with most requirements, although some have not been verified.

Performance requirements were verified in functional testing using the EPOS control electronics. The results are not directly representative of real operations, but can serve as a benchmark. The RW can deliver the minimum torque over its operational speed range and store the required angular momentum. Disturbances due to control inaccuracies are within the required margins and the speed can be controlled with sufficient accuracy to support Earth observation. The lifetime and motor speed determination accuracy are not verified. The power consumption requirement is met, depending on how the requirement is interpreted. The average power consumption is compliant, but at maximum speed the motor uses about 60% more power.

The RW complies with physical requirements for a first design, i.e. the initial design targets. The housing provides adequate structural support to the motor and housing and meets the eigenfrequency and structural strength requirements. However, the current housing design offers opportunities for optimisation in terms of providing a vacuum seal while reducing weight and volume. The preliminary three-wheel design in Section 9.6 indicates that volume constraints can be met for the PocketQube if all three wheels are included in one pressurised housing.

Environmental requirements have been partly verified. The RW can survive launch vibrations without measurable performance degradation, but some damage was identified after radial direction testing. The impact of this damage must be investigated further, e.g. as part of lifetime performance tests. Temperature effects are analysed theoretically indicating that performance changes are well within safety margins. In the future thermal vacuum tests of the RW are required. Apart from this, the effects of radiation are not tested.

Finally, interface requirements are partly met, but the control electronics and the ADCS are not yet developed so the interfaces will change. The motor can operate with the bus voltage, but this was not tested. The disturbances generated by the wheel itself are above Requirement RW-IN3 for rotation speeds above 4000 [RPM], i.e. observation scenarios are constrained by wheel disturbances rather than by the speed control accuracy of the controller. The housing serves as a shield against magnetic fields created by the motor, which is assumed to lead to compliance with the EMI requirements, but the efficacy of the shielding was not tested.

Overall the reaction wheel prototype development served to identify and evaluate key engineering aspects that provide a solid basis to develop a three-wheel assembly.

12.2. Answers to research questions

The research questions that were formulated to guide the research can now be answered.

1. What is the ideal performance of a reaction wheel

Separating ideal from real performance was not strictly possible because empirically determined motor parameters are required for the calculations that were used to select a motor, and are also important inputs for the Simulink model. However, the theoretical performance of the motor, without it being included in the reaction wheel, can be defined as its ideal performance. The performance is shown as part of the motor selection process in Section 5.5.

2. What effects lead to non-ideal performance and how can they be modelled?

Non-ideal effects are defined as those that determine the real performance of the motor, and by extension the motor with flywheel inside the reaction wheel housing. They can be separated into control electronics and reaction wheel effects.

The control electronics commutate the current flowing through the windings of the motor ensuring that magnetic fields are generated in the right sequence to rotate the rotor. The current itself is controlled using pulse-width modulation to control the rotation speed and acceleration, and thus the torque. Three main non-ideal effects are identified. First, over one electrical period the current switches 6 times from one combination of windings to the next. The time it takes for the current to adjust is very small, nonetheless the freewheeling behaviour gives rise to switching effects which lead to non-ideal waveforms and therefore torque ripples. Second, the speed is controlled with a PI control scheme, which also has a control error, i.e. variations from the set speed. Especially at low rotation speeds these disturbances are present (see Section 11.4) due to static friction of the rotor. The first two effects are modelled in the Simulink model in Chapter 7. Finally, the electrical parameters of the control electronics change with temperature, which influences the power consumption of the electronics.

For the reaction wheel there are mechanical and environmental effects that influence its performance. Fundamental disturbances are caused by static and dynamic imbalances of the wheel. They include mass imbalance and misalignment of the flywheel, and bending of the motor axle during rotation due to its finite stiffness. These disturbances are amplified at structural resonance frequencies of the reaction wheel. Wheel imbalances can lead to increased friction and therefore power consumption. Creation of a mechanical model for the reaction wheel lies outside the scope of this thesis, but measurements of the reaction wheel disturbances were performed that are suitable inputs for such a model. Environmental effects again include temperature changes as well as the vacuum and zero-g environment. The former leads to changes in the torque efficiency of the motor and its power consumption. Both are modelled as linear deviations from empirically determined parameters. Due to weightlessness the balls inside the motor bearings might float and not run ideally in their races, but this effect is countered by the wheel imbalance forcing the balls into their races. It is not modelled as part of this thesis because it is impossible to validate the model. Finally, in vacuum the bearing lubrication evaporates, so if the housing leaks the lifetime of the bearings is reduced.

3. What is the real performance of a miniaturised reaction wheel?

The real performance was measured during functional testing reported in Section 11.4 and in microvibration testing reported in Chapter 10. Compared with the measured performance of only the motor the reaction wheel uses about 35% more power and delivers less torque. This is likely because the imbalance of the wheel leads to increased friction, which in turn requires more current to be overcome. At a given voltage the control electronics can only 'force' so much current through the windings, so that the current available for producing torque is reduced. As a result the power consumption increases and the torque efficiency of the motor decreases. On the other hand, the increased inertia of the motor due to the addition of the flywheel reduced the control error especially at low rotation speeds, which is also reflected in the current consumption. However, because it was impractical to measure voltage during dynamic testing the dynamic power consumption could not be established with sufficient uncertainty. Microvibrations created by the wheel are several orders of magnitude above the required control torque, and constrain the performance of the reaction wheels. Criteria derived from Earth observation scenarios are only met for rotation speeds below about 4000 [RPM].

4. What is the power consumption of the reaction wheel in detail?

The total power consumption is separated into the contribution of the motor and the control electronics. The former was measured and the latter is estimated using the validated Simulink model. The detailed power consumption is shown in Section 11.4.

Power is consumed in the motor through friction and resistive heating. Electromagnetic effects such as hysteresis loss and eddy currents are included in the friction because they are also strongly speed dependent. Based on the comparison in power consumption between the motor and the reaction wheel the importance of a balanced flywheel becomes apparent as the imbalance drastically increased the friction, and thus the power consumption. It is possible that a part of the increased power consumption is due to eddy currents being induced in the flywheel or the reaction wheel housing which, made of bronze and aluminium, conduct electricity. Comparative tests between the motor fixed inside a plastic clamp and glued to the housing did not show a difference, likely because the measurement uncertainty was not sufficiently small. This effect can be investigated in more detail in future work once the dedicated control electronics are available and better accuracy current sensors are used. However, it is typically small for miniaturised motors. Furthermore, the power consumption is also dependent on the control strategy and efficiency of the controller. Constant overshooting of the target velocity consumes more power than an almost perfectly steady wheel. These effects can be modelled in the future once the actual drive electronics parameters are determined.

In the control electronics power is also lost due to resistive heating in the MOSFET switches and additional circuitry. Specifically, when a switch is ON current flows through the switch, and when the switch is OFF the current freewheels through the flyback diode. Furthermore, there is additional power lost due to the time taken for the current to rise and fall each time the MOSFET is switched. Further sources of power consumption could be MOSFET gate drivers and a current sensor, however these are not strictly necessary so the minimum power consumption is defined without their contribution.

12.3. Evaluation of research goals

Goals were identified to evaluate the project using objective success criteria.

The first goal was to model the RW's ideal motion and all non-ideal effects. This was not strictly achieved. The ideal motion was modelled in detail, but electromagnetic effects and disturbances were not modelled to limit the scope of the thesis. A future disturbance model can use the results from the microvibration tests, but modelling the electromagnetic effects is likely not practically relevant. Instead, the effects can be measured as explained in the previous section.

The second goal was to design, integrate and test the RW. This was mostly achieved, but some requirements were not verified. The preliminary design was used to draw conclusions about the flywheel placement and housing design. Motor tests were used to validate the Simulink model and the detailed design was integrated and tested. However, the lifetime performance of the reaction wheel was not tested and the wheel showed some damage after radial vibration testing. Furthermore, thermal vacuum tests of the complete assembly were not performed either and the design offers opportunities for optimisation. Microvibration tests were performed successfully although some improvements can be made to the test setup.

The third goal to characterise the power consumption was achieved, but the measurement accuracy was constrained by current measurement in the EPOS controller and the voltage measurements. The differences between ideal and non-ideal performance could therefore not be analysed in detail, but the effect of adding the flywheel was isolated, and the contribution of the control electronics was simulated. Electromagnetic effects could be investigated in the future to optimise the power consumption.

Overall, a working prototype of the reaction wheel was developed and tested. Analyses, models and results can be used to developed a complete three-wheel assembly with control electronics. Additionally, a test bench was developed that can be used to characterise micro-vibrations of the assembly.

Delfi-PQ Reaction Wheel Prototype Specifications	
Min. Torque [10^{-7} Nm]	3
One way momentum storage [mNms]	0.1
Mass [g]	7.6
Max. steady state power consumption [mW]	25
Dimensions [mm]	20x20x12
Operational temperature range [C]	-15 to 45
Operating voltage [V]	3.3

12.4. Reaction wheel prototype specifications

The specifications for the developed reaction wheel prototype given here are based on the largest housing design.

12.5. Research objective and external aim

The research objective was achieved, and clear opportunities for further work are identified. The prototype reaction wheel was developed successfully with clear points of improvement for subsequent iterations that are based on test results. Detailed analysis of the power consumption showed the importance of balancing the flywheel. Microvibration tests showed the relatively large disturbances created by the wheel that constrain its performance. Therefore, improving the balance of the wheel is the most important conclusion.

Based on test results for a single wheel and a design for a three-wheel assembly the external aim of the thesis is also met. If the balance of the flywheel is improved, and its housing can properly seal it from the vacuum of space, the reaction wheel will enable 3-axis stabilisation of picosatellites. At present Earth observation is not possible at high rotation speeds, but thrust manoeuvres can be performed. The proposed 3-wheel design, once developed, could take the miniaturisation of reaction wheel assemblies a step further still. This is required for launching a three-wheel assembly, integrated into the ADCS, on-board a PocketQube satellite. The power consumption was shown to not be prohibitive.

12.6. Recommendations

Recommendations for improvements on the design of the reaction wheel presented in this report are subdivided into modelling, design, integration and testing recommendations.

It is recommended to use the Simulink model as a design tool in development of the control electronics. Maximum currents in MOSFETs can be simulated and control strategies can be evaluated. To evaluate the dynamic behaviour of the model the architecture in the model should match the real controller architecture. Overall, a sensitivity analysis should be performed to assess the dynamic predictions. Apart from this, a full disturbance model of the reaction wheel that accounts for wheel imbalances can be developed, and validated using microvibration test data. This allows to better understand the dynamic and static imbalances of the wheel and axle, and to design the flywheel accordingly. Furthermore, the disturbance torques acting on the satellite should be simulated to derive a more precise requirement for minimum torque and momentum storage. With more information the safety margins could be reduced, effectively optimising the design.

In terms of design, it is crucial to develop the control electronics because they directly determine the behaviour of the reaction wheel. The presented three-wheel design should be analysed and expanded in more detail, with a focus on optimisation of weight and volume, while providing a working vacuum seal. However, these recommendations require the ADCS of the PocketQube to be developed so that the interfaces can be precisely defined. For example, does the motor controller need to include a current sensor or is this part of the ADCS? A different recommendation concerns the motor cable. The combination of O-ring and cable proved to not provide a reliable seal in vacuum. It is recommended to include a cable connector in the structure itself, so that a full O-ring can be used to seal the atmosphere inside. The flywheel material could be changed depending on whether the effect of induced eddy currents can be measured. A complete survey of material options is recommended. Next, 3D printing in aluminium yielded poor quality structures that probably leaked air in vacuum. Either the manufacturing quality should improve, or the structure must be created using conventional techniques. Apart from this, the flywheel dimensions were manufactured accounting for the uncertainty in the motor dimensions, but

the width of the motor was at the lowest end of the uncertainty band so the flywheel was 0.2 [mm] too large. It is recommended in the future to first measure the motor accurately, and then manufacture the flywheel to fit precisely on the rotor to reduce the mass imbalance.

So far the integration process of the wheels was performed manually. As a result the flywheel was not aligned perfectly. The possibility of using robots or special tools for this task should be investigated.

In terms of testing, additional vibration testing is required to identify the cause of the observed minor damage to the flywheel. The radial direction test was performed after the axial direction test on the same motor with flywheel. Since it could have been damaged in the first test, which was exacerbated in the second, the tests should be performed independently, and in more stages. This should be followed by long-term motor tests to assess the motor's lifetime performance. Furthermore, thermal vacuum tests of the complete RWA are recommended, once a suitable vacuum-proof design is found. Microvibration tests were limited by time constraints, so additional measurements can be performed to further validate test results. Furthermore, suggestions for improving the test bench include using a single high stiffness suspension wire and measuring with two accelerometers instead of one. Most importantly, the wheel should be mounted securely on the seismic mass, which was not possible because of the small screw diameter.

VI

Appendices

A

Overview small reaction wheels

Table A.1: Overview of COTS Reaction wheels

Reaction wheel	RWP015 Blue Canyon Technologies [3]	GSW-600 GOMspace [5]	CubeWheel small CubeSpace [4]	RW210 Hyperion Technologies [6]	RW1B Astro-und Feinwerktechnik Adlershof GmbH [2]
Max. Torque [mNm]	4	2	0.23	1.5	-
Peak Power [W]	5.5	1.76	1	1	0.32
Mass [g]	130	47	90	12	90
Size [mm^3]	43x43x18	44x44x27	28x28x21	25x25x15	21x21x12

B

Requirements traceability matrix

Requirement traceability matrix							
TOP LEVEL		SYSTEM LEVEL			COMPONENT LEVEL		
Identifier	**Functional requirements**	**Parent**	**Identifier**	**Performance requirements**	**Parent**	**Identifier**	**Motor requirements**
F1	The RW shall be able to generate torque around its rotation axis.	F2	RW-PE1	The RW shall be able to store at least 1*10^-4 Nms angular momentum about its rotation axis in one direction of rotation.	RW-PE7	COM-MR1	The motor shall have a nominal power consumption of 12 [mW].
F1.1	The RW shall be able to accelerate/decelerate to counter disturbances.	F1	RW-PE2	The RW shall be able to generate at least 2.93*10^-3 Nm of torque around its rotation axis over its operational speed range.	RW-PE5	COM-MR2	The motor shall have rotor position sensors.
F1.2	The RW shall be able to accelerate/decelerate at the required rate over its operational speed range.	M4	RW-PE3	The RW shall not generate instantaneous disturbance torques larger than 0.0041 [Nm].	RW-PH3	COM-MR3	The motor shall have a mass below 1 [g].
F2	The RW shall be able to store angular momentum around its rotation axis.	M4	RW-PE4	The RW shall not have a momentum error of larger than 0.134*10^-7 [Nms] Nms over half an orbit. Equivalent: the RW shall control its speed to within at least 300 [rpm] of the desired value.	RW-PH1	COM-MR4	The motor shall have a maximum speed as high as possible.
F2.1	The RW shall be able to counter the total disturbance momentum over one orbit.	F2 M4	RW-PE5	The RW shall be able to determine its rotation speed to within 10 [rpm].	RW-E1	COM-MR5	The motor shall operate between -15 and 45 degrees celsius
F2.2	The RW shall be able to control its speed.	M2	RW-PE6	The RW shall have a nominal power consumption of 15 [mW].	RW-PH4	COM-MR6	The motor shall have maximum dimensions of 14x14x7.5 [mm].
F2.3	The RW shall be able to determine its rotation speed.	M3	RW-PE7	The RW shall have a lifetime in space of at least one year.	RW-PE2	COM-MR7	The motor shall have a linear torque-velocity curve.
					RW-I1	COM-MR8	The motor shall operate at 3.3 [V].
					RW-E4	COM-MR9	The motor shall survive launch accelerations of 7.156 [g] (RMS)
					RW-PE8	COM-MR10	The motor shall have a lifetime of at least 1 year
	Mission requirements			**Physical requirements**			**Flywheel requirements**
M1	The RW shall survive the PocketQube operational environments.	M1	RW-PH1	The housing shall provide structural support for the motor and flywheel.	RW-PH4	COM-FW1	The flywheel shall have a maximum diameter of 14 [mm].
M2	The RW shall be able to operate within PocketQube constraints.	M1	RW-PH2	The housing shall contain an airtight sealed environment with 1 atmosphere pressure.	RW-PE1	COM-FW2	The flywheel shall have a thickness such that it has a moment of inertia of 0.877 [gcm^2]
M3	The RW shall have a lifetime of 1 year.	M2	RW-PH3	The RW shall weigh less than 8g.	RW-PH1	COM-FW3	The flywheel shall be glued to the rotor of the motor.
		M2	RW-PH4	The RW shall ideally measure less than 14x14x8 [mm], but for a first design it shall measure less than 20x20x12 [mm].	RW-PH3	COM-FW4	The flywheel shall be manufactured out of bronze (rho= 8950 kg/m^3] with a precision of better than 0.1 [mm].
		M2	RW-PH5	The RW shall have an eigenfrequency above 60 [Hz]			
				Environmental requirements			**Housing requirements**
		M1	RW-E1	The RW shall be able to operate between -15 and 45 degrees [celsius]	RW-I2	COM-HO1	The housing shall provide structural support for the motor and flywheel, and interface with the 3-wheel assembly structurally.
		M1	RW-E2	The RW shall be able to operate in vacuum.	RW-PH2 RW-E2	COM-HO2	The housing shall have an airtight seal and 1 atmosphere internal pressure
		M1	RW-E3	The RW shall be able to withstand the radiation environment in Low Earth Orbit.	RW-E4	COM-HO3	The housing shall survive random vibrations of 7.156 [g] (RMS) during launch.

		M1	RW-E4	The RW shall be able to survive random vibrations during launch with a root mean square value of 7.2 [g] and sine vibrations of up to 2 [g].	RW-E4	COM-HO4	The housing shall survive sine vibrations of 2 [g] max. during launch.
					RW-PH3	COM-HO5	The housing shall ideally have a mass of less than 3g, but for a first design it shall weigh less than 6 [g]
					RW-E3 RW-I3	COM-HO6	The housing shall be made out of aluminum.
					RW-PH5	COM-HO7	The housing shall have an eigenfrequency of more than 200 [Hz].
				Interface requirements			**Control electronics requirements**
		M2	RW-I1	The RW shall operate with the bus voltage of 3.3 [V].	RW-PE7	COM-CE1	The control electronics board shall control the motor using Pulse-width modulation.
		M2	RW-I2	The RW shall have a structural interface with the ADCS system.	RW-PE7	COM-CE2	The control electronics board shall have a power consumption of less than 10 [mW].
		M2	RW-I3	The RW shall not generate electromagnetic disturbances that interfere with other subsystems.	RW-PE4	COM-CE3	The control electronics shall be able to control the motor speed to at least within 300 [RPM].
					RW-PH4	COM-CE4	The board shall have dimensions of less than 14x14x2 [mm].
					RW-PH3	COM-CE5	The board shall have a mass of less than 1 [g].

Figure B.1: Requirements traceability matrix

C

Motor manufacturers

The motor manufacturers which were included in the search for suitable DC and BLDC motors are listed here. The most relevant ones are written in bold font.

- **Maxon**
- **Faulhaber**
- **Moog**
- **Namiki**
- **Premotec**
- **Portescap**
- **Precision micro-drives**
- **Nimebea**
- **Micro flierradio**
- **Aveox**
- **Jinlong**
- **Transmotec**
- Hsiang Neng
- Pittman
- Fulling
- Rotero
- Johnson Electric
- Metmotors
- Oriental Motors
- Crouzet Motors
- Goldenmotor
- Baldor
- Allied motion
- Nidec
- Electrocraft
- Dunkermotoren
- Nanotec
- Printed motor works
- Molon
- Shezhen Hotec
- Haydon
- Kag
- Bison
- PML
- Micro gearmotors
- Rotalink
- Infineon
- Sinotech
- Delta
- Granger
- Ebm-papst
- Acme fan
- Bodine electric
- Nanmotion
- Mechtex
- Anaheim
- Weg
- ISL
- Copal electronics
- Cramer Co
- CNI Inc
- PMPM
- OMRON
- Panasonic industrial
- TE connectivity
- Trinamic
- ABB
- Advanced motion controls
- Bartec
- Bauer
- Beckhoff
- Bergerluhr
- Bonfiglioli
- Brock COmpton
- SEW Eurodrive
- Gefeg-Neckar
- Focquet
- Curtis-Wright
- Marathon
- Creusen
- Merkle-korff
- Omec
- Mavilor
- Lin engineering
- Parvex
- Telcomotion
- Assun motor
- Canon USA
- Celeroton
- Citizen micro
- Dagu
- Rotek
- Ziehl-ABEGG

D

Test setup details

D.1. Functional test

The purpose of the test is to create characteristic plots of the motor such as Speed vs Time, Torque vs Time, Torque vs Power, Current vs Time and to verify the motor datasheet parameters. Because of some practical limitations discussed in Appendix D.1 it was not possible to produce the Torque vs Power plots.

Measurement limitations

Phase current, dynamic phase voltages and direct torque measurements were not possible due to practical limitations.

In the EPOS software only the DC current is measured. External measurement of phase currents using a current probe was not possible. Therefore, it was decided to measure the voltage waveforms instead. The EPOS controller chops a 10 [V] supply voltage with unknown duty cycle and so the voltage is not directly known. At any given moment current flows in 2 phases, with the back EMF being induced in the third. Therefore, to measure the actual supply voltage (after PWM modulation) the potential difference between the two active phases is the supply voltage, and the third phase should be ignored. The separate parts can easily identified at high speeds, but at speeds below about 2000 [RPM] this becomes difficult. Furthermore, many separate measurements (16 per motor per set speed) are required to obtain a reasonable random uncertainty. In the maximum acceleration scenario necessary to determine the motor constants this is not possible, as over 16 rotations the motor accelerates to another velocity. Therefore, only the steady-state power consumption can be determined.

The torque can only be obtained indirectly by taking the derivative of the speed curve. This means that the starting torque is not accurately measured, as the rotor doesn't respond immediately due to its inertia. However, since the torque constant can be determined from the velocity constant instead this is not problematic.

Test hardware

The functional tests of the motor and motor with flywheel are performed with the test setup shown in Figure 8.1. The required hardware for the test is:

- PC with EPOS software installed
- Control board EPOS 24/2
- Connector cables
- Maxon EC10FL
- Power supply 9-24V
- Multi-meter

- PicoScope
- three voltage probes

Test parameters

The independent variable is the set speed which is specified in the EPOS software interface. The dependent variables are the measured rotation speed, DC current and phase voltages. The supply voltage is the controlled variable in the test. The motor and winding temperature are also dependent variables, but they are not measured. However, their effect is included in the random variations of the measurement by testing on timescales that include random variations. The ambient conditions are uncontrolled variables, however tests are all performed at 25 degree ambient temperature. Further random variations are control inaccuracies, random variations in the friction torque due to for example parasitic vibrations, power supply instabilities and disturbing magnetic fields. The time scales of the measurements are taken as large enough to include these effects.

The motor speed and DC current are measured using the EPOS software data acquisition function. The controller calculates the rotation speed from the the Hall sensor signals. Current is measured with a 0-4 [A] 12 bit current sensor giving a resolution of about 1 [mA].

Because the controller is chopping 10 [V] to deliver the supply voltage to the motor it is not straightforward to determine the voltage supplied to the motor at a given moment. Instead, the voltage is established by measuring the three phase voltages. At any moment the current is flowing through two out of the three windings. Over three electrical periods the voltage in one winding is shown in Figure D.1. Per electrical period, for 1/3rd of the time, the winding is not carrying the supply current, but a current is induced due to the motion of the rotor. This part of the voltage has to be ignored. Instead, the sum of the voltage across the other two phases corresponds to the supply voltage in that particular winding. Overall, 16 such measurements, per set speed are performed to obtain a reasonable random uncertainty.

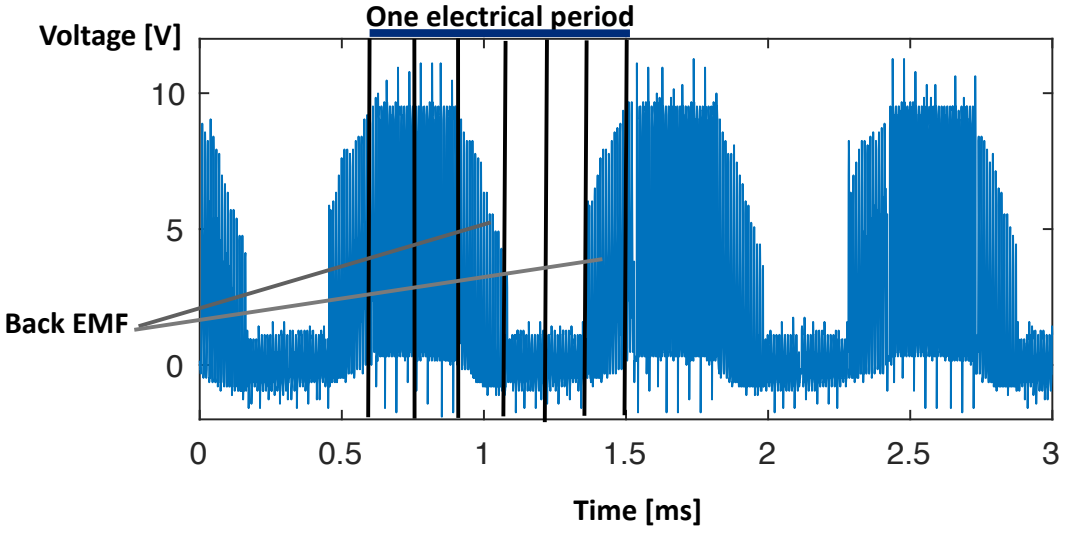

Figure D.1: Voltage in one phase over three electrical periods

Uncertainty analysis

The uncertainty analysis of the functional tests of both the motor and the complete reaction wheel is presented here. The equations are taken from the text book 'Experimentation, Validation, and Uncertainty Analysis for engineers' [13]. The parameters that are measured are the DC current, motor speed and phase voltages. Their systematic, random and finally combined uncertainties are derived in the following sections.

Systematic uncertainties

The systematic uncertainty in the speed, current, and voltage measurements is discussed after which equations to propagate systematic uncertainties are derived.

Both measurements are performed using the EPOS software interface. The speed measurement is based on averaging the speed calculated from hall sensor signals. No information is available about the systematic uncertainty of the measurement. Attempts to validate the measurement by measuring the electrical periods of the voltage waveforms proved unsuccessful due to large random uncertainties. Therefore the systematic uncertainty is estimated as 0.1 %, which is about 10% of the control error. The current measurement is performed with a 12 bit 0-4 [A] current sensor and therefore the systematic uncertainty is $\frac{4}{2^{12}} \approx 1$ [mA].

The voltage is measured by inspection of the voltage waveforms using a PicoScope. The average voltage over a period is determined by setting bars in the interface according to the waveform period (see Figure D.1. The PicoScope has a measurement uncertainty of three%. The voltage probes have an uncertainty in their resistance of two%, which is assumed to translate into a measurement uncertainty of two%. The combined uncertainty of the voltage measurement is given by Equation (D.1).

$$b_V = \left| \sum_{k=1}^{M} (b_k)^2 \right|^{\frac{1}{2}} = (b_{scope}^2 + b_{probe}^2)^{\frac{1}{2}} = 0.036\% \tag{D.1}$$

For values that are calculated using multiple measured parameters the systematic uncertainties are propagated separately, before being combined with the random uncertainty. The formulas are based on Equation (D.2), where $x_1 \cdots x_j$ are the measured parameters and f is the function that is used to calculate the desired value, for which b_R is the total systematic uncertainty. The measurements are assumed to be uncorrelated.

$$b_R = \left| \left(\frac{\delta f}{\delta x_1}\right)^2 \times b_{x_1}^2 + \left(\frac{\delta f}{\delta x_2}\right)^2 \times b_{x_2}^2 \cdots \left(\frac{\delta f}{\delta x_j}\right)^2 \times b_{x_j}^2 \right|^{\frac{1}{2}} \tag{D.2}$$

The motor constants can all be calculated using the back EMF constant using Equation (D.3). Its systematic uncertainty is given by Equation (D.4). Similar equations can be derived for the speed and torque constant.

$$k_B = \frac{V - i \times R}{\omega} \tag{D.3}$$

$$b_{k_B} = \left| \left(\frac{1}{\omega}\right)^2 \times b_V^2 + \left(\frac{V - i \times R}{-\omega^2}\right)^2 \times b_\omega^2 + \left(\frac{-R}{\omega}\right)^2 \times b_i^2 \right|^{\frac{1}{2}} \tag{D.4}$$

The friction torque is calculated from the torque constant using Equation (D.5). To keep the calculations simple the combined systematic uncertainty of the torque constant is propagated in Equation (D.6), instead of propagating the individual contributions.

$$T_{fr} = K_T \times i \tag{D.5}$$

$$b_{T_{fr}} = \left| \left(K_T\right)^2 \times b_i^2 + \left(i\right)^2 \times b_{T_K}^2 \right|^{\frac{1}{2}} \tag{D.6}$$

Finally, the power consumption and friction loss are calculated using Equation (D.7) and Equation (D.8).

$$P = V \times i \tag{D.7}$$

$$P_{fr} = T_{fr} \times V \tag{D.8}$$

The associated systematic uncertainties are calculated using Equation (D.9) and Equation (D.10).

$$b_P = \left| \left(V\right)^2 \times b_i^2 + \left(i\right)^2 \times b_V^2 \right|^{\frac{1}{2}} \tag{D.9}$$

$$b_{P_{fr}} = \left| \left(T_{fr}\right)^2 \times b_V^2 + \left(V\right)^2 \times b_{T_{fr}}^2 \right|^{\frac{1}{2}} \tag{D.10}$$

Random uncertainties

Random uncertainties of the measurement are calculated as standard uncertainties using Equation (D.11). They are computed for each measurement of speed, current and voltage at each set speed, both for the motor and the reaction wheel. The values for each set speed are then separately combined with the systematic uncertainty. M is the number of measurements, $\bar{r}$ is the average and r_k the specific measurement.

$$S_R^2 = \frac{1}{M-1} \sum_{k=1}^{M} (r_k - \bar{r})^2 \tag{D.11}$$

For values that are calculated using the measured parameters the total random uncertainty is calculated directly without including the individual standard uncertainties using Equation (D.12). This method automatically takes into account correlations between the variables that might otherwise be hidden.

$$S_T = \frac{1}{\sqrt{M}} \left| \frac{1}{M-1} \sum_{k=1}^{M} (r_k - \bar{r})^2 \right|^{\frac{1}{2}} \tag{D.12}$$

Combined uncertainty

The systematic and random uncertainties for each measurement are combined and expanded for a 95% confidence interval using Equation (D.13) or Equation (D.14). N is the number of measurements and t_{95} is a factor that expands the uncertainty, which is determined by the number of measurements and the assumption of a normally distributed parent population.

$$U_{95} = t_{95} \times \left(\frac{S_R^2}{N} + b_R^2 \right)^{\frac{1}{2}} \tag{D.13}$$

$$U_{95} = t_{95} \times \left(S_T^2 + b_R^2 \right)^{\frac{1}{2}} \tag{D.14}$$

D.2. Vibration test

The details of the vibration test are described in this section.

Test setup

The test setup is shown in Figure D.4. A picture of the reaction wheel mounted in sideways configuration is shown in Figure D.3. A signal generator is used to produce the required sine input signals. The random signal is generated in Matlab and sent to a power amplifier using a custom built Audio Jack to BNC coax cable. The accelerations on the shaker - RW interface are measured with an accelerometer that is read using a PicoScope. The data is then processed in Matlab. However, no closed loop system is implemented. Instead, the gain of the amplifier is continuously adapted manually to the real-time root mean square acceleration value. For a 120s interval 6 measurements of the root mean square acceleration are averaged to measure changes in the load level.

Qualification loads

Qualification envelopes for different launchers are shown in Figure D.5. At first the RW will be qualified for PSLV sine vibrations and DNEPR random vibrations. The NanoRacks qualification loads are larger, the qualification can be extended should this prove necessary. Dwell times per frequency band are typically indicated on a log scale as octave per minute; one octave higher corresponds to doubling the frequency. The dwell times for the sine vibration tests are 2 octaves/minute as per PSLV requirements [8]. The random vibrations will be tested for 120 [s], which is representative of the real launch environment.

Input signal

The input random noise signal is matched to the structural properties of the shaker and interface by first finding the shaker eigenmodes. The input (random noise 0-2 [kHz]) and output are shown in Figure D.2. The shaker has clear eigenmodes at around 200 [Hz], 620 [Hz] and 2600 [Hz]. At the lower two frequencies a bandstop filter is applied to the input signal. This results in a waveform closely resembling the target envelope. The adjusted input signal and shaker response can be seen in Figure 11.6.

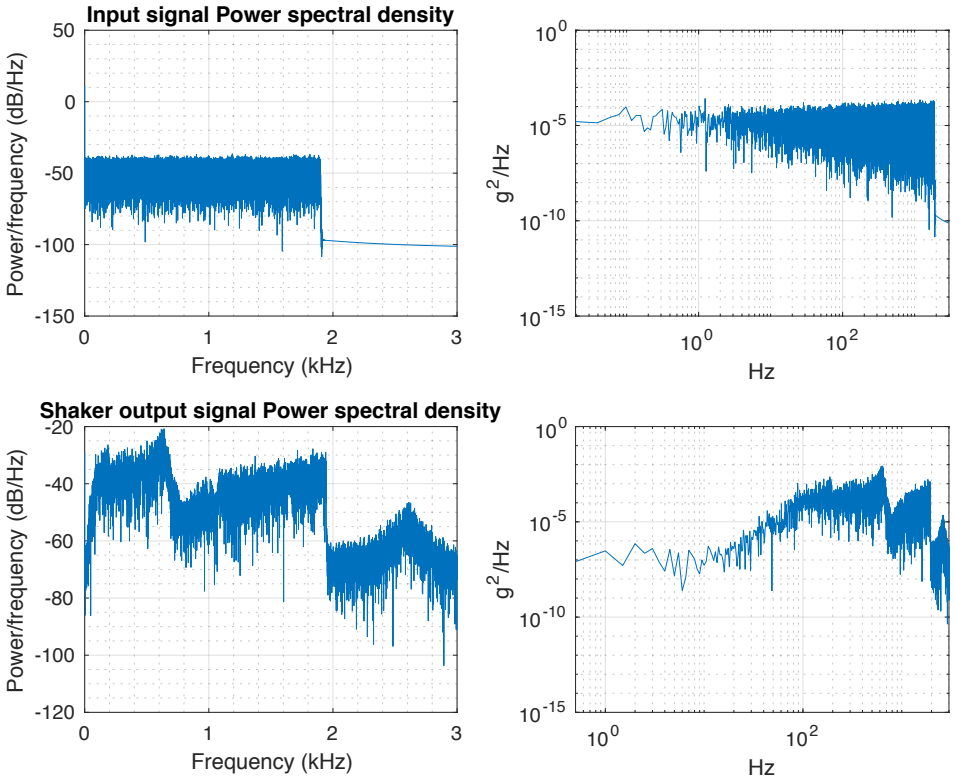

Figure D.2: Shaker input signal and response

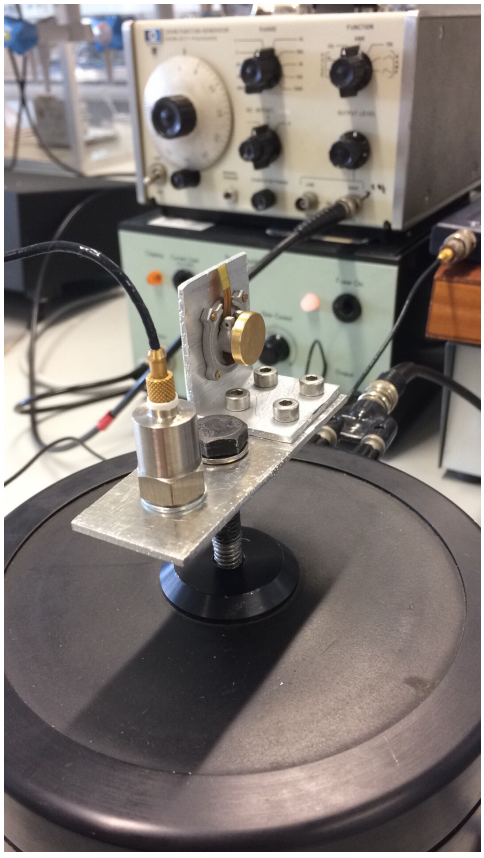

Figure D.3: Reaction wheel mounted on shaker for radial test

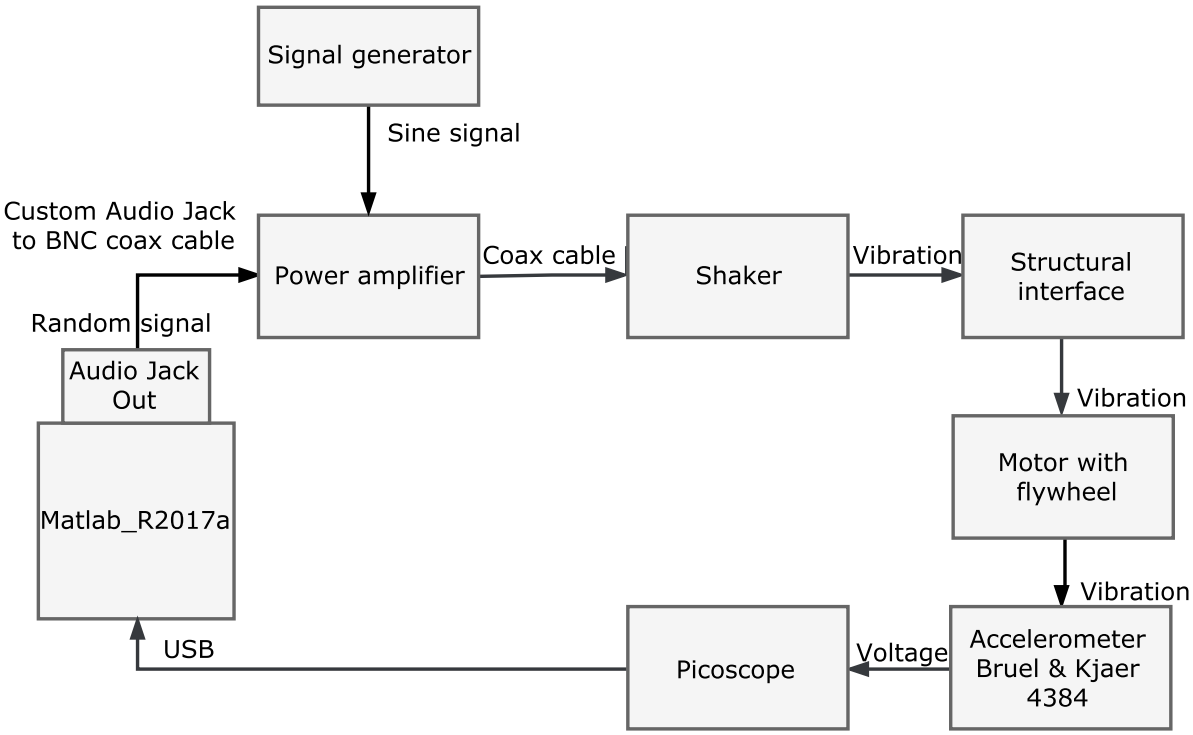

Figure D.4: Vibration test

Table D.1: Vibration test procedure

Step	Signal type	Frequency [Hz]	Load [g]	Duration [s]
1.	Sine sweep	0-800	0.5	-
2.	Sine	5-20	1	60
3.	Sine	20-40	3	60
4.	Sine	40-100	0.8	60
5.	Sine sweep	0-800	0.5	-
6.	Random	0-2000	3	120
7.	Sine sweep	0-800	0.5	-
8	Random	0-2000	7.2	120
9.	Sine sweep	0-800	0.5	-

Test procedures

The test procedures and qualification levels are summarised in Table D.1. First, a sine sweep is performed to identify the eigenfrequencies of the reaction wheel, after which the sine loads are applied. Another sine sweep is done to identify changes in the wheel's structural properties, which would indicate a failure. The random vibration tests are done in two steps with sine sweeps in between and after. Finally, a functional test is performed to quantify the wheel's performance after vibration testing.

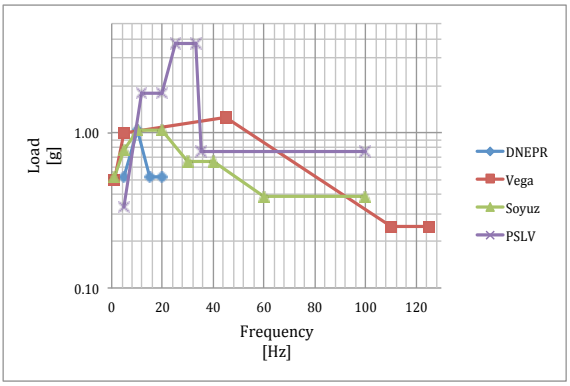

(a) Sine vibration envelope

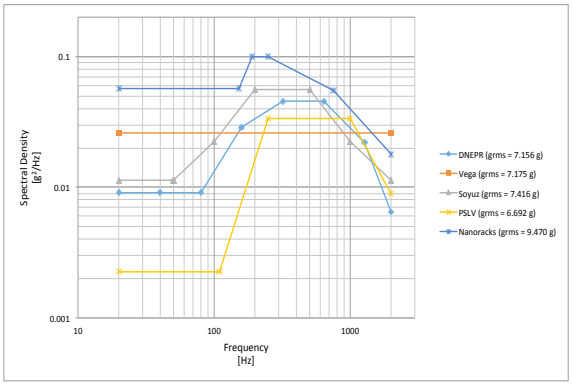

(b) Random vibration envelope

Figure D.5: Launch loads for different launch vehicles [8]

Data processing

The test data is produced in the form of measured voltages over time. The following Matlab code is used to generate Power Spectral Density plots for a single time series.

Creating input signal

The input signal is generated using the following matlab code.

```
close all
clear all

\%\% Create filters
\%Lowpass filter at 2 [kHz]
d1 = designfilt('lowpassiir', 'PassbandFrequency', 475, ...
    'StopbandFrequency', 500, 'PassbandRipple', 1, ...
    'StopbandAttenuation', 200, 'SampleRate', 2000, ...
    'DesignMethod', 'cheby1', 'MatchExactly', 'stopband');
\%Passband filter at 180 [Hz]
d2 = designfilt('bandstopiir','FilterOrder',20, ...
         'HalfPowerFrequency1',85,'HalfPowerFrequency2',140, ...
         'SampleRate',1500);
\%Passband filter at 600 [Hz]
d3 = designfilt('bandstopiir','FilterOrder',20, ...
         'HalfPowerFrequency1',295,'HalfPowerFrequency2',400, ...
         'SampleRate',1500);

\%\% Create random noise
N = 4096;
Nsamples = 100;
noise = rand(N*Nsamples,1);

\%\% Filter random noise
noisef1 = filter(d1,noise);
noisef2 = filter(d2test,noisef1);
noisef3 = filter(d3,noisef2);

\%\% Output noise
sound(noisef3);

\%\% Inspect noise in PSD plot
subplot(2,1,1)
plot(psd(spectrum.periodogram,noisef3,'Fs',8000,'NFFT',length(noisef3)));
```

```
xlim([0 3]); grid on; grid minor
ylim([-100 -30])
title('Input signal Power spectral density')

subplot(2,1,2)
psdest = psd(spectrum.periodogram,noisef3,'Fs',8000,'NFFT',length(noisef3));
loglog(psdest.Frequencies, psdest.Data); grid on
xlim([0 3000])
ylabel('g^2/Hz');
ylim([-10^1, 3*10^0])
xlabel('Hz');
```

Analysing test data

```
close all
clear all

\%\% import data
ximport = importdata('time_series.txt');
xdata = ximport.data;
t0 = xdata(:,1);

\%\% convert voltage to acceleration and compute time-domain RMS acceleration
\%\% accelerometer sensitivity is 8.04 mV/g
x0 = xdata(:,2)/1000/0.00804;

\%\% compute time-domain rms acceleration and sampling frequency
trms = rms(x);
Fs = 1/(t1(5)-t1(4))


\%\% Normal PSD plot
subplot(2,1,1)
plot(psd(spectrum.periodogram,x,'Fs',Fs,'NFFT',length(x)))

\%\% Separate frequency and amplitude
psd = psd(spectrum.periodogram,x,'Fs',Fs,'NFFT',length(x));
freq = psd2.Frequencies;
dat2 = psd2.data;
title('Shaker response with RW')
xlim([0 7])
ylim([-100 5])
grid on; grid minor

\%\% log PSD plot
subplot(2,1,2)
loglog(freq, dat); grid on;
ylabel('g^2/Hz');
xlim([0 7000])
xlabel('Hz');
ylim([-100 5])

\%\%compute rms acceleration in frequency domain
area = trapz(freq2,dat2);
grms = mean(sqrt(area))
```

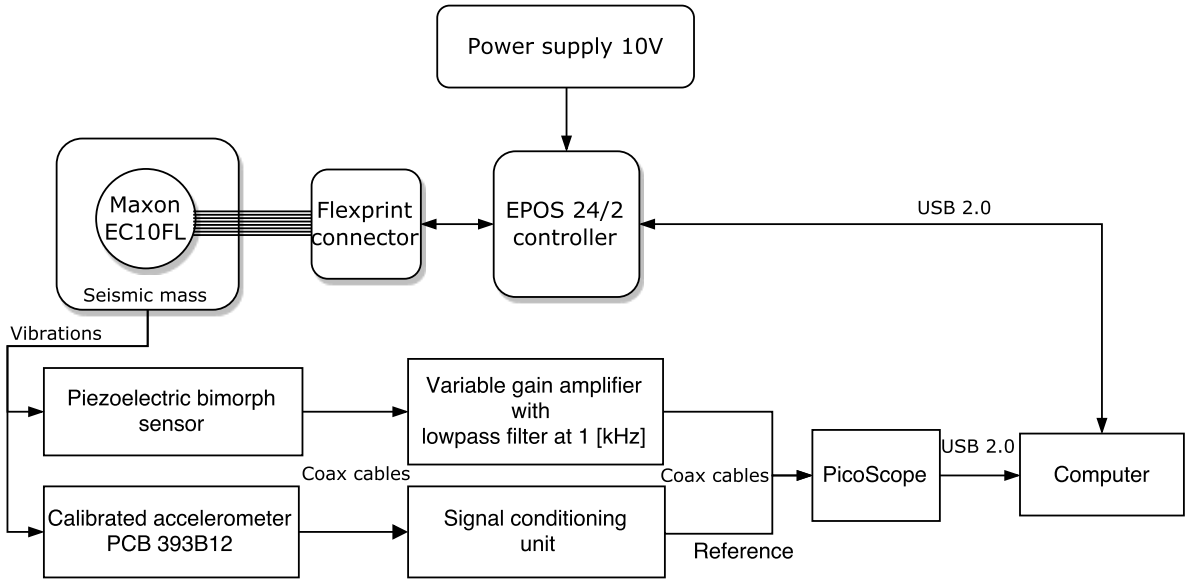

Figure D.6: Test setup micro-vibration tests

D.3. Microvibration test

Details about the test procedures, data processing and uncertainty analysis of the micro-vibration test are presented here.

Test setup

The test setup is shown in Figure D.6 and pictures of the test bench were shown in Section 10.7.

Test procedures

The tests were performed in the physical lab of the faculty of Aerospace Engineering on a passive vibration isolation table.

Initialisation of the test

The accelerometer was connected to the signal conditioning unit which supplies the sensor with power and isolates the acceleration signal. The signal was sent to a PicoScope oscilloscope sampling at 50 [kHz]. The motor is controlled using the EPOS motor controller and software. The accelerometer was screwed into the measurement location on the seismic mass and the background noise was measured. Parasitic vibrations with an amplitude of 10 [mV] and frequency of 50 [Hz] were measured. This is typical measurement noise caused by the power supply. Clearly the vibration isolation is not ideal, which is likely due to the cables connected to the accelerometer and controller. The to be measured signals have an amplitude of more than 1 [V] so this was not problematic.

Test steps

The speed of the wheel was changed in increments of 2000 [RPM] from 0 to 14000 [RPM], which is just above the maximum useful speed of the wheel. The tests were performed with the accelerometer at one location, and then again with the accelerometer at the other location. For each step 10 measurements were performed to improve the random uncertainty and assess the reproducibility of the results. Ideally, two accelerometers are used to calculate the forces and moments, but this was not possible. The random uncertainty of the measurements is a measure of how well the tests can be reproduced.

Data processing

The data obtained is in units of Voltage vs Time. This is converted to units of acceleration and filtered to exclude frequencies above 1 [kHz]. Then the forces and moments are calculated using the equations derived in Section 10.6. The RMS value of each is taken as this accounts for the time history of the signal and in acceleration

measurements is a measure of the overall energy. The accelerations are also processed in the frequency domain to create power spectral density plots. The calculations were performed in Matlab with the code given below.

```
%% Microvib_testprocess
clear all
close all

%% set up test parameters
m_bench = 3.585;
d1 = 140/2/1000;
d2 = d1;
d3 = 140/2/1000;
d4 = d3;
Ixx = 0.015;

%% load test data for each measurement step
% load bottom measurements
numfiles = 8;
cal = 10.36/9.81;

for k = 1:numfiles
  myfilename0 = sprintf('mu_B0_%d.txt', k);
  vib_b0{k} = importdata(myfilename0);
  Tb0(:,k) = vib_b0{k}.data(:,1);
  Ib0(:,k) = vib_b0{k}.data(:,2)/1000/1000/cal;
  myfilename1 = sprintf('mu_B1_%d.txt', k);
  vib_b1{k} = importdata(myfilename1);
  Tb1(:,k) = vib_b1{k}.data(:,1);
  Ib1(:,k) = vib_b1{k}.data(:,2)/1000/cal;
  myfilename2 = sprintf('mu_B2_%d.txt', k);
  vib_b2{k} = importdata(myfilename2);
  Tb2(:,k) = vib_b2{k}.data(:,1);
  Ib2(:,k) = vib_b2{k}.data(:,2)/cal;
  myfilename3 = sprintf('mu_B3_%d.txt', k);
  vib_b3{k} = importdata(myfilename3);
  Tb3(:,k) = vib_b3{k}.data(:,1);
  Ib3(:,k) = vib_b3{k}.data(:,2)/cal;
  myfilename4 = sprintf('mu_B4_%d.txt', k);
  vib_b4{k} = importdata(myfilename4);
  Tb4(:,k) = vib_b4{k}.data(:,1);
  Ib4(:,k) = vib_b4{k}.data(:,2)/cal;
  myfilename5 = sprintf('mu_B5_%d.txt', k);
  vib_b5{k} = importdata(myfilename5);
  Tb5(:,k) = vib_b5{k}.data(:,1);
  Ib5(:,k) = vib_b5{k}.data(:,2)/cal;
  myfilename6 = sprintf('mu_B6_%d.txt', k);
  vib_b6{k} = importdata(myfilename6);
  Tb6(:,k) = vib_b6{k}.data(:,1);
  Ib6(:,k) = vib_b6{k}.data(:,2)/cal;
  myfilename7 = sprintf('mu_B7_%d.txt', k);
  vib_b7{k} = importdata(myfilename7);
  Tb7(:,k) = vib_b7{k}.data(:,1);
  Ib7(:,k) = vib_b7{k}.data(:,2)/cal;
  myfilename8 = sprintf('mu_B8_%d.txt', k);
  vib_b8{k} = importdata(myfilename8);
  Tb8(:,k) = vib_b8{k}.data(:,1);
  Ib8(:,k) = vib_b8{k}.data(:,2)/cal;
```

```
  myfilename9 = sprintf('mu_B9_%d.txt', k);
  vib_b9{k} = importdata(myfilename9);
  Tb9(:,k) = vib_b9{k}.data(:,1);
  Ib9(:,k) = vib_b9{k}.data(:,2)/cal;
  myfilename10 = sprintf('mu_B10_%d.txt', k);
  vib_b10{k} = importdata(myfilename10);
  Tb10(:,k) = vib_b10{k}.data(:,1);
  Ib10(:,k) = vib_b10{k}.data(:,2)/cal;
  myfilename11 = sprintf('mu_B11_%d.txt', k);
  vib_b11{k} = importdata(myfilename11);
  Tb11(:,k) = vib_b11{k}.data(:,1);
  Ib11(:,k) = vib_b11{k}.data(:,2)/cal;
  myfilename12 = sprintf('mu_B12_%d.txt', k);
  vib_b12{k} = importdata(myfilename12);
  Tb12(:,k) = vib_b12{k}.data(:,1);
  Ib12(:,k) = vib_b12{k}.data(:,2)/cal;
  myfilename13 = sprintf('mu_B13_%d.txt', k);
  vib_b13{k} = importdata(myfilename13);
  Tb13(:,k) = vib_b13{k}.data(:,1);
  Ib13(:,k) = vib_b13{k}.data(:,2)/cal;
  myfilename14 = sprintf('mu_B14_%d.txt', k);
  vib_b14{k} = importdata(myfilename14);
  Tb14(:,k) = vib_b14{k}.data(:,1);
  Ib14(:,k) = vib_b14{k}.data(:,2)/cal;
  myfilename15 = sprintf('mu_B15_%d.txt', k);
  vib_b15{k} = importdata(myfilename15);
  Tb15(:,k) = vib_b15{k}.data(:,1);
  Ib15(:,k) = vib_b15{k}.data(:,2)/cal;
end

% load top measurements

for k = 1:numfiles
  myfilename0 = sprintf('mu_T0_%d.txt', k);
  vib_t0{k} = importdata(myfilename0);
  Tt0(1:size(vib_t0{k}.data(:,1)),k) = vib_t0{k}.data(:,1);
  It0(1:size(vib_t0{k}.data(:,2)),k) = vib_t0{k}.data(:,2)/1000/1000/cal;
  myfilename1 = sprintf('mu_T1_%d.txt', k);
  vib_t1{k} = importdata(myfilename1);
  Tt1(1:size(vib_t1{k}.data(:,1)),k) = vib_t1{k}.data(:,1);
  It1(1:size(vib_t1{k}.data(:,2)),k) = vib_t1{k}.data(:,2)/1000/cal;
  myfilename2 = sprintf('mu_T2_%d.txt', k);
  vib_t2{k} = importdata(myfilename2);
  Tt2(1:size(vib_t2{k}.data(:,1)),k) = vib_t2{k}.data(:,1);
  It2(1:size(vib_t2{k}.data(:,2)),k) = vib_t2{k}.data(:,2)/1000/cal;
  myfilename3 = sprintf('mu_T3_%d.txt', k);
  vib_t3{k} = importdata(myfilename3);
  Tt3(1:size(vib_t3{k}.data(:,1)),k) = vib_t3{k}.data(:,1);
  It3(1:size(vib_t3{k}.data(:,2)),k) = vib_t3{k}.data(:,2)/cal;
  myfilename4 = sprintf('mu_T4_%d.txt', k);
  vib_t4{k} = importdata(myfilename4);
  Tt4(1:size(vib_t4{k}.data(:,1)),k) = vib_t4{k}.data(:,1);
  It4(1:size(vib_t4{k}.data(:,2)),k) = vib_t4{k}.data(:,2)/cal;
  myfilename5 = sprintf('mu_T5_%d.txt', k);
  vib_t5{k} = importdata(myfilename5);
  Tt5(1:size(vib_t5{k}.data(:,1)),k) = vib_t5{k}.data(:,1);
```

```
  It5(1:size(vib_t5{k}.data(:,2)),k) = vib_t5{k}.data(:,2)/cal;
  myfilename6 = sprintf('mu_T6_%d.txt', k);
  vib_t6{k} = importdata(myfilename6);
  Tt6(1:size(vib_t6{k}.data(:,1)),k) = vib_t6{k}.data(:,1);
  It6(1:size(vib_t6{k}.data(:,2)),k) = vib_t6{k}.data(:,2)/cal;
  myfilename7 = sprintf('mu_T7_%d.txt', k);
  vib_t7{k} = importdata(myfilename7);
  Tt7(1:size(vib_t7{k}.data(:,1)),k) = vib_t7{k}.data(:,1);
  It7(1:size(vib_t7{k}.data(:,2)),k) = vib_t7{k}.data(:,2)/cal;
  myfilename8 = sprintf('mu_T8_%d.txt', k);
  vib_t8{k} = importdata(myfilename8);
  Tt8(1:size(vib_t8{k}.data(:,1)),k) = vib_t8{k}.data(:,1);
  It8(1:size(vib_t8{k}.data(:,2)),k) = vib_t8{k}.data(:,2)/cal;
  myfilename9 = sprintf('mu_T9_%d.txt', k);
  vib_t9{k} = importdata(myfilename9);
  Tt9(1:size(vib_t9{k}.data(:,1)),k) = vib_t9{k}.data(:,1);
  It9(1:size(vib_t9{k}.data(:,2)),k) = vib_t9{k}.data(:,2)/cal;
  myfilename10 = sprintf('mu_T10_%d.txt', k);
  vib_t10{k} = importdata(myfilename10);
  Tt10(1:size(vib_t10{k}.data(:,1)),k) = vib_t10{k}.data(:,1);
  It10(1:size(vib_t10{k}.data(:,2)),k) = vib_t10{k}.data(:,2)/cal;
  myfilename11 = sprintf('mu_T11_%d.txt', k);
  vib_t11{k} = importdata(myfilename11);
  Tt11(1:size(vib_t11{k}.data(:,1)),k) = vib_t11{k}.data(:,1);
  It11(1:size(vib_t11{k}.data(:,2)),k) = vib_t11{k}.data(:,2)/cal;
  myfilename12 = sprintf('mu_T12_%d.txt', k);
  vib_t12{k} = importdata(myfilename12);
  Tt12(1:size(vib_t12{k}.data(:,1)),k) = vib_t12{k}.data(:,1);
  It12(1:size(vib_t12{k}.data(:,2)),k) = vib_t12{k}.data(:,2)/cal;
  myfilename13 = sprintf('mu_T13_%d.txt', k);
  vib_t13{k} = importdata(myfilename13);
  Tt13(1:size(vib_t13{k}.data(:,1)),k) = vib_t13{k}.data(:,1);
  It13(1:size(vib_t13{k}.data(:,2)),k) = vib_t13{k}.data(:,2)/cal;
  myfilename14 = sprintf('mu_T14_%d.txt', k);
  vib_t14{k} = importdata(myfilename14);
  Tt14(1:size(vib_t14{k}.data(:,1)),k) = vib_t14{k}.data(:,1);
  It14(1:size(vib_t14{k}.data(:,2)),k) = vib_t14{k}.data(:,2)/cal;
  myfilename15 = sprintf('mu_T15_%d.txt', k);
  vib_t15{k} = importdata(myfilename15);
  Tt15(1:size(vib_t15{k}.data(:,1)),k) = vib_t15{k}.data(:,1);
  It15(1:size(vib_t15{k}.data(:,2)),k) = vib_t15{k}.data(:,2)/cal;
end


%% Filter all data
ab = [Ib0 Ib1 Ib2 Ib3 Ib4 Ib5 Ib6 Ib7 Ib8 Ib9 Ib10 Ib11 Ib12 Ib13 Ib14 Ib15];
abT = [Tb0 Tb1 Tb2 Tb3 Tb4 Tb5 Tb6 Tb7 Tb8 Tb9 Tb10 Tb11 Tb12 Tb13 Tb14 Tb15];
at = [It0 It1 It2 It3 It4 It5 It6 It7 It8 It9 It10 It11 It12 It13 It14 It15];
atT = [Tt0 Tt1 Tt2 Tt3 Tt4 Tt5 Tt6 Tt7 Tt8 Tt9 Tt10 Tt11 Tt12 Tt13 Tt14 Tt15];

%doublecheck sample rates
for j = 1 : size(ab,2)
    Fsa(j) = 1/(abT(100,j)-abT(99,j));
    Fsb(j) = 1/(atT(100,j)-atT(99,j));
end
```

```
%if all the same
Fs = Fsa(1);
N  = 200;
Fp  = 1e3;
Ap  = 0.01;
Ast = 80;

% set up filter
lowpassFilt = dsp.LowpassFilter('DesignForMinimumOrder',false, ...
    'FilterOrder',N,'PassbandFrequency',Fp,'SampleRate',Fs,...
    'PassbandRipple',0.01, 'StopbandAttenuation',80);

low_1000 = designfilt('lowpassiir', 'PassbandFrequency', 1000, ...
    'StopbandFrequency', 1200, 'PassbandRipple', 1, ...
    'StopbandAttenuation', 200, 'SampleRate', Fs, ...
    'DesignMethod', 'cheby1', 'MatchExactly', 'stopband');

ab = lowpassFilt(ab);
at = lowpassFilt(at);
% fvtool(low_1000)

%% Inspect ab and at to check the signals are in phase;
% if they are the measurements taken at separate moments can be combined
figure
plot(Tt2, ab(:,10*8+2))
hold on
plot(Tt2, at(:,10*8+2))
legend('show')
legend('bottom a1', 'top a2')
%% Computes Fy and Mx

A = m_bench*d2/(d1+d2);
B = m_bench*d1/(d1+d2);
C = (Ixx-m_bench*d2^2)/(d1+d2);
D = (-Ixx-m_bench*d1*d2)/(d1+d2);

for i = 1:size(ab,2)
    for k = 1: size(ab,1)-100
        F(k,i) = A*ab(k,i)+B*at(k,i);
        M(k,i) = C*ab(k,i)+D*at(k,i);
%         Mm(k,i) = Ixx/(d1+d2)*ab(k,i)-Ixx/(d1+d2)*at(k,i);
    end
end


Fyy = rms(F);
% Mm = rms(Mm);
Mx = rms(M);
abrms = rms(ab);
atrms = rms(at);

% separate measurements
for i = 1:16
    Fy(1,i) = Fyy(numfiles*(i-1)+1);
    Fy(2,i) = Fyy(numfiles*(i-1)+2);
    Fy(3,i) = Fyy(numfiles*(i-1)+3);
```

```
    Fy(4,i) = Fyy(numfiles*(i-1)+4);
    Fy(5,i) = Fyy(numfiles*(i-1)+5);
    Fy(6,i) = Fyy(numfiles*(i-1)+6);
    Fy(7,i) = Fyy(numfiles*(i-1)+7);
    Fy(8,i) = Fyy(numfiles*(i-1)+8);

    Mxx(1,i) = Mx(numfiles*(i-1)+1);
    Mxx(2,i) = Mx(numfiles*(i-1)+2);
    Mxx(3,i) = Mx(numfiles*(i-1)+3);
    Mxx(4,i) = Mx(numfiles*(i-1)+4);
    Mxx(5,i) = Mx(numfiles*(i-1)+5);
    Mxx(6,i) = Mx(numfiles*(i-1)+6);
    Mxx(7,i) = Mx(numfiles*(i-1)+7);
    Mxx(8,i) = Mx(numfiles*(i-1)+8);

    a1(1,i) = abrms(numfiles*(i-1)+1);
    a1(2,i) = abrms(numfiles*(i-1)+2);
    a1(3,i) = abrms(numfiles*(i-1)+3);
    a1(4,i) = abrms(numfiles*(i-1)+4);
    a1(5,i) = abrms(numfiles*(i-1)+5);
    a1(6,i) = abrms(numfiles*(i-1)+6);
    a1(7,i) = abrms(numfiles*(i-1)+7);
    a1(8,i) = abrms(numfiles*(i-1)+8);

    a2(1,i) = atrms(numfiles*(i-1)+1);
    a2(2,i) = atrms(numfiles*(i-1)+2);
    a2(3,i) = atrms(numfiles*(i-1)+3);
    a2(4,i) = atrms(numfiles*(i-1)+4);
    a2(5,i) = atrms(numfiles*(i-1)+5);
    a2(6,i) = atrms(numfiles*(i-1)+6);
    a2(7,i) = atrms(numfiles*(i-1)+7);
    a2(8,i) = atrms(numfiles*(i-1)+8);

end

%% Uncertainty analysis
%Random uncertainty
rand_Fy = std(Fy);
rand_Mx = std(Mxx);

mean_Fy = mean(Fy);
mean_Mx = mean(Mxx);

mean_a1 = mean(a1);
mean_a2 = mean(a2);

%Systematic uncertainty
bm = 0.0005;     % [kg]
bm = bm/m_bench;% [% of 1]
ba = 0.03;       % [% of 1]
bd = 0.001;      % [m]
bd = bd/d1;      % [% of 1]
bI = 0.01;       % [% of 1]

%Uncertainties in percentage of 1
bFy = ((0.5*mean_a1+0.5*mean_a2).^2.*bm^2+0.5*m_bench^2*ba^2).^0.5;
```

```
bMx = (((mean_a1-mean_a2)/2/d1).^2*bI^2+(0.5*(Ixx*(mean_a2-mean_a1)/d1^2)+m_bench*(mean_a1
    + ((Ixx+m_bench*d1^2)/2/d1).^2*ba^2+(m_bench*d1/2-mean_a2/2/d2).^2*ba^2 ...
    + (0.5*d1*(mean_a2+mean_a1))).^2*bm^2).^0.5;

%Combined uncertainty
t = 3.264; % 8 measurements, 95% confidence interval
UFy = t*(rand_Fy.^2./sqrt(numfiles)+bFy.^2).^0.5;
UMx = t*(rand_Mx./sqrt(numfiles)+bMx.^2).^0.5;


%% make plots
%% make plots
speed = [0 1000 2000 3000 4000 5000 6000 7000 8000 9000 10000 11000 12000 13000 14000 1500

figure
subplot(2,1,1)
title('Disturbance force and moment from acceleration measurements')
errorbar(speed,mean_Fy,mean_Fy.*UFy)
ax = gca;
ax.XAxis.Exponent = 0;
grid on; grid minor;
xlabel('Rotation speed [RPM]')
ylabel('Fy [N]')

subplot(2,1,2)
errorbar(speed, mean_Mx, mean_Mx.*UMx)
xlabel('Rotation speed [RPM]')
ylabel('Mx [Nm]')
grid on; grid minor
```

Reproducability of results

Ideally two simultaneous measurements of accelerations are used to compute the forces and moments. This was not possible because only one sensor was available. Separate measurements are combined to compute the forces and moments. Figure D.7 shows that even though the measurements are taken at different times they are aligned in phase. Figure D.8 shows test results for eight different measurements, indicating that at lower rotation speeds reproducibility is good, while at larger speeds there are some problems. As discussed in Section 11.6 this is likely due to the fact that the wheel was not perfectly tightly mounted on the seismic mass. However, this was not verified experimentally due to time constraints. Furthermore, measurements at locations three and four were not possible either. They can be used to validate the moment calculated from measurements at locations 1 and 2, and so would give a good idea of the reproducibility. For now, the random uncertainty of the measurements, which has a maximum value of six %, indicates that the measurements are reproducible. However, the suggestions for an improved design in Section 10.8 should be implemented as well.

Uncertainty analysis

The independent variable in this experiment is the motor speed. In reality the supply voltage is switched with a given duty cycle thus supplying the motor with the required voltage to rotate with the desired speed, but for all practical purposes the motor speed is the independent variable. The dependent variables are the vibrations created by the wheel, transmitted to the seismic mass and measured by the accelerometer. The controlled variables are the supply voltage, mass of the seismic block, distances between accelerometer locations and centre of mass and moment of inertia of the block. Four measurements of acceleration are used to calculate the forces and moments with the equations presented in Section 10.6. The random uncertainty of the measurements can be computed directly from the result using Equation (D.12). The systematic uncertainties of each parameter must be propagated by deriving equations for the forces and moments using Equation (D.2). The mass of the block was measured on a scale with an error of 0.5 [g]. All distances are measured with a caliper with an accuracy of 0.1 [mm], however the measurement uncertainty is constrained by the handling of the tool to 1

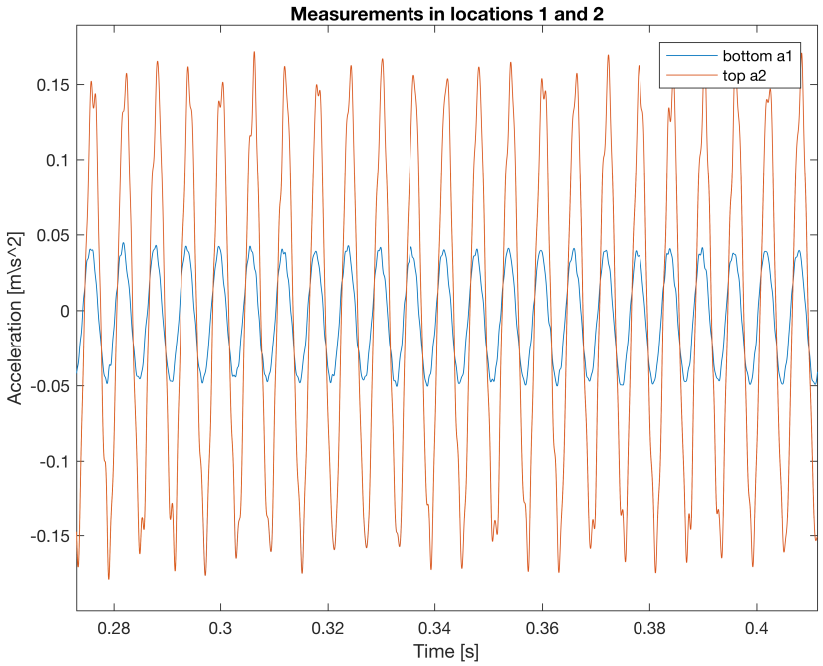

Figure D.7: Time series acceleration data from location 1 and 2

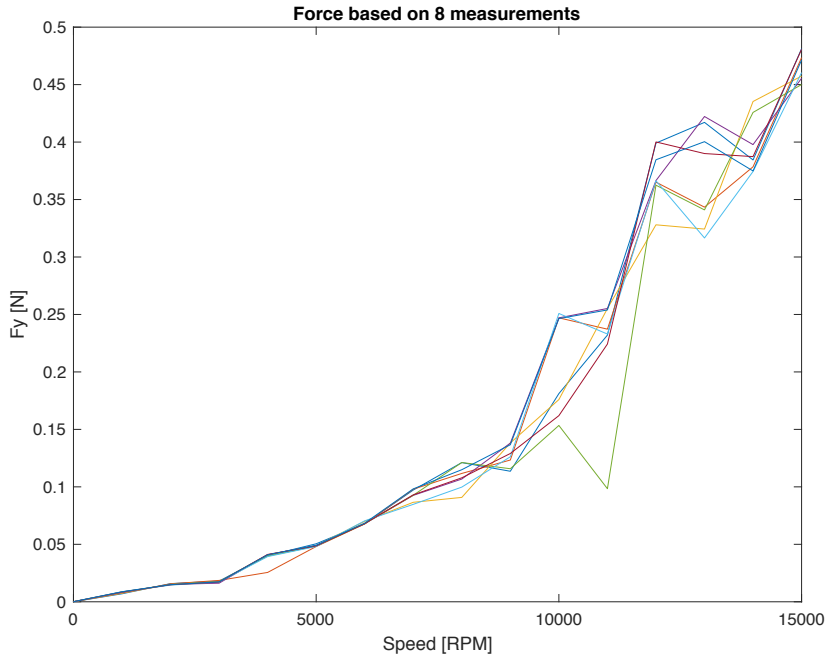

Figure D.8: Force in y-direction computed from 8 different measurements

[mm]. The accelerometer has an accuracy of three % in the range between 0-1 [kHz]. The moment of inertia is determined using Catia with material properties of aluminium. However, not all holes are exactly replicated in Catia. Therefore the uncertainty is estimated at 2 %. The derived equations for the uncertainty in the measurements of F_y and M_x are presented in Equation (D.15) and Equation (D.16). Note that the uncertainties in the distances cancel out in the first equation and that d_1 is equal to d_2.

$$b_{F_y} = \left| \left(\frac{1}{2} a_1 + \frac{1}{2} a_2 \right)^2 \times b_m^2 + \frac{1}{2} m^2 \times b_a^2 \right|^{\frac{1}{2}} \tag{D.15}$$

$$b_{Mx} = \left| \left(\frac{a_1 - a_2}{2d} \right)^2 \times b_{I_{xx}}^2 + \left(\frac{1}{2} \left(\frac{I_{xx}(a_2 - a_1)}{d^2} \right) + m(a_1 + a_2) \right)^2 \times b_d^2 + \left(\frac{I_{xx} + md^2}{2d} \right)^2 \times b_a^2 \cdots \right.$$
$$\left. + \left(\frac{md}{2} - \frac{a_2}{2d} \right)^2 \times b_a^2 + \left(\frac{1}{2} d(a_1 + a_2) \right)^2 \times b_m^2 \right|^{\frac{1}{2}} \tag{D.16}$$

Bibliography

[1] Mai-200 ADCS Data Sheet. Technical report, Inc, Maryland Aerospace, 2011.

[2] Astrofein GmbH Datasheet RW1, 2016. URL http://www.astrofein.com/astro-und-feinwerktechnik-adlershof/produkte/raumfahrt/9/rw-1/.

[3] Blue canyon technologies Datasheet RWP015, 2016. URL http://bluecanyontech.com/microwheel/.

[4] CubeSpace Datasheet CubeWheel small, 2016. URL https://www.cubespace.co.za/cubewheel.

[5] Gomspace Datasheet GSW-600, 2016. URL https://gomspace.com/shop/subsystems/adcs/nanotorque-gsw-600.aspx.

[6] Hyperion Technologies Datasheet RW210, 2016. URL http://hyperiontechnologies.nl/products/rw210/.

[7] D. Addari, G. S. Aglietti, and M. Remedia. Experimental and numerical investigation of coupled microvibration dynamics for satellite reaction wheels. *Journal of Sound and Vibration*, 386:225–241, 2017. ISSN 10958568. doi: 10.1016/j.jsv.2016.10.003.

[8] M. Boerci. Small satellite launcher loads TU Delft Internal Document, 2017.

[9] Bruce Bowman, W. Tobiska, and Frank Marcos. A New Empirical Thermospheric Density Model JB2006 Using New Solar Indices. *AIAA/AAS Astrodynamics Specialist Conference and Exhibit*, (August), 2006. doi: 10.2514/6.2006-6166. URL http://arc.aiaa.org/doi/abs/10.2514/6.2006-6166.

[10] Gian Paolo Candini, D Ph, Fabrizio Piergentili, and Fabio Santoni. Designing , Manufacturing , and Testing a Self-Contained and Autonomous Nanospacecraft Attitude Control System. 27(6):1–8, 2014. ISSN 0893-1321. doi: 10.1061/(ASCE)AS.1943-5525.0000291.

[11] M. C. Chou, C. M. Liaw, S. B. Chien, F. H. Shieh, J. R. Tsai, and H. C. Chang. Robust current and torque controls for PMSM driven satellite reaction wheel. *IEEE Transactions on Aerospace and Electronic Systems*, 47(1):58–74, 2011. ISSN 00189251. doi: 10.1109/TAES.2011.5705659.

[12] John Christian, Michael Turbe, Erik Kabo, Laura Manno, and Eric Johnson. Development of a Variable Inertia Reaction Wheel System for Spacecraft Attitude Control. In *AIAA Guidance, Navigation, and Control Conference and Exhibit*, number August, pages 1–13, Reston, Virigina, 8 2004. American Institute of Aeronautics and Astronautics. ISBN 978-1-62410-073-4. doi: 10.2514/6.2004-5132. URL http://arc.aiaa.org/doi/10.2514/6.2004-5132.

[13] Hugh W. Coleman and W. Glenn Steele. *Experimentation, Validation, and Uncertainty Analysis for engineers*. John Wiley & Sons, Inc., Hoboken, New Jersey, 3rd edition, 2009. ISBN 978-0-470-16888-2.

[14] Xiaofeng Ding, Guanliang Liu, Min Du, Hong Guo, Hao Qiao, and Christopher Gerada. Development of an Axial Flux MEMS BLDC Micromotor with Increased Efficiency and Power Density. *Energies*, 8(7):6608–6626, 2015. ISSN 1996-1073. doi: 10.3390/en8076608. URL http://www.mdpi.com/1996-1073/8/7/6608/.

[15] L M Elias, D W Miller, and Alexander Bell Drive. AIAA-2002-1252 A Coupled Disturbance Analysis Method Using Dynamic Mass Measurement Techniques AIAA / ASME / ASCE / AHS / ASC Structures , Structural MASS MEASUREMENT TECHNIQUES. (April), 2002.

[16] ESA/ESTEC. ECSS-E-ST-10-04C Space engineering Space environment. (January), 2008.

[17] Michele M Gates. INSPECTING THE CHARACTERISATION OF MICROVIBRATION SOURCES Daniele. pages 1–10, 2014.

[18] Jens Gießelmann. Development of an Active Magnetic Attitude Determination and Control System for Picosatellites on Highly Inclined Circular Low Earth Orbits. (June):1–191, 2006.

[19] Jian Guo, Jasper Bouwmeester, and Eberhard Gill. In-orbit results of Delfi-n3Xt: Lessons learned and move forward. *Acta Astronautica*, 121:39–50, 2016. ISSN 00945765. doi: 10.1016/j.actaastro.2015.12.003. URL http://dx.doi.org/10.1016/j.actaastro.2015.12.003.

[20] J R Hendershot and Magna Physics Publishing. Design of Brushless Permanent- Magnet Motors. (5), 2010.

[21] Russel C. Hibbeler. *Mechanics of Materials*. Prentice Hall, 7th edition, 2007. ISBN 978-0132209915.

[22] Antonius G.L. Hoevenaars. *Master of Science Thesis: Design , Integration and Verification of the Delfi-n3Xt Reaction Wheel System*. PhD thesis, Delft University of Technology, 2012.

[23] Jan Holterman and Pim Groen. *An Introduction to Piezoelectric Materials and Applications*. Stichting Applied Piezo, 2013. ISBN 978-90-819361-1-8.

[24] Yi Huang and Chunquan Li. Model and system simulation of Brushless DC motor based on SVPWM control. *Proceedings of the 2nd International Conference on Electronic and Mechanical Engineering and Information Technology (2012)*, pages 1765–1768, 2012. doi: 10.2991/emeit.2012.391. URL http://www.atlantis-press.com/php/paper-details.php?id=3609.

[25] Co Huynh, Liping Zheng, and Dipjyoti Acharya. Losses in High Speed Permanent. *Journal of Engineering for Gas Turbines and Power*, 131(March):1–6, 2009. ISSN 07424795. doi: 10.1115/1.2982151. URL http://www.calnetix.com/sites/default/files/7_0.pdf.

[26] Dahaman Ishak, Z. Q. Zhu, and David Howe. Eddy-Current Loss in the Rotor Magnets of Permanent-Magnet Brushless Machines Having a Fractional Number of Slots Per Pole. *2462 Ieee Transactions on Magnetics*, 41(9):2462–2469, 2005.

[27] Vahid Izadi, Mostafa Abedi, and Hossein Bolandi. Verification of Reaction Wheel Functional Model in Test-bed. *4th International Conference on Control, Instrumentation, and Automation (ICCIA)*, (January): 155–160, 2016.

[28] Sanjay Jayaram. Design and analysis of nano momentum wheel for picosatellite attitude control system. *Aircraft Engineering and Aerospace Technology*, 81(5):424–431, 2009. ISSN 0002-2667. doi: 10.1108/00022660910983707.

[29] Dae Kwan Kim. Micro-vibration model and parameter estimation method of a reaction wheel assembly. *Journal of Sound and Vibration*, 333(18):4214–4231, 2014. ISSN 10958568. doi: 10.1016/j.jsv.2014.04.032.

[30] W. J. Larson and J. R. Wertz. *Space Mission Analysis and Design*. 1999. ISBN 978-1881883104.

[31] Nissen Lazreg. Design and Architecture of Pico-Satellites Network for Earth Coverage. pages 601–605, 2016. ISBN 9781467385268.

[32] Kuo-Chia Liu, Peiman Maghami, and Carl Blaurock. Reaction Wheel Disturbance Modeling, Jitter Analysis, and Validation Tests for Solar Dynamics Observatory. *AIAA Guidance, Navigation, and Control Conference and Exhibit*, (August):1–18, 2008. doi: doi:10.2514/6.2008-7232.

[33] Carmen Lungoci and D A N Stoia. Temperature effects on torque production and efficiency of motors with NdFeB. *Parameters*, 3(1):445–454, 2008.

[34] Robert Lyle, Pericles Stabekis, Lee Sentman, and R. Passamaneck. NASA: Spacecraft aerodynamic torques. Technical Report January, 1971.

[35] Ki B. Ma, Yong Zhang, Yevgeniy Postrekhin, and Wei Kan Chu. HTS bearings for space applications: Reaction wheel with low power consumption for mini-satellites. *IEEE Transactions on Applied Superconductivity*, 13(2 II):2275–2278, 2003. ISSN 10518223. doi: 10.1109/TASC.2003.813064.

[36] James P. Mason, Thomas N. Woods, Amir Caspi, Phillip C. Chamberlin, Christopher Moore, Andrew Jones, Rick Kohnert, Xinlin Li, Scott Palo, and Stanley C. Solomon. Miniature X-Ray Solar Spectrometer: A Science-Oriented, University 3U CubeSat. *Journal of Spacecraft and Rockets*, 53(2):328–339, 3 2016. ISSN 0022-4650. doi: 10.2514/1.A33351. URL http://arc.aiaa.org/doi/10.2514/1.A33351.

[37] Maxon Motors. Maxon DC motor and Maxon EC motor Key information. Technical Report May, 2011.

[38] Peter Millett. Application Report: SLVA504 Calculating Motor Driver Power Dissipation. Technical Report February, Texas Instruments, 2012. URL http://www.ti.com/lit/an/slva504/slva504.pdf.

[39] Sreeja Nag, Joseph L. Rios, David Gerhardt, and Camvu Pham. CubeSat constellation design for air traffic monitoring. *Acta Astronautica*, 128:180–193, 2016. ISSN 00945765. doi: 10.1016/j.actaastro.2016.07.010.

[40] Hwa-suk Oh and Dong-ik Cheon. Precision Measurements of Reaction Wheel Disturbances with Frequency Compensation Process. *Journal of Mechanical Science and Technology*, 19(1):136–143, 2005. ISSN 1738-494X. doi: 10.1007/BF02916112.

[41] John F. O'Hanlon. *A User's Guide to Vacuum Technology*. John Wiley & Sons, Inc., Hoboken, New Jersey, 3rd edition, 2003. ISBN 978-0-471-27052-2.

[42] Scott E. Palo. High rate communications systems for CubeSats. In *2015 IEEE MTT-S International Microwave Symposium*, pages 1–4. IEEE, 5 2015. ISBN 978-1-4799-8275-2. doi: 10.1109/MWSYM.2015.7167152. URL http://ieeexplore.ieee.org/document/7167152/.

[43] Christopher M. Pong, Matthew W. Smith, Matthew W. Knutson, Sungyung Lim, David W. Miller, Sara Seager, Jesus S. Villaseñor, and Shawn D. Murphy. One-arcsecond line-of-sight pointing control on exoplanetsat, a three-unit CubeSat. *Advances in the Astronautical Sciences*, 141:147–166, 2011. ISSN 00653438.

[44] Schmitz. MS5607 pressure sensor code, 2017. URL https://github.com/Schm1tz1/arduino-ms5xxx.

[45] Sara C Spangelo, D. Kaslow, Chris Delp, Bjorn Cole, L. Anderson, E. Fosse, B. S. Gilbert, L. Hartman, T. Kahn, and J. Cutler. Applying Model Based Systems Engineering (MBSE) to a standard CubeSat. In *2012 IEEE Aerospace Conference*, pages 1–20. IEEE, 3 2012. ISBN 978-1-4577-0557-1. doi: 10.1109/AERO.2012.6187339. URL http://ieeexplore.ieee.org/lpdocs/epic03/wrapper.htm?arnumber=6187339.

[46] Xun Sun and Xiaofeng Wu. Novel ultrasonic motor driver design for CubeSat reaction wheel. *2013 IEEE International Conference on Mechatronics and Automation, IEEE ICMA 2013*, (1):425–430, 2013. doi: 10.1109/ICMA.2013.6617956.

[47] Michael Swartwout and Clay Jayne. University-Class Spacecraft by the Numbers: Success, Failure, Debris. (But Mostly Success.). *AIAA/USU Conference on Small Satellites*, 2016. URL http://digitalcommons.usu.edu/smallsat/2016/TS13Education/1.

[48] Shigemune Taniwaki and Yoshiaki Ohkami. Experimental and Numerical Analysis of Reaction Wheel Disturbances, 2003. ISSN 1344-7653. URL http://www.scopus.com/inward/record.url?eid=2-s2.0-0041323082&partnerID=tZOtx3y1.

[49] Tanya Vladimirova, Xiaofeng Wu, Kawsu Sidibeh, David Barnhart, and Abdul Halim Jallad. Enabling technologies for distributed picosatellite missions in LEO. *Proceedings - First NASA/ESA Conference on Adaptive Hardware and Systems, AHS 2006*, 2006:330–337, 2006. doi: 10.1109/AHS.2006.33.

[50] Kirk Woellert, Pascale Ehrenfreund, Antonio J. Ricco, and Henry Hertzfeld. Cubesats: Cost-effective science and technology platforms for emerging and developing nations. *Advances in Space Research*, 47 (4):663–684, 2011. ISSN 02731177. doi: 10.1016/j.asr.2010.10.009.

[51] Zhe Zhang, Guglielmo S. Aglietti, and Weiyong Zhou. Microvibrations Induced by a Cantilevered Wheel Assembly with a Soft-Suspension System. *AIAA Journal*, 49(5):1067–1079, 2011. ISSN 0001-1452. doi: 10.2514/1.J050791. URL http://www.scopus.com/inward/record.url?eid=2-s2.0-79955542147&partnerID=tZOtx3y1.

[52] Zhe Zhang, Guglielmo S. Aglietti, and Wei Jia Ren. Microvibration Model Development and Validation of a Cantilevered Reaction Wheel Assembly. *Applied Mechanics and Materials*, 226-228:133–137, 11 2012. ISSN 1662-7482. doi: 10.4028/www.scientific.net/AMM.226-228.133. URL http://www.scientific.net/AMM.226-228.133.

[53] Wei Yong Zhou, Guglielmo S. Aglietti, and Zhe Zhang. Modelling and testing of a soft suspension design for a reaction/momentum wheel assembly. *Journal of Sound and Vibration*, 330(18-19):4596–4610, 2011. ISSN 0022460X. doi: 10.1016/j.jsv.2011.03.028. URL http://dx.doi.org/10.1016/j.jsv.2011.03.028.

[54] Christof Zwyssig, Thomas Baumgartner, and Johann W. Kolar. High-Speed Magnetically Levitated Reaction Wheel Demonstrator. In *The 2014 International Power Electronics Conference*, 2014.